OUKA
The University of Osaka
Institutional Knowledge Archive

Title	Spin-orbit Splitting of ^<13>_ΛC Hypernucleus studies by the ^<13>C(K^-,π^-) reaction
Author(s)	Kohri, Hideki
Citation	大阪大学, 2000, 博士論文
Version Type	VoR
URL	https://doi.org/10.11501/3169107
rights	
Note	

The University of Osaka Institutional Knowledge Archive : OUKA

https://ir.library.osaka-u.ac.jp/

The University of Osaka

理学 7181

Spin-orbit Splitting of ${}^{13}_{\Lambda}\mathrm{C}$ Hypernucleus studied by the ${}^{13}\mathrm{C}(K^-, \pi^-)$ reaction

Hideki Kohri

Department of Physics

Osaka University

January, 2000

理甲 7181

Spin-orbit Splitting of ${}^{13}_{\Lambda}\mathrm{C}$ Hypernucleus studied by the ${}^{13}\mathrm{C}(K^-, \pi^-)$ reaction

Hideki Kohri

Department of Physics

Osaka University

January, 2000

Abstract

The γ-rays from the $1/2^-$ and $3/2^-$ doublet states at $\sim$11 MeV to the ground state in $^{13}_{\Lambda}$C were successfully measured by using 72 NaI detectors to obtain the spin-orbit splitting energy with high precision. The energy resolution of the NaI detector for the detection of the 11 MeV γ-ray is about 350 keV. It is almost an order-of-magnitude better than those of the magnetic spectrometers ($\sim$2 MeV) previously used to determine the splitting. $^{13}_{\Lambda}$C is an unique hypernucleus to measure the spin-orbit splitting clearly. $^{13}_{\Lambda}$C has single Λ particle states with $p_{1/2}(\Lambda)(j_\Lambda=l_\Lambda-1/2)$ and $p_{3/2}(\Lambda)(j_\Lambda=l_\Lambda+1/2)$ which couple to the spin 0^+ ^{12}C core. The energy difference of the states thus simply corresponds to the spin-orbit splitting. Since these states lie under the particle emission threshold, the energy difference can be observed by their γ-decays. The (K^-, π^-) reaction on an enriched ^{13}C target was used to excite these states. High intensity K^- beam of $\sim 5 \times 10^4$/spill at the beam momentum of 0.93 GeV/c was provided by the D6 line at the AGS of BNL. Scattered π^-s at 0 to 16 degrees were detected by the 48D48 spectrometer, which enabled us to excite the $1/2^-$ and $3/2^-$ doublet states simultaneously. The angular distribution of the ^{13}C$(K^-, \pi^-)^{13}_{\Lambda}$C reaction makes separate population of the doublet states possible by which we extracted the spin-orbit splitting with little systematic errors. The obtained spin-orbit splitting of $^{13}_{\Lambda}$C is 152 $\pm$ 54 (stat.) $\pm$ 35 (syst.) keV. It is almost 30$\sim$40 times smaller than that of single particle states in nuclei. Furthermore the $j_\Lambda=l_\Lambda-1/2$ ($p_{1/2}(\Lambda)$) state still appears higher in energy as in nuclei. The result is compared with recent theoretical predictions and other experimental results.

Contents

1 Introduction 5
- 1.1 Spin-orbit Interaction . . . 5
- 1.2 Historical Development of Study of Spin-orbit Splitting . . . 6
  - 1.2.1 Small Spin-orbit Splitting . . . 6
  - 1.2.2 Relatively Large Spin-orbit Splitting . . . 9
- 1.3 Theoretical Predictions . . . 11
  - 1.3.1 Boson Exchange Model . . . 11
  - 1.3.2 Quark Model . . . 11

2 Experiment 13
- 2.1 Principles of Experiment . . . 13
- 2.2 AGS accelerator . . . 16
- 2.3 Kaon Beam Line . . . 16
  - 2.3.1 Scintillator Hodoscopes in Beam Line . . . 18
  - 2.3.2 Beam Line TOF . . . 18
  - 2.3.3 Profile of K^- Beam . . . 19
- 2.4 Triggers . . . 20
- 2.5 Spectrometer (48D48) . . . 21
  - 2.5.1 Acceptance of 48D48 Spectrometer . . . 24
  - 2.5.2 Scintillator Hodoscopes in Spectrometer . . . 25
  - 2.5.3 Čerenkov Counters . . . 27
  - 2.5.4 Drift Chambers . . . 37
  - 2.5.5 TOF Wall (BT) . . . 39
- 2.6 Other Detectors around Target . . . 40
  - 2.6.1 Active Target (LT) . . . 40
  - 2.6.2 Decay Particle Counters (DEC) . . . 41
  - 2.6.3 Charged Particle Veto Counters (VETO) . . . 41
  - 2.6.4 NaI Detectors . . . 42
- 2.7 Energy Calibration of NaI Detector . . . 44
  - 2.7.1 ^{22}Na source . . . 44
  - 2.7.2 ^{58}Ni(n, γ) reaction . . . 45
  - 2.7.3 Linearlity of Energy Calibration . . . 48
  - 2.7.4 Energy Resolution of NaI detector . . . 49
- 2.8 Energy Correction of Doppler Shift . . . 51
- 2.9 How to Add γ-ray Energies . . . 52
- 2.10 Data Acquisition and Monitoring System . . . 55
- 2.11 Off-line Data Analysis System . . . 56

3 Data Analysis 57
- 3.1 Data Reduction . . . 57
- 3.2 Event Selection . . . 58

3.2.1 Beam line TOF 58
3.2.2 Mass of Outgoing Particles 59
3.2.3 Reaction Vertices 60
3.2.4 DEC 62
3.2.5 LT 64
3.2.6 VETO 69
3.2.7 NaI Detectors 72
3.2.8 Energy Spectrum of $^{13}_{\Lambda}$C 73
3.2.9 Analysis Efficiency and Detection Efficiency for the 11 MeV γ-ray . 75

4 Experimental Result and Discussion **76**
4.1 Quasi-free Region of ^{13}C(K^-, π^-) Reaction 76
4.1.1 γ-ray Energy Spectrum Around 4.4 MeV 76
4.1.2 γ-ray Energy Spectrum Around 15 MeV 77
4.2 Bound Region of ^{13}C(K^-, π^-) Reaction 78
4.2.1 γ-ray Energy Spectrum Around 4.9 MeV 78
4.2.2 γ-ray Energy Spectrum Around 11 MeV 81
4.3 Spin-orbit Splitting Energy 85
4.4 Evaluation of Systematic Errors 86
4.4.1 Systematic Error Originating from Cross Sections 86
4.4.2 Systematic Error Originating from Fits to Histograms 87
4.4.3 Systematic Error Originating from Doppler Shift Correction 88
4.5 Discussion 91

5 Summary **93**

1 Introduction

1.1 Spin-orbit Interaction

Historically, an introduction of the spin-orbit interaction resulted in the greatest successes of the nuclear shell model. Before the introduction, the central potential described by the harmonic oscillator with

$$\hbar\omega_0 \approx 40A^{-\frac{1}{3}}\mathrm{MeV} \tag{1}$$

was unable to explain magic numbers except for 2, 8 and 20 [1]. The spin-orbit potential

$$V = V_{so}(\boldsymbol{r})\boldsymbol{l}\cdot\boldsymbol{s}, \tag{2}$$

where $\boldsymbol{l}$ and $\boldsymbol{s}$ indicate an orbital angular momentum and a spin of a nucleon respectively, clearly explained all of the magic numbers. The spin-orbit interaction explains well not only the magic numbers but also many prominent nuclear properties, therefore it plays a very important role in the nuclear physics.

The spin-orbit interaction splits a single-particle state with the orbital angular momentum l into two states of j=l+1/2 and j=l−1/2, where j indicates a total angular momentum. In the former case $\boldsymbol{l}$ and $\boldsymbol{s}$ are parallel, and the spin-orbit force is attractive. While in the latter case $\boldsymbol{l}$ and $\boldsymbol{s}$ are antiparallel, and the spin-orbit force is repulsive. Since the $\boldsymbol{l}\cdot\boldsymbol{s}$ is calculated to be

$$\begin{aligned} \boldsymbol{l}\cdot\boldsymbol{s} &= \frac{1}{2}(\boldsymbol{j}^2 - \boldsymbol{l}^2 - \boldsymbol{s}^2) && (3)\\ &= \frac{1}{2}\left(j(j+1) - l(l+1) - \frac{3}{4}\right), && (4) \end{aligned}$$

the spin-orbit potential is expressed as

$$V = \begin{cases} -\frac{1}{2}V_{so}(\boldsymbol{r})(l+1), & j = l - \frac{1}{2} \\ \frac{1}{2}V_{so}(\boldsymbol{r})l, & j = l + \frac{1}{2}. \end{cases} \tag{5}$$

Thus the splitting energy ΔE_{so}=$E_{j=l+1/2} - E_{j=l-1/2}$ is given as

$$\Delta E_{so} = -\langle V_{so}(\boldsymbol{r})\rangle(l + \frac{1}{2}). \tag{6}$$

Systematic studies of ΔE_{so} for various nuclei found that ΔE_{so} is given as

$$\Delta E_{so} \propto A^{-\frac{2}{3}}(l + \frac{1}{2}), \tag{7}$$

where A indicates the mass number of the nucleus.

On the other hand, as for interactions related to Λ particle, the (π^+, K^+) reaction data have clarified the gross structure of the Λ-nucleus interaction [2, 3, 4]. The phenomenological analyses with the use of Woods-saxon potentials indicated that the dominant central part of the Λ-nucleus interaction was about 2/3 (~ 28 MeV) of that of the nucleon [4, 5]. While, the spin dependent parts were found to be surprisingly small. For example, the spin-orbit interaction was about an order-of-magnitude smaller than that of the nucleon [6]. It can be naively explained that the spins of the u, d quarks couple to zero and the s quark contributes little to the nuclear force. The small Λ-nucleus spin-orbit interaction has been one of the most interesting subjects in the hypernuclear physics for more than 20 years.

1.2 Historical Development of Study of Spin-orbit Splitting

1.2.1 Small Spin-orbit Splitting

In 1978, the first indication of the small Λ-nucleus spin-orbit interaction was given by the ^{16}O(K^-, π^-)$^{16}_{\Lambda}$O experiment performed at the beam momentum of 0.715 GeV/c at the CERN Proton Synchrotron (PS) [6]. In the experiment using SPES II with the momentum resolution of 2 MeV/c, four peaks were observed at 0° as shown in Fig.1.

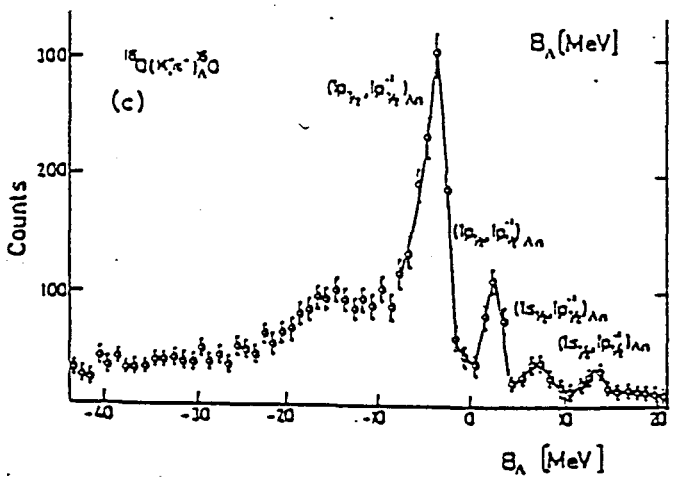

Figure 1: Spectrum obtained by the ^{16}O(K^-, π^-)$^{16}_{\Lambda}$O reaction at the momentum 0.715 GeV/c plotted as a function of the transformation energy $M_{HY} - M_A$.

The first peak with the configuration of $[(p_{1/2})_n^{-1}(s_{1/2})_\Lambda]$ and the second peak with the configuration of $[(p_{3/2})_n^{-1}(s_{1/2})_\Lambda]$ were observed with the energy difference of about 6 MeV. In addition, the third peak with the configuration of $[(p_{3/2})_n^{-1}(p_{3/2})_\Lambda]_{0^+}$ and the

forth peak with the configuration of $[(p_{1/2})_n^{-1}(p_{1/2})_\Lambda]_{0+}$ were also observed with the energy difference of about 6 MeV. The assigned configurations of the peaks are based on the fact that the (K^-, π^-) reaction dominantly excites substitutional states at 0° because of its small momentum transfer. The splitting energy of the neutron $p_{1/2}$ and $p_{3/2}$ hole states in ^{15}O, which is a core nucleus of $^{16}_{\Lambda}$O, is 6.176 MeV. The observed splitting energies are almost the same as the well known splitting in ^{15}O. It seems that the Λ-^{15}O spin-orbit interaction is extremely small. As the result for the p-shell hyper nuclei, W. Bruckner *et al.* gave an upper limit of 0.3 MeV for the spin-orbit splitting.

In 1981, the result of the ^{13}C$(K^-, \pi^-)^{13}_{\Lambda}$C experiment performed by M. May *et al.* at the beam momentum of 0.8 GeV/c at BNL-AGS was published [7]. Moby-Dick spectrometer with the energy resolution of 2.5 MeV was used.

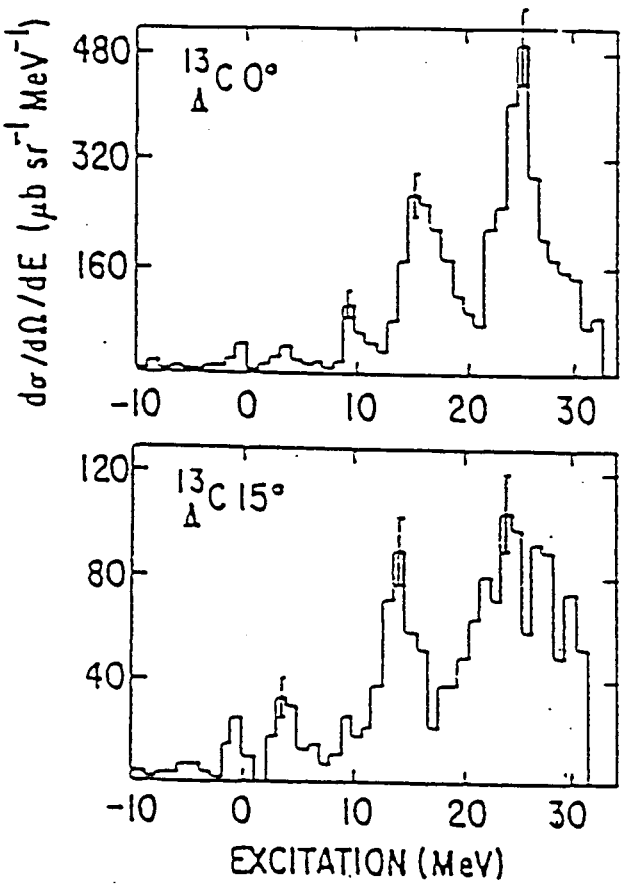

Figure 2: Energy spectra of $^{13}_{\Lambda}$C obtained by the (K^-, π^-) reaction at 0° and 15°.

In Fig.2, a peak observed at about 10 MeV at 0° is considered to have the configuration of $[(p_{1/2})_n^{-1}(p_{1/2})_\Lambda]_{1/2-}$. Because the (K^-, π^-) reaction at 0° dominantly excites states

with the ΔL=0 transition. While a peak like structure observed at about 10 MeV at 15° is considered to have the configuration of $[(p_{1/2})_n^{-1}(p_{3/2})_\Lambda]_{3/2^-}$. Because the transitions with larger momentum transfer such as the ΔL=2 transition are dominant at 15°. The energy difference between the peaks gives the spin-orbit splitting of ${}^{13}_{\Lambda}$C. A measured splitting energy of the doublet states was 0.36$\pm$0.3 MeV.

In 1983, the result of the ^{9}Be(K^-, π^- γ)${}^9_\Lambda$Be experiment performed by M. May *et al.* at the beam momentum of 0.82 GeV/c at BNL-AGS was published [8]. The energy resolution of the excitation energy was 7 MeV by using Moby-Dick spectrometer. They detected γ-rays from ${}^9_\Lambda$Be by using six NaI detectors of 12.7 cm in diameter and 7.6 cm thick installed at 11.4 cm from the target center and two NaI detectors of 20.3 cm in diameter and 15.2 cm thick installed at 20.0 cm from the target. There were two peaks in the γ-ray energy spectrum in Fig.3.

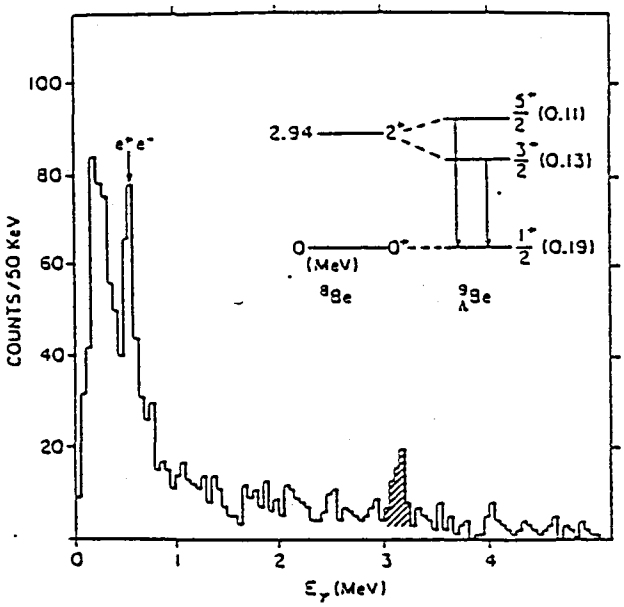

Figure 3: γ-ray energy spectrum observed in coincidence with the Λ bound region of the ${}^9_\Lambda$Be excitation energy spectrum.

One peak at 0.511 MeV corresponds to the annihilation, and the other peak at 3.079 $\pm$ 0.040 MeV corresponds to a γ-ray either from the $3/2^+$ state or from the $5/2^+$ state to the ground state ($1/2^+$) in ${}^9_\Lambda$Be. The $3/2^+$ and $5/2^+$ doublet states are formed with a Λ in the s-orbit added to the 2^+ state in ^{8}Be. The 2^+ state is formed by the orbital angular momentum of two α particles (L=2). The energy difference between the doublet states gives the spin-orbit splitting. The $3/2^+$ and $5/2^+$ states are predicted to be excited with almost equal intensity by the ^{9}Be(K^-, π^-)${}^9_\Lambda$Be reaction. The first excited state of ^{8}Be

lies at 2.94 MeV and decays into two α particles. The additional binding provided by the presence of Λ is considered to make the hypernuclear doublet stable. The peak at 3.079 $\pm$ 0.040 MeV had width of 150 $\pm$ 30 keV compared with their estimated resolution of 160 keV. If two γ-rays were observed as a peak, the doublet splitting would be less than 100 keV with 95 % confidence. Conversely, if either state of the doublet states lies above the particle emission threshold, the splitting would be large.

1.2.2 Relatively Large Spin-orbit Splitting

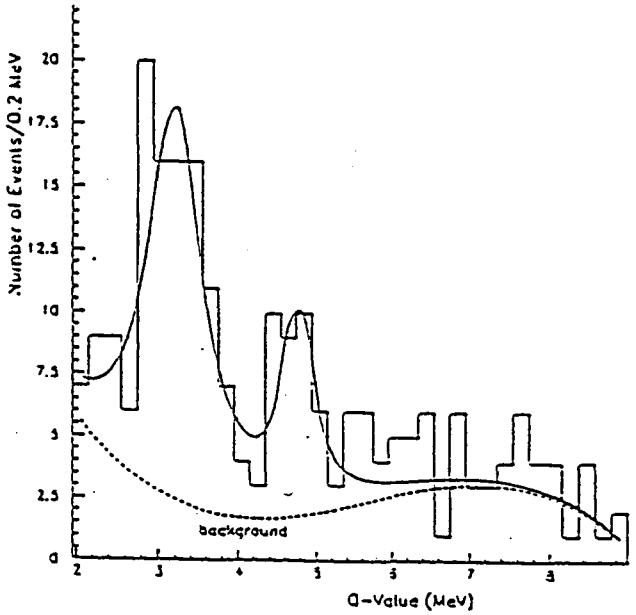

Figure 4: Q-value distribution for ${}^{16}_{\Lambda}O^{*}$ events. The solid curve represents the best fit, the dashed curve represents the background contribution.

On the other hand, a relatively large spin-orbit splitting was also indicated by the re-analysis of the emulsion data in 1997 [9]. The original experiments were performed by the European K^- collaboration in 1970's. In the emulsion experiment, K^- interactions at rest, whose final particles have the topology "charged pion, stable particle (range > 2 μm) and recoiling hypernucleus" are selected and interpreted as examples of the process

$$K^- + {}^{A}\mathrm{Z} \rightarrow \pi^- + \mathrm{p} + {}^{(A-1)}_{\Lambda}(\mathrm{Z}-1). \tag{8}$$

The observation of a visible track for the hypernucleus implies that the initial nucleus ^{A}Z is necessarily a light nucleus. There are compositions of ^{12}C (52 %), ^{14}N (12 %) and ^{16}O (36 %) in the emulsion. R. H. Dalitz *et al.* selected events of

$$K^- + {}^{16}\mathrm{O} \rightarrow \pi^- + \mathrm{p} + {}^{15}_{\Lambda}\mathrm{N}, \tag{9}$$

and observed two peaks in the Q-value distribution for ${}^{16}_{\Lambda}$O as shown in Fig.4. The larger peak observed at 3.20 $\pm$ 0.08 MeV in the Q-value distribution was considered to dominantly be the 2^+ state with the configuration of $[(p_{1/2})_n^{-1}(p_{3/2})_\Lambda]$, while the smaller peak observed at 4.76 $\pm$ 0.09 MeV in the Q-value distribution was considered to be the 0^+ state with the configuration of $[(p_{1/2})_n^{-1}(p_{1/2})_\Lambda]$. As the result, an observed spin-orbit splitting was 1.56 $\pm$ 0.12 MeV for the 2^+ and 0^+ doublet states in ${}^{16}_{\Lambda}$O.

In 1995, the result of the ^{89}Y$(\pi^+, K^+)^{89}_{\Lambda}$Y experiment performed at KEK was published by T. Nagae *et al.* [10]. In the experiment SKS spectrometer with the energy resolution of ~2 MeV was used. There were more than four bumps in the energy spectrum of ${}^{89}_{\Lambda}$Y as shown in Fig.5.

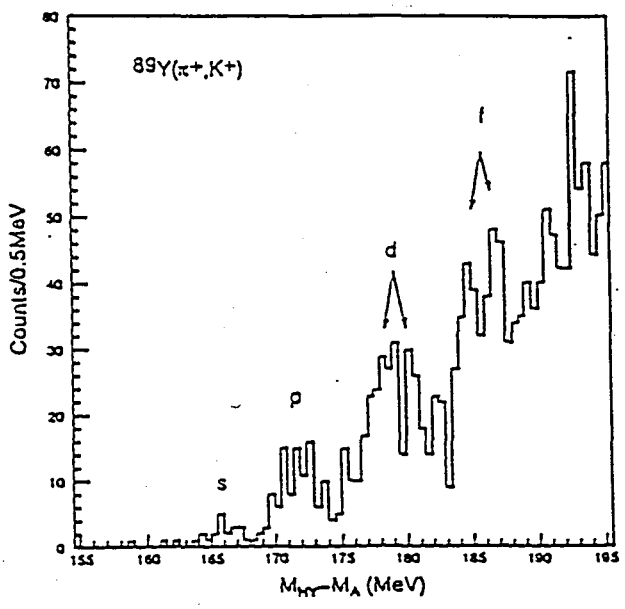

Figure 5: Energy spectrum of the ^{89}Y$(\pi^+, K^+)^{89}_{\Lambda}$Y reaction.

The lowest, the second, the third and the forth bumps are considered to be states with a Λ in the s-orbit, in the p-orbit, in the d-orbit and in the f-orbit, respectively. The lower two bumps do not have micro structure, however the higher two look separated into two peaks. In addition, a splitting energy of the f-states observed larger than that of the d-states, which is consistent with the theoretical expectation. In 1998, they performed a new experiment using the same reaction in order to confirm the splitting [11].

The Λ-nucleus spin-orbit splitting energies extracted before are far from conclusive because of insufficient quality of the experiments. One of the most important factors in measuring the splitting is energy resolution. Typical energy resolution of the magnetic

spectrometer is about 2 MeV FWHM which is not enough to distinguish states. A new experiment with high resolution, high statistics and high quality is needed to measure the spin-orbit splitting energy with high precision.

1.3 Theoretical Predictions

1.3.1 Boson Exchange Model

Traditionally, interactions between baryons have been investigated by the meson exchange theory combined with phenomenology [12, 13, 14, 15]. It has been tried to construct potential models which can describe simultaneously nucleon-nucleon (NN) and hyperon-nucleon (YN) systems. A purpose of the combined study is to obtain the unified picture by using the kinematical breaking of $SU_F(3)$ symmetry. Another purpose is to give a good theoretical description of the YN interaction by using the results for the meson-nucleon coupling constants from the NN analysis. The Nijmegen group has constructed one boson exchange (OBE) models for a realistic description of the NN and YN channels since 1972 [16, 17]. After 1990 they started to construct models which include two-meson exchange. The OBE models are divided into hard-core and soft-core models. The well known model D and model F are in the first category [18, 19]. They have been applied to YN and also hyperon-hyperon (YY) [20, 21]. The soft-core models have been applied in [22, 23, 24]. They give a quantitative account of the rich and accurate NN data and also give a good description of YN.

In the OBE model, heavy vector mesons contribute much to the spin-orbit interaction which is the short-range part. K. Itonaga *et al.* predicted a spin-orbit splitting using the YNG ΛN effective interaction deduced on the basis of the G-matrix calculation with Nijmegen model D [25]. A predicted spin-orbit splitting was 0.56 MeV for the $1/2^-$ and $3/2^-$ doublet states in ${}^{13}_{\Lambda}\mathrm{C}$.

1.3.2 Quark Model

Several attempts have been made to study the short-range part of the NN interaction from the standpoint that the baryons are made of quarks and the short-range part of baryon-baryon interactions should be understood as a nature of the quark many-body systems [26, 27, 28, 29, 30]. They succeeded in reproducing the repulsive-core-like phase shift. O. Morimatsu *et al.* studied the spin-orbit interaction between baryons in a non-relativistic quark-cluster model [31]. The Galilei-invariant part of the spin-orbit term in the one-gluon-exchange potential was considered since this term seemed best founded among the various origins of the spin-orbit interaction. It gives, for examples, the NN spin-orbit interaction which is qualitatively similar to the empirical ones. It is well known, however, that this term disturbs the description of excited baryons. Other origins of the spin-orbit interaction which effectively cancel the contribution of this term are phenomenologically required. Among them are the frame-dependent antisymmetric spin-orbit term (ALS) in the one-gluon-exchange potential and the spin-orbit term from the confinement

term, although none of them seem established. Under these circumstances, they decided to concentrate on the effect of the best-founded term and left the other contributions. An interesting feature of the spin-orbit interaction between a hyperon and a nucleon is the presence of the ALS term. The relative orbital angular momentum and the difference of the spins are related to the ALS term. This model gave comparatively strong ALS terms both for the ΛN and ΣN interactions but with opposite signs. Therefore, the Λ-nucleus spin-orbit splitting becomes small and the Σ-nucleus spin-orbit splitting becomes large.

H. J. Pirner *et al.* also predicted zero splitting for the Λ-nucleus spin-orbit interaction in terms of the combined quark-gluon exchange between the valence baryon and the nucleons in the nucleus [32]. Since they considered only those contributions which were additive in the spins and isospins of the exchanged light quarks, they called it the additive quark model.

Theoretically, there are obvious discrepancies between predictions on the Λ-nucleus spin-orbit splitting with the OBE models and the quark models.

In 1998 we performed the ^{13}C(K^-, π^- γ)$^{13}_{\Lambda}$C experiment at BNL. Our experiment has great advantages over previous experiments to measure the spin-orbit splitting energy with high precision. First, better energy resolution of the NaI detector than magnetic spectrometers' gives high precision. Second, higher statistics obtained using 72 NaI detectors covering large solid angles also gives high precision. Third, $^{13}_{\Lambda}$C is an unique hypernuclei. Last, we have a special device to suppress the in-flight decay of K^- which is the most dominant background in the experiment. These advantages are described in detail below.

2 Experiment

2.1 Principles of Experiment

We measured the γ-rays from the $1/2^-$ and $3/2^-$ states to the ground state in ${}^{13}_{\Lambda}$C by using 72 NaI detectors to obtain the spin-orbit splitting of ${}^{13}_{\Lambda}$C with high precision. The $1/2^-$ and $3/2^-$ states are extremely rare states. It is well known that the $1/2^-$ state has the configuration of $[{}^{12}\mathrm{C}(\mathrm{g.s.}\ 0^+) \otimes (p_{1/2})_\Lambda]$, while the $3/2^-$ state has the configuration of $[{}^{12}\mathrm{C}(\mathrm{g.s.}\ 0^+) \otimes (p_{3/2})_\Lambda]$ as shown in Fig.6. These states are the partners of the spin-orbit doublet states. By virtue of the 0^+ spin of the ^{12}C core, interactions related to the core spin can be ignored, thus the spin-orbit splitting is clearly observed. The doublet states had been experimentally observed at around 11 MeV [7, 33]. Theoretically, the doublet states were predicted by E. Hiyama *et al.* as the bound states at a little bit under the Λ emission threshold (11.70 MeV) as shown in Fig.7 [34]. They performed the calculation with OBE ΛN interaction (NSC97f). The doublet states decay to the ground state in ${}^{13}_{\Lambda}$C by emitting γ-rays via the E1 transitions (100 %). In the ${}^{13}\mathrm{C}(K^-, \pi^-){}^{13}_{\Lambda}\mathrm{C}$ reaction, at around 0° the transition from the $1/2^-$ state to the ground state is isotropic, while at around 15° the correlation of the transition from the $3/2^-$ state to the ground state has the form $1-0.6\cos^2\theta$ [35].

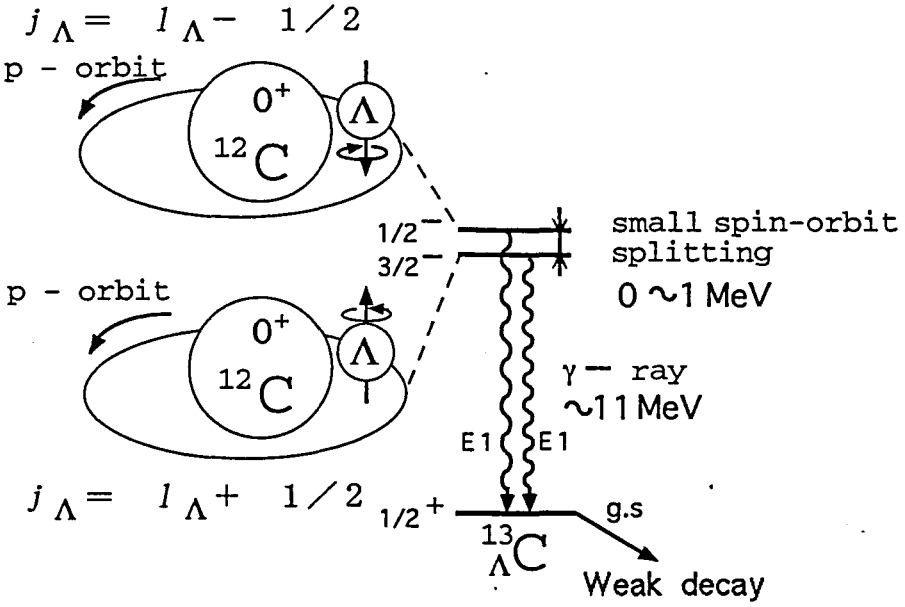

Figure 6: Configurations of the $1/2^-$ and $3/2^-$ doublet states in ${}^{13}_{\Lambda}$C.

An advantage of measuring γ-rays is a better energy resolution. Historically, it has been tried to observe the $1/2^-$ and $3/2^-$ doublet states by the (K^-, π^-) and (π^+, K^+) reactions. But the excitation energies have not been clearly obtained yet due to insufficient energy resolution of the magnetic spectrometers ($\sim$2 MeV) [7, 36, 37]. We used 72 NaI detectors which had the energy resolution of 350 keV FWHM for the detection of the 11 MeV γ-ray. The energy resolution is almost an order-of-magnitudes better than those obtained by using magnetic spectrometers. The better energy resolution gives higher precision.

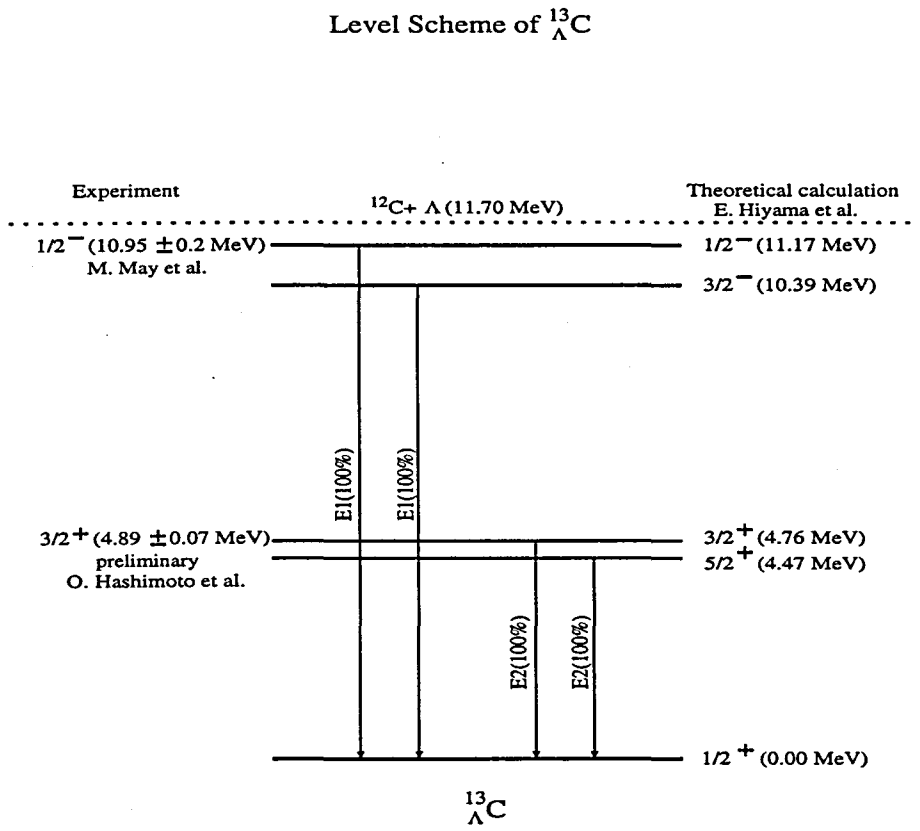

Figure 7: Level scheme of $^{13}_{\Lambda}$C.

We needed to separately excite the $1/2^-$ and $3/2^-$ doublet states, therefore the (K^-, π^-) reaction was used to form the $^{13}_{\Lambda}$C hypernucleus. The reaction has advantageous angular distributions for the doublet states at the momentum of 0.9 GeV/c. Fig.8 shows the cross sections of the doublet states calculated by T. Motoba *et al.* [38]. The $1/2^-$ state is excited dominantly at the forward angles via the ΔL=0 transition. While the $3/2^-$ state is excited dominantly at the larger angles of $\sim$13° via the ΔL=2 transition. The cross angle of the cross sections is about 9°. The (π^+, K^+) reaction does not satisfy our experimental demands. It is weak in exciting the $1/2^-$ state because of its larger

momentum transfer than that of the (K^-, π^-) reaction. We also needed high K^- beam intensity to obtain sufficient statistics for the conclusive result. We expected the intense K^- beam of 10^5 K^-s for 10^{13} protons only at BNL-AGS-D6 line [39]. In addition, we also expected the clean beam with the $(\pi^-\mu^-e^-)/(K^-)$ ratio of less than 0.01 there. The beam intensity and the $(\pi^-\mu^-e^-)/(K^-)$ ratio at D6 line are particularly excellent. At D6 line, the quantity of (cross section) $\times$ (beam intensity), that is in proportion to the yield, becomes the maximal at the beam momentum of 0.9 GeV/c.

The (K^-, π^-) reaction on an enriched ^{13}C target was used to excite the doublet states in $^{13}_{\Lambda}$C at BNL-AGS-D6 line. We set the K^- beam momentum at 0.93 GeV/c which was close to 0.9 GeV/c at the center of the target after the momentum loss. Scattered π^-s at 0 to 16 degrees were detected by the spectrometer, which enabled us to excite the doublet states simultaneously. For suppressing the background due to the in-flight decay of K^-, we made an active target of ^{13}C, which enabled us to selectively observe the ^{13}C$(K^-, \pi^-)^{13}_{\Lambda}$C reaction at all the scattering angles. The special device for the suppression of the background was one of important advantages of our experiment.

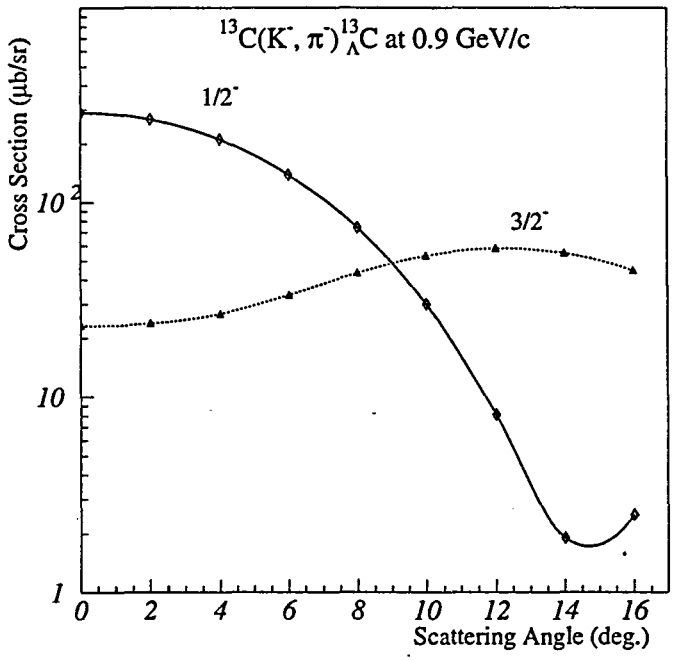

Figure 8: Predicted cross sections of the $1/2^-$ and $3/2^-$ doublet states with the ^{13}C$(K^-, \pi^-)^{13}_{\Lambda}$C reaction at 0.9 GeV/c.

2.2 AGS accelerator

Alternating Gradient Synchrotron (AGS) has been one of the world's foremost particle accelerators since 1962, with three Nobel Prizes and many discoveries in high-energy and nuclear physics. AGS is used to accelerate proton and heavy irons up to energies of more than 20 GeV per unit charge. The proton and the heavy irons are accelerated during different running periods throughout the year. This experiment (E929) was done during the proton running period of AGS.

During the 1998 proton running cycle, typically 4.5×10^{13} protons from AGS were extracted per spill of 4.5 seconds and distributed among several beam lines. About 5×10^{12} protons per spill were allocated to D6 line. At D6 line these protons are used to bombard a platinum target for the production of K^-.

In the near future, AGS will be used to inject beam into RHIC that is a new accelerator under construction now. RHIC will soon be one of the largest and most powerful accelerators in the world. It is capable of creating thousands of head-on collisions between beams of heavy irons or polarized protons. Four massive experiments being built along the RHIC's 3.8 km underground ring will capture the particles unleashed when the beams collide. It is possible to search for a form of matter that has not existed since moments after the Big Bang.

2.3 Kaon Beam Line

The experiment was performed by using the 2-GeV/c kaon beam line (BNL-AGS-D6 line) which had been operational since 1991. The beam line can deliver intense and clean beams of kaon. Details of the beam line are described in Ref. [40]. For better separation of kaons from other particles such as pions, the beam line has two stages of velocity selection and magnetic optics corrected to third order. Fig.9 shows a schematic layout of the beam line. The beam line elements involve three dipoles (D1-3), nine quadrupoles (Q1-9), six sextupoles (S1-6), five octupoles (O1-5), two velocity sectors with separated E and B fields (E1,2 and CM1-4) and collimators (4-Jaw, HS and MS1,2). Primary protons which are accelerated to 24 GeV/c by AGS are incident on a 9 cm thick platinum

Maximum Momentum	1.9 GeV/c
Length	31.6 m
Angular acceptance	1.6 msr
Momentum acceptance	6% FWHM
Beam optics	corrected to third order
Target thickness	9 cm
Electrostatic separators	750 kV, 10.2 cm gap × 4.5 m length
Production angle	5 degrees

Table 1: Parameters of the AGS 2 Gev/c beam line

production target located at the entrance to the first dipole (D1). Secondary particles are transported with the extraction angles of 5 degrees and the momentum acceptance of 6 % (FWHM). After the velocity is selected with two stages of separators (CM1-E1-CM2 and CM3-E2-CM4), they are delivered to the final focus point (FF).

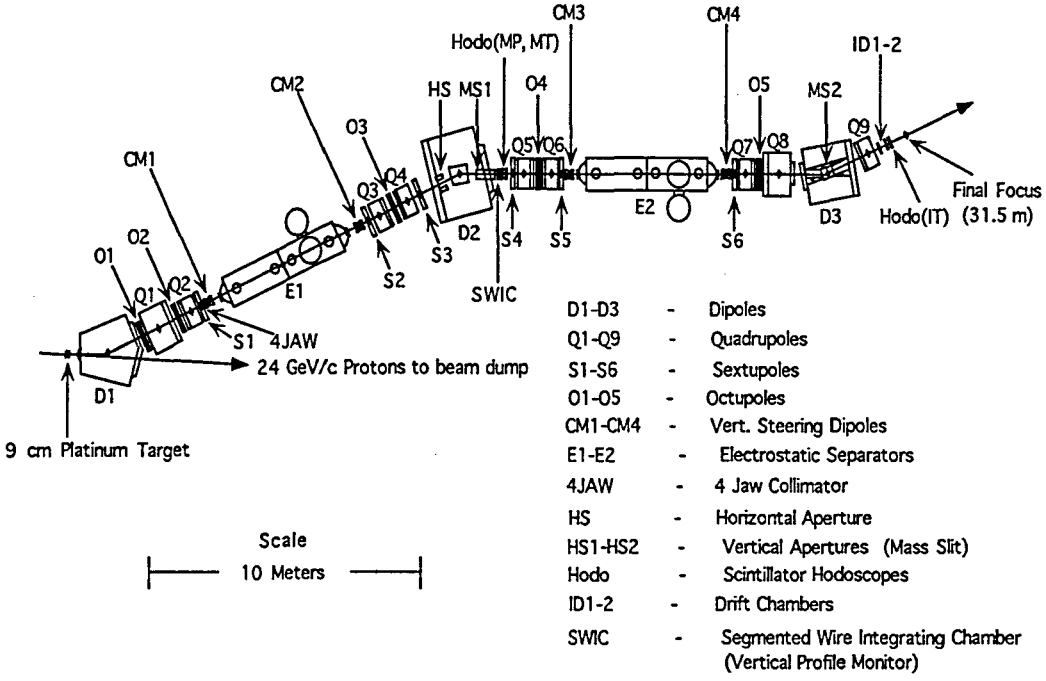

Figure 9: Schematic layout of the BNL-AGS 2 GeV/c K^- beam line.

Design parameters of the beam line are summarized in Table.1. A typical intensity of the 0.93 GeV/c beam was $\sim 5 \times 10^4$ K^-s/spill for 5×10^{12} protons at D-primary target, which is consistent with the expected intensity of 10^5 K^-s/spill for 10^{13} protons [39]. Although a typical $(\pi^- \ \mu^- \ e^-)/K^-$ ratio of the beam line is $\sim$0.01 at 0.93 GeV/c, we used the setting of $\sim$0.3 for increasing the beam intensity. The ratio of $\sim$0.3 was good enough for performing our experiment.

2.3.1 Scintillator Hodoscopes in Beam Line

Table.2 shows the specifications of two scintillator hodoscopes of MP and MT installed between the first mass slit (MS1) and the forth sextupole (S4). The primary function of MP which has 72 elements is to determine the beam momentum by measuring the x position of the particle, whereas that of MT is to measure the time of flight (TOF) between MT and IT installed in the spectrometer.

Hodoscope	Orientation	Dimension (a)	Segmentation
MP	V	1.5 × 0.7 × 0.3	72
MT	V	1.5 × 3.7 × 0.6	9

[a] dimension of one element (length × width × thickness (cm^3))

Table 2: Specifications of the scintillator hodoscopes in the beam line. The orientation is indicated by the direction of hodoscopes (V: vertical).

2.3.2 Beam Line TOF

Fig.10 shows difference of the beam line TOF in the logarithmic scale, where the TOF between MT♯5 and IT is selected to limit spreading of the beam momentum. Data were collected with the IT trigger to be defined below. The TOF of the K^- beam is adjusted to zero. A distance between MT and IT is about 15.4 m which is long enough to separate the K^- beam from the π^- beam at the beam momentum of 0.93 GeV/c. A timing resolution is about 75 ps for the K^- beam, while it is about 250 ps for the π^- beam.

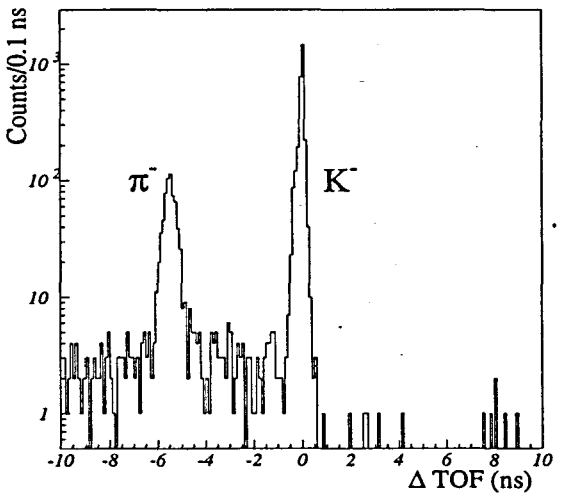

Figure 10: Difference of the beam line TOF. Data were collected with the IT trigger.

2.3.3 Profile of K^- Beam

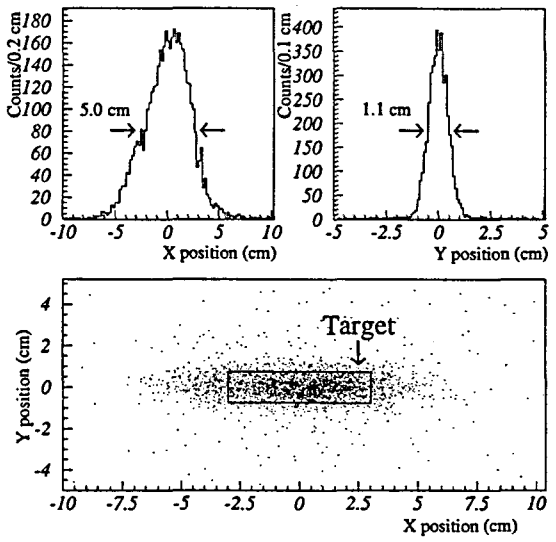

Figure 11: Profile of the K^- beam. The target region is indicated by a square.

The beam profile at the target which is reconstructed with drift chambers of ID1 and ID2 is shown in Fig.11. Data were collected with the IT trigger, and the K^- beam is selected using TOF shown in Fig.10. Size of the K^- beam (FWHM) is 5.0 cm in the horizontal direction and 1.1 cm in the vertical direction. The vertical size is much smaller than the horizontal one because the last quadrupole Q9 is designed to focus the beam vertically. The target region is indicated by a square.

Fig.12 shows the angle distribution of the K^- beam. The angle is also determined with ID1 and ID2. The horizontal distribution (FWHM) is 1.2 degrees, and the vertical distribution is 0.6 degrees.

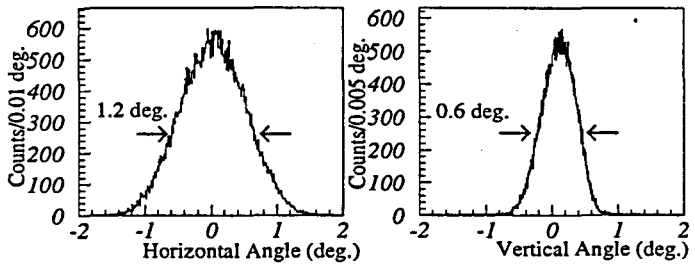

Figure 12: Horizontal and vertical angle distributions of the K^- beam.

2.4 Triggers

The hardware trigger was formed from the discriminated signals of the plastic and liquid scintillators (IT, BS, LT1, FP and BP) and the discriminated signals of the Čerenkov counters (IC, BQC and FAC).

The "Kbeam" and "πbeam" triggers were used to identify beam particles entering the target region. These triggers are defined as

$$Kbeam = IT \cdot \overline{IC_1^4} \cdot BS \cdot \overline{BQC} \cdot LT1, \quad (10)$$

$$\pi beam = IT \cdot IC_1^4 \cdot BS \cdot BQC \cdot LT1. \quad (11)$$

IC_1^4 indicates that all PMTs (♯1-♯4) of IC were used.

The "Kscat" and "πscat" used to identify outgoing particles into 48D48 spectrometer are defined as

$$Kscat = \overline{FAC} \cdot FP_1^{11} \cdot BP_1^6, \quad (12)$$

$$\pi scat = FAC \cdot FP_1^{11} \cdot BP_1^6. \quad (13)$$

FP_1^{11} indicates that 11 elements (♯1-♯11) of FP were used. BP_1^6 indicates that all elements (♯1-♯6) of BP were used.

Although only Kbeam and πscat were of interest for collecting the (K^-,π^-) reaction data, we also acquired the data with the Kbeam, πbeam and IT triggers for investigating performance of the detectors. We also acquired the data with the ^{22}Na and LED triggers for the energy calibration of NaI detectors. The typical trigger rate and the prescale factor are summarized in Table.3.

Trigger	Definition	Rate/spill	Prescale factor
IT	IT	9×10^4	4×10^4
Kbeam	Kbeam	5×10^4	8×10^4
πbeam	πbeam	2×10^4	1×10^4
$K\pi$	Kbeam ∩ πscat	160	1
^{22}Na	^{22}Na ∩ prescaled NaIor	5×10^3	2×10^2
LED	LED ∩ prescaled NaIor	20	2

Table 3: Definition of the on-line triggers. The typical rate per spill and prescale factor used for the data taking are also shown.

2.5 Spectrometer (48D48)

Schematic side view of the spectrometer is shown in Fig.13, and schematic view of target region is also shown in Fig.14. The detectors of a scintillator hodoscope (BS), a quartz Čerenkov counter (BQC), an active target (LT) are covered with an iron box as shown in Fig.15. The iron box with thickness of 5 mm is used as the shield against the magnetic field to maintain enough pulse heights near the magnet. The iron box has windows for beams, outgoing particles and decay particles not to be disturbed. Scintillator hodoscopes of IT, BS, FP and BP are used to form the trigger. A delivered K^- beam is identified by two Čerenkov counters of an aerogel (IC) and BQC. While an outgoing π^- is identified by an aerogel Čerenkov counter (FAC). Two drift chambers of ID1 and ID2 are used for the beam tracking. The outgoing π^- is bent vertically by the 48D48 magnet, and its momentum is measured by the tracking using five drift chambers of FD1-3 and BD1-2. BT is used to measure the TOF between IT and itself.

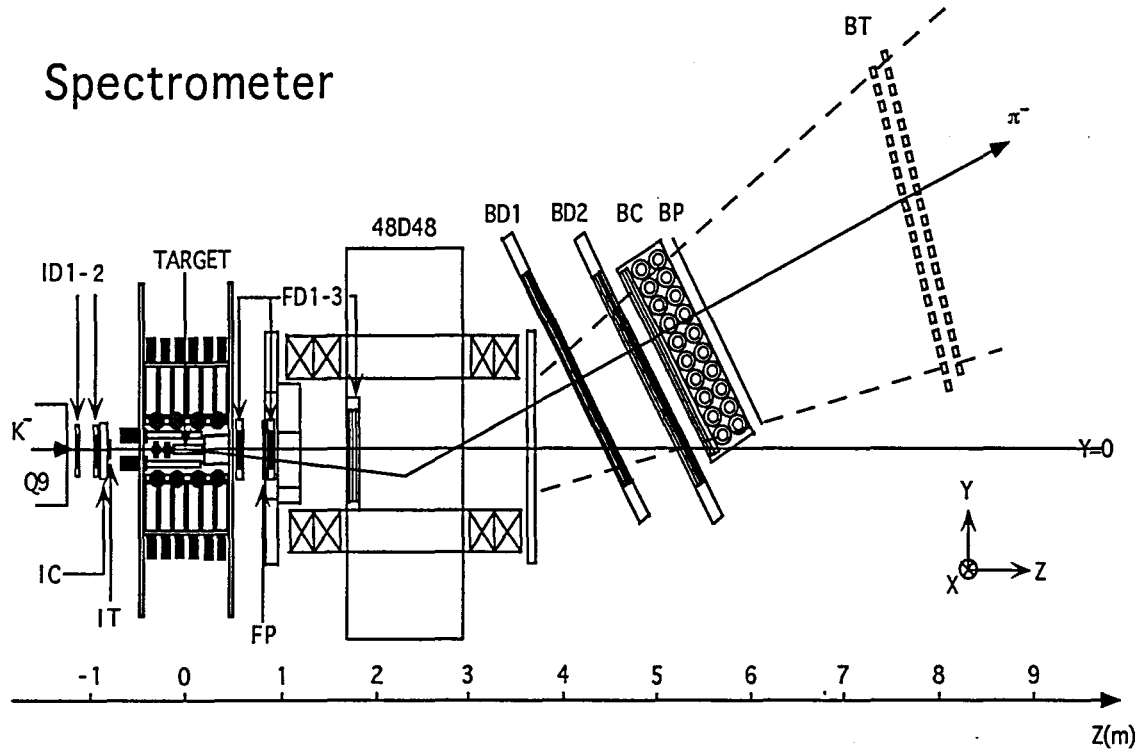

Figure 13: Experimental Setup of BNL-AGS-D6LINE.

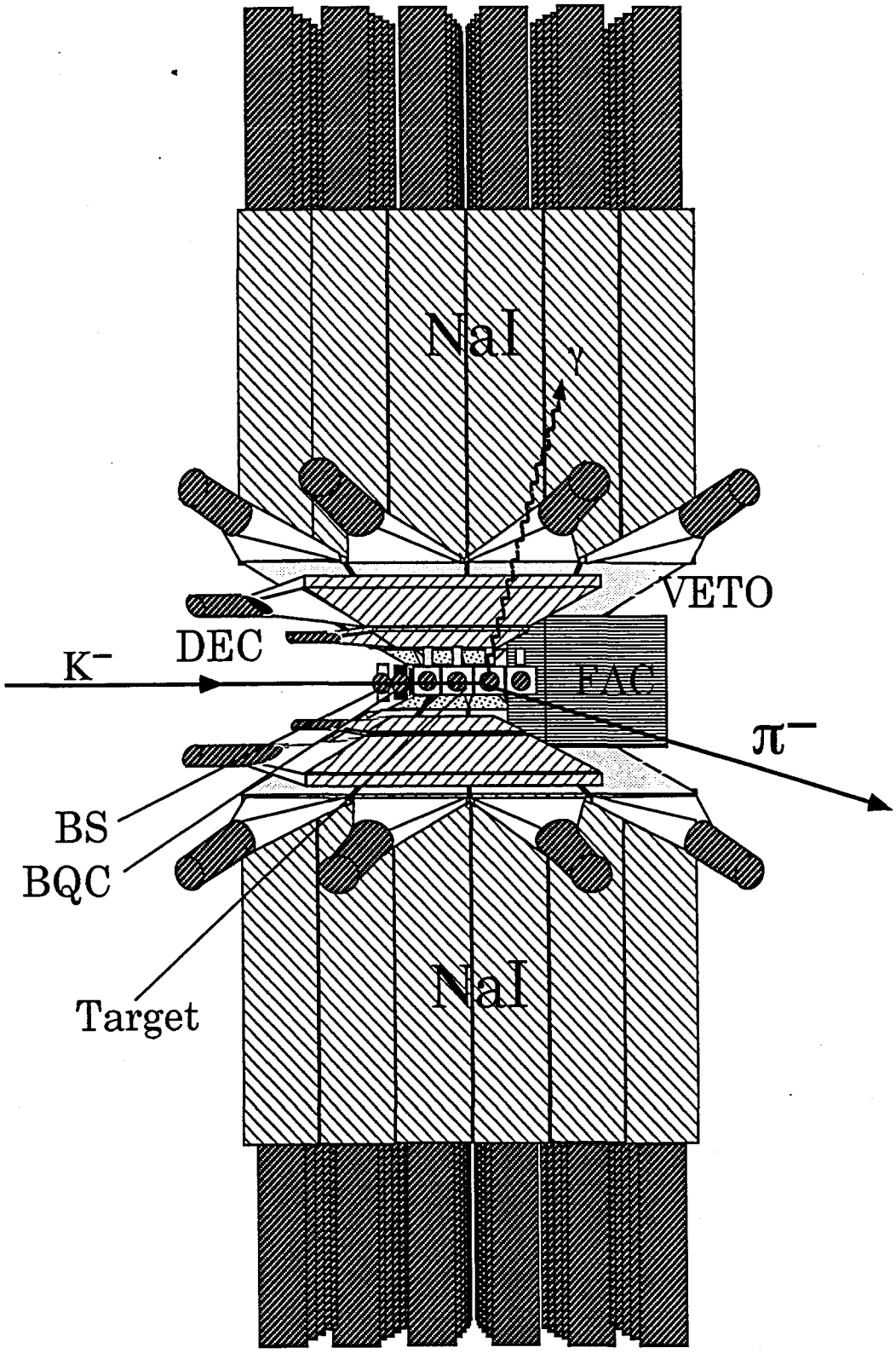

Figure 14: Schematic view around the target.

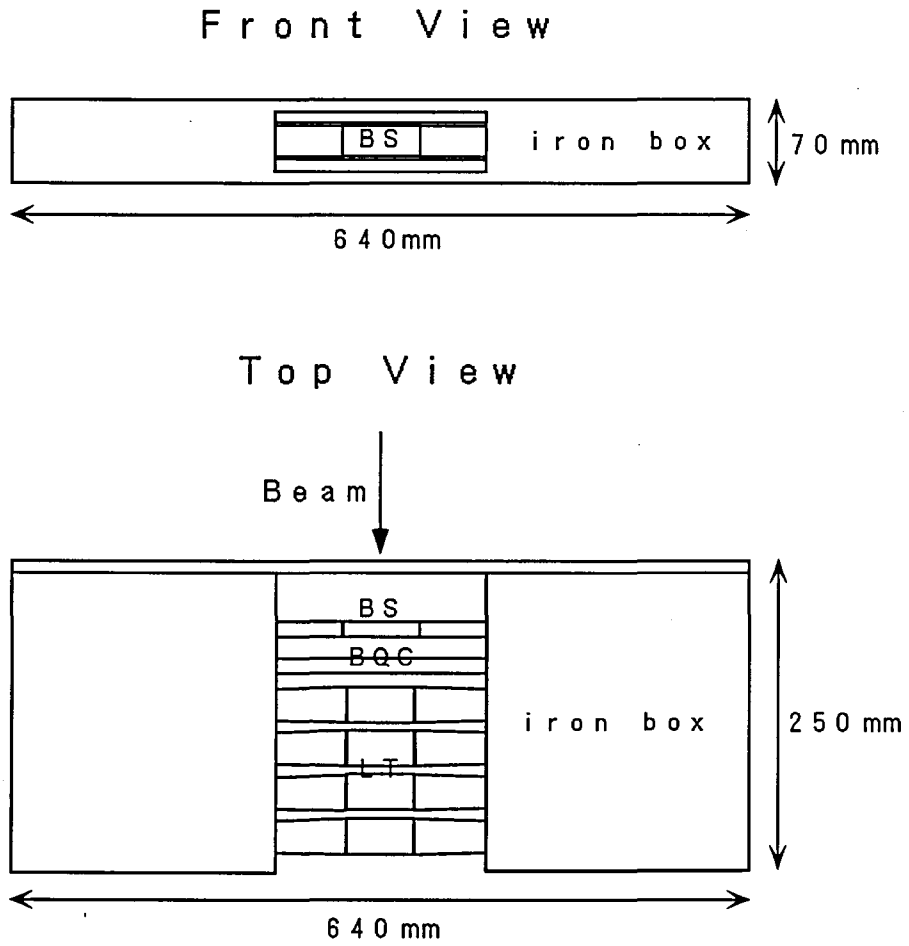

Figure 15: Drawing of an iron box covering the PMTs of the detectors installed around the target. The iron box was used as a shield against the magnetic field of the spectrometer. Thickness of the iron box is 5 mm.

2.5.1 Acceptance of 48D48 Spectrometer

In the D6 line, the 48D48 dipole magnet (48" pole length by 48" width) with a gap of 80 cm was used as a magnetic spectrometer. The central magnetic field was set 0.71 Tesla in the experiment. The direction of the magnetic field was horizontal, therefore outgoing particles were bent vertically. Large acceptance of 48D48 spectrometer collected with the KPI trigger is shown in Fig.16, where most of in-flight decays of K^- are rejected by event selections. Horizontal acceptance of -8 to 8 degrees is limited by the covered angles with BP installed downstream the spectrometer. Vertical acceptance of -16 to 0 degrees is limited by the covered angles with FP installed between drift chambers of FD1 and FD2.

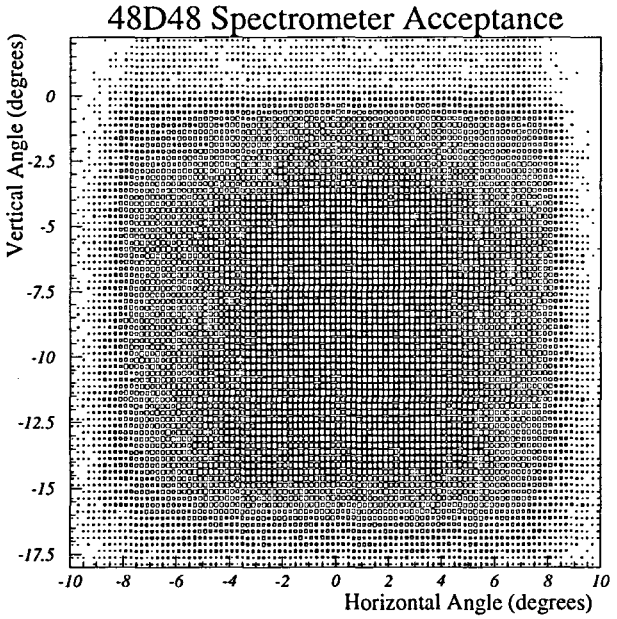

Figure 16: Acceptance of 48D48 spectrometer.

Expected cross sections of the $1/2^-$ and $3/2^-$ doublet states in ${}^{13}_{\Lambda}\mathrm{C}$ by considering the acceptance of 48D48 spectrometer using the Monte Carlo simulation, GEANT is shown in Fig.17(a). Original cross sections are calculated by T. Motoba *et al.* [38]. Fig.17(b) shows the purities of the integrated cross sections of the doublet states. For example, when obtained data are divided into two parts by 9°, the purity of the $1/2^-$ state integrated from 0° to 9° and that of the $3/2^-$ state integrated from 9° to 16° are the same ($\sim$0.78).

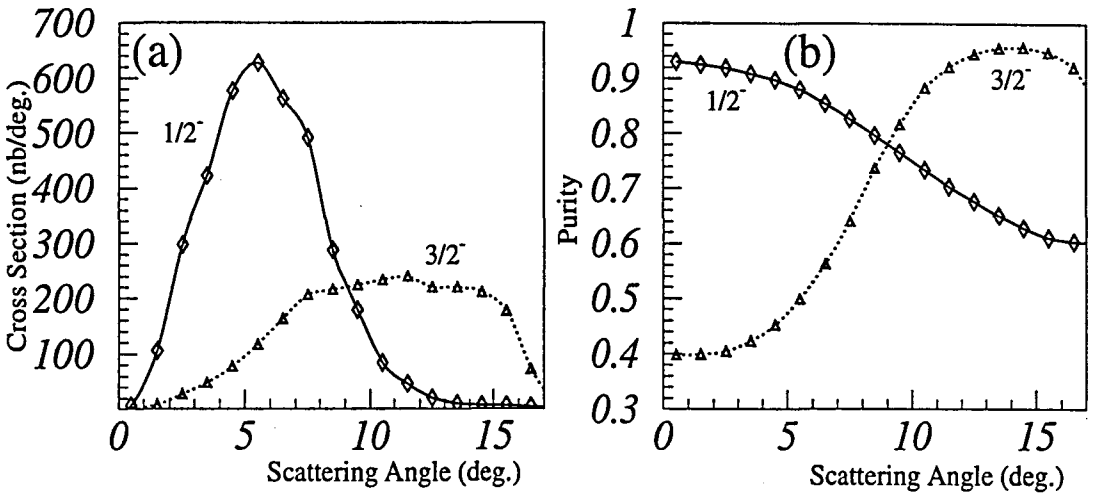

Figure 17: (a) Expected cross sections by considering the acceptance of 48D48 spectrometer. The solid curve represents the $1/2^-$ state's, while the dotted curve represents the $3/2^-$ state's. (b) Purities of the integrated cross sections. The purity of the $1/2^-$ state (solid curve) represents the ratio of $\sigma_{1/2^-}/(\sigma_{1/2^-}+\sigma_{3/2^-})$ integrated from 0° to a certain angle corresponding to the horizontal axis. While the purity of the $3/2^-$ state (dotted curve) represents the ratio of $\sigma_{3/2^-}/(\sigma_{1/2^-}+\sigma_{3/2^-})$ integrated from a certain angle, corresponding to the horizontal axis, to 16°.

2.5.2 Scintillator Hodoscopes in Spectrometer

Table.4 shows the specifications of four scintillator hodoscopes of IT, BS, FP and BP.

IT

IT operated at high counting rate under beam-on condition is equipped with 2" PMTs (Hamamatsu H6533) with booster power supplies to hold potentials of the last three dynodes. IT provides the reference timing signal with high resolution for all detectors. IT is used to measure the beam line TOF between MT and itself, also measure the spectrometer TOF between itself and BT.

BS

BS is a plastic scintillation counter installed in the iron box. BS is 7.2 cm long, 1.9 cm wide and 1.0 cm thick, which was designed to cover the target size. Two 3/4" PMTs (Hamamatsu H3167) are coupled to the sides of the plastic scintillator through light guides as shown in Fig.18. The signal from each anode is amplified and divided by the

Hodoscope	Orientation	Dimension (a)	Segmentation
IT	H	10.0 × 4.0 × 1.0	1
BS	H	7.2 × 1.9 × 1.0	1
FP	H	24.0 × 1.5 × 0.4	16
BP	V	180.0 × 21.0 × 1.0	6

[a] dimension of one element (length × width × thickness (cm^3))

Table 4: Specifications of the scintillator hodoscopes in the spectrometer. The orientation is indicated by the direction of hodoscopes (V: vertical, H: horizontal).

PM amp., and discriminated with a constant fraction discriminator, Phillips 715 (CFD). Discriminated timing signal is read by kinetic F432 FASTBUS TDC. The divided analog signal is read by LeCroy 1885 FASTBUS ADC with the gate width of 150 ns. Typical counting rate of BS was $\sim 6 \times 10^4$/spill under which the scintillator worked stably.

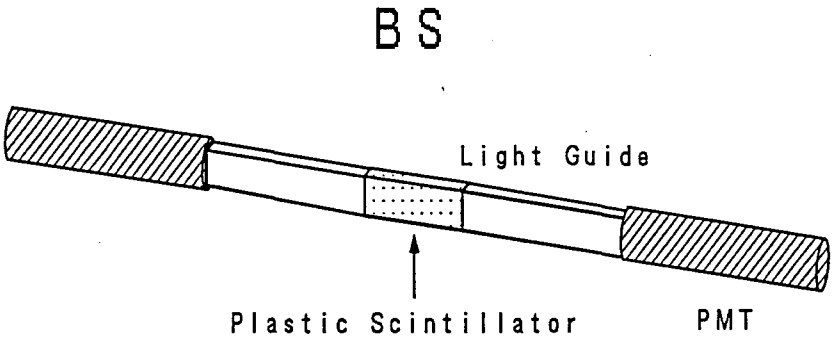

Figure 18: A scintillation counter (BS). Two PMTs are coupled to the plastic scintillator through light guides.

FP and BP

The hodoscopes FP and BP define the acceptance of the 48D48 magnetic spectrometer. In our experiment an outgoing π^- has the same charge as an incoming K^-, which makes difficulties. At forward scattering angles, δ-rays produced by the beam terribly increased trigger rate. FP elements of #12-#16 had to be used as the beam vetoes, and elements of #1-#11 are used to identify the scattering. Therefore, (K^-, π^-) events at vertical angles of more than 0° can not be acquired. As for BP, all elements of #1-#6 are used to identify particles with negative charges.

2.5.3 Čerenkov Counters

For the particle identification, we used three kinds of aerogel Čerenkov counters, IC, FAC and BC and a quartz Čerenkov counter, BQC. Design parameters of aerogel Čerenkov counters are summarized in Table.5.

	IC	FAC	BC
Effective area (X × Y, cm^2)	11.5 × 2.0	10 × 10	126 × 189
Total thickness (cm)	5.8	7.8	9.0
Dimension of a block			
(X × Y × Z, cm^3)	11.4 × 5.4 × 4.1	10 × 10 × 7.8	21 × 21 × 3
Number of block	1	6	162 (6 × 9 × 3)
Refractive index (n)	1.03	1.035	1.04
Threshold momentum (GeV/c)			
for π/K	0.56/1.97	0.52/1.85	0.49/1.74
Photomultiplier	Hamamatsu	Hamamatsu	Burle
	H1161	H5543	8854
Number of channel	4	1	40

Table 5: Design parameters of aerogel Čerenkov counters.

Aerogel Čerenkov Counter (IC)

In order to distinguish a K^- beam from a π^- beam, an aerogel Čerenkov counter (IC) with refractive index of 1.03 was installed between ID2 and IT. Schematic drawings of IC are shown in Fig.19.

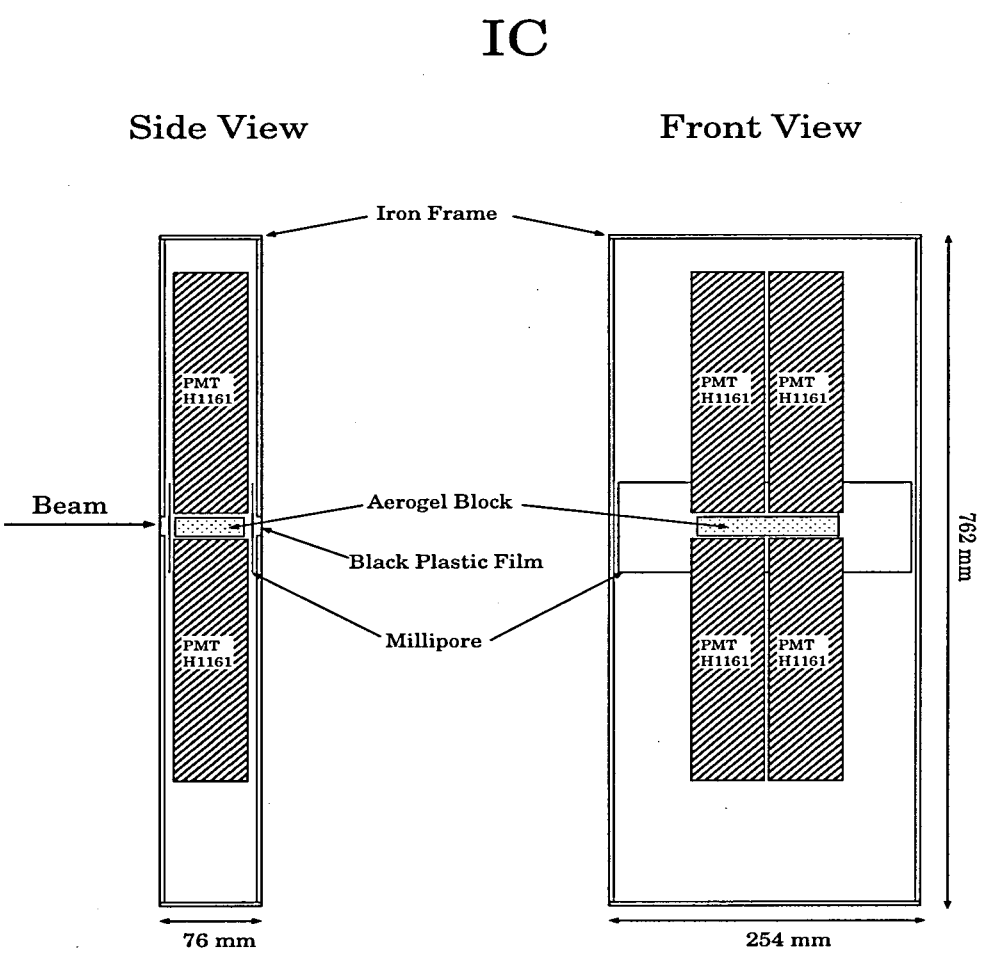

Figure 19: Drawings of the aerogel Čerenkov counter IC.

An active area of IC is 11.5 cm × 2.0 cm × 5.8 cm. For detecting Čerenkov photons, four 2"-diameter PMTs (Hamamatsu H1161) with UVT glass windows were used. Two PMTs were above the aerogel block and others were below it. IC operated at high counting rate under beam-on condition was equipped with PMTs with booster power supplies to hold potentials of the last three dynodes.

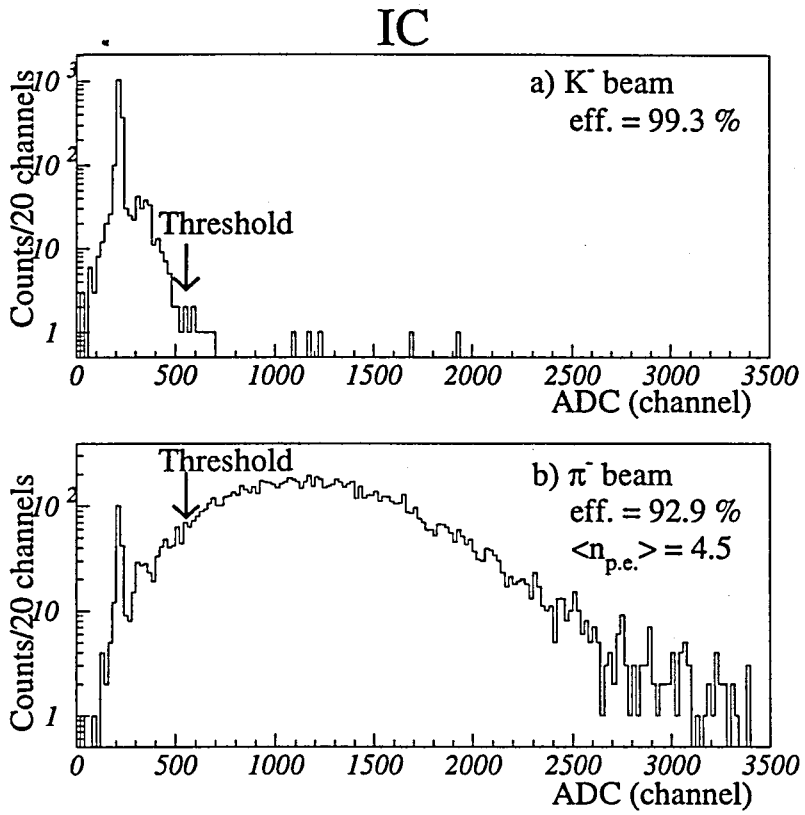

Figure 20: ADC spectra of IC collected with the IT trigger. Upper spectrum is for the K^- beam and lower is for the π^- beam. The threshold of the CFD was set at ~550 channel in the experiment as indicated by arrows.

The performance of IC for both beams of K^- (Upper) and π^- (lower) at 0.93 GeV/c is shown in Fig.20. The data were collected with the IT trigger. The K^- beam is identified by the beam line TOF and the reconstructed mass using the spectrometer to reject the in-flight decay. While the π^- beam is identified by the beam line TOF. Sharp peaks observed at 200 channel correspond to the pedestals. If a threshold were set at 250 channel, a detection efficiency would be more than 98 % for the π^- beam. Since the threshold was set at higher (~550 channel) in order not to decrease the efficiency for the K^- beam, the efficiency for the π^- beam becomes 92.9 %. The efficiency for the K^- beam is 99.3 %, where most of the in-flight decays of K^- are already rejected. These efficiencies would get better if there are not any multi-hits on IC. The average number of photo-electrons is estimated to be about 4.5 for the π^- beam.

Quartz Čerenkov Counter (BQC)

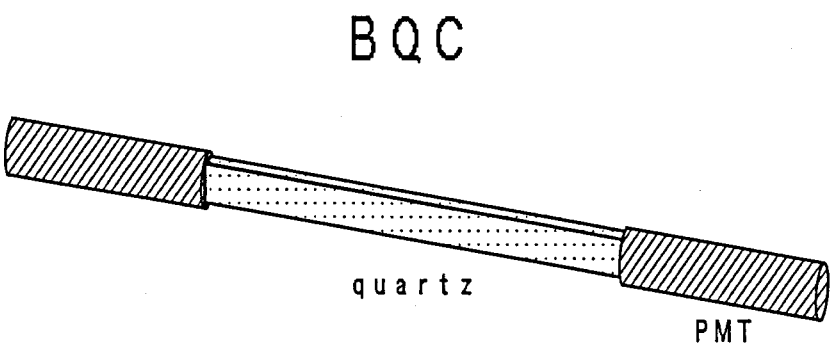

Figure 21: A quartz Čerenkov counter (BQC). Two 9/8" PMTs are directly coupled to the quartz.

BQC is a quartz Čerenkov counter to distinguish the K^- beam from the π^- beam just in front of the target. BQC played an important role in decreasing trigger rate. BQC is 20.0 cm long, 2.0 cm wide and 1.0 cm thick, which was designed to cover the target size. Refractive index of the quartz is 1.46. Two 9/8" PMTs (Hamamatsu H3171) with the UV-transparent glass window are directly coupled to the sides of the plate of quartz as shown in Fig.21. A signal from each anode is amplified and divided by the PM amp., and discriminated with a constant fraction discriminator, Phillips 715 (CFD). The discriminated timing signal is read by kinetic F432 FASTBUS TDC. The divided analog signal is read by LeCroy 1885 FASTBUS ADC with the gate width of 150 ns.

When a particle moving with velocity β orthogonally passes through a plate with refractive index n, the Čerenkov radiation is emitted as shown in Fig.22. A particle emitting the Čerenkov radiation must have a velocity

$$\beta > 1/n. \tag{14}$$

Principle of the Čerenkov counter is based on the mechanism of the total reflection of the Čerenkov light. The emitted angle is well defined as

$$\theta_C = cos^{-1}(1/\beta n). \tag{15}$$

The critical angle for the total reflection $\theta_{crit.}$ is given by

$$\theta_{crit.} = sin^{-1}(n_0/n), \tag{16}$$

where n_0 is the refractive index of the medium outside the plate. Therefore, the threshold velocity $\beta_{th.}$ for the total reflection is given by

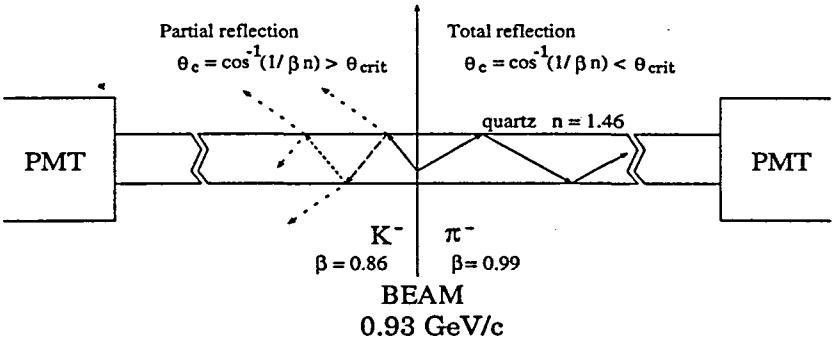

Figure 22: Principle of a Čerenkov counter based on the total reflection of light.

$$\beta_{th.} = \frac{1}{\sqrt{n^2 - n_0^2}}. \tag{17}$$

In case of a particle with higher β, the Čerenkov angle θ_C is large enough for the total reflection on the surface of the plate. Consequently the light is detected by PMTs coupled at both sides. On the other hand, in case of a slow particle, the light is partially reflected and escapes the plate after reflections of a few times.

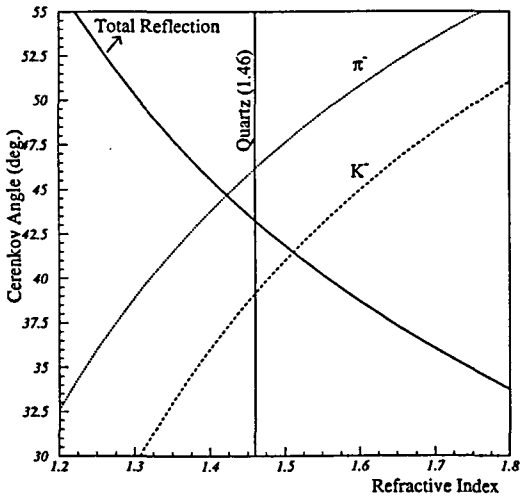

Figure 23: Relations between refractive index of material and Čerenkov angle for π^- (dotted curve) and K^- (dashed curve) at the beam momentum of 0.93 GeV/c. The solid curve indicates critical angle for the total reflection.

For examples, a π^- (β=0.989) and a K^- (β=0.883) with the momentum of 0.93 GeV/c emit Čerenkov radiation at 46.2° and 39.2°, respectively, while critical angle for the total reflection is 43.2° in the quartz as shown in Fig.23. Therefore, the π^- is detected and the K^- is not. The quartz is one of the most suitable materials for the Čerenkov counter at the beam momentum of 0.93 GeV/c.

Fig.24 shows ADC spectra of BQC collected with the IT trigger. The ADC spectra are the average pulse heights of left and right PMTs' for the K^- beam (a) and for the π^- beam (b). The K^- beam is identified by the beam line TOF and by the reconstructed mass using the spectrometer for rejecting the effect due to the in-flight decay of K^-. While the π^- beam is identified only by the beam line TOF. Since about 30 % of particles passing through IT didn't hit BS, events with both hits on BS and LT1 are selected. BQC was placed between them. The threshold of the CFD for BQC was set at ~550 channel during the experiment. Pedestal events which were subtracted by the DAQ system are plotted at negative region of the ADC spectra. The detection efficiency for the K^- beam is 99.9 %, which verifies high ability of BQC. While the efficiency for the π^- beam is 97.2 %. A separation between the K^- beam and the π^- beam looks extremely fine in the figures. The average number of photo-electrons is estimated to be 32.5 for the π^- beam by assuming the Pisson distribution to have the Gaussian form for large $\langle n_{p.e.} \rangle$.

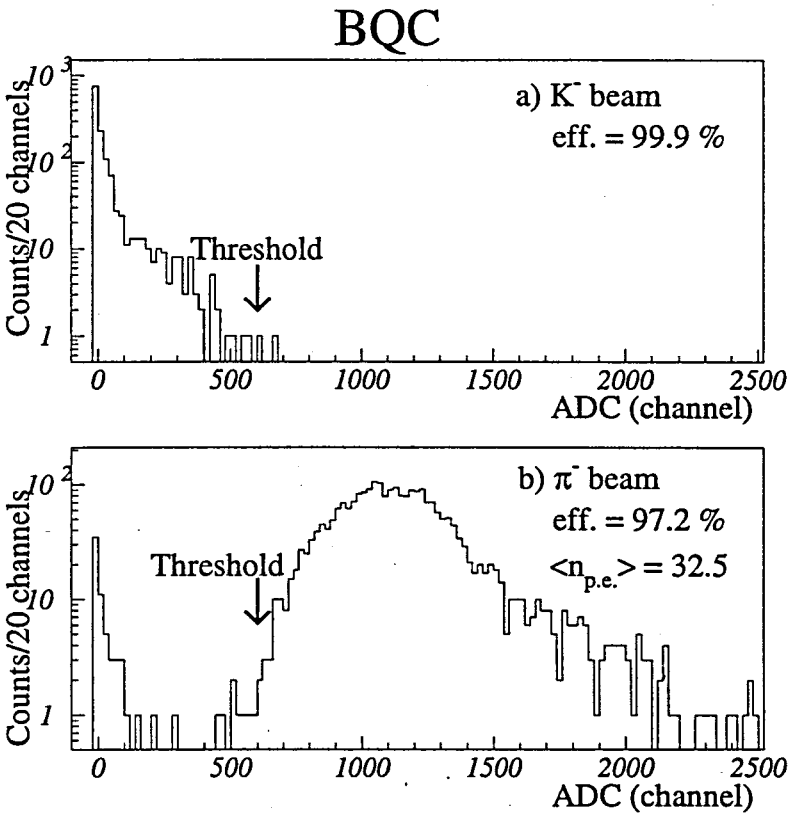

Figure 24: ADC spectra of BQC collected with the IT trigger for the K^- beam (a) and for the π^- beam. Pedestals subtracted by the DAQ system were plotted at negative regions. The threshold of the CFD during the experiment was set at ~600 channel as indicated by arrows.

Aerogel Čerenkov Counter (FAC)

FAC is an aerogel Čerenkov counter to identify outgoing π^- particles. FAC was installed just behind the target for suppressing the in-flight decays of K^- as much as possible. Since they occupied most of trigger rate, FAC played an important role. An active area of FAC is 10.0 cm × 10.0 cm × 7.8 cm. FAC consists of six aerogel sheets with refractive index of 1.035, and each sheet is 10.0 cm × 10.0 cm × 1.3 cm. The active area sufficiently covers the scattering angles of 0° to 16° which is needed in the experiment. A Gortex was placed as a reflection mirror for the detection of Čerenkov radiation as shown in Fig.26. A finemesh type 3" PMT (Hamamatsu H5543) was used to maintain enough gain even installed near the spectrometer with high magnetic field. Since FAC was operated at high counting rates under beam-on condition, it was equipped with the PMT with booster power supplies to hold potentials of the last two dynodes.

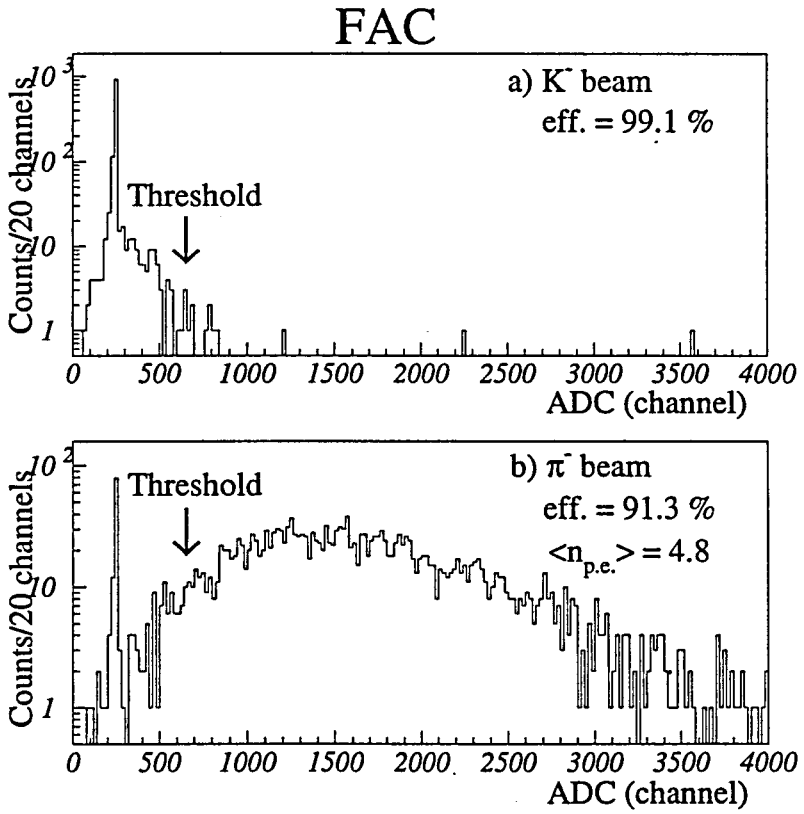

Figure 25: ADC spectra of FAC collected with the IT trigger. Arrows indicate the threshold of the CFD (~650 channel) in the experiment.

The performance of FAC with the IT trigger is shown in Fig.25, where the upper ADC

spectrum is for the K^- beam and the lower is for the π^- beam at the beam momentum of 0.93 GeV/c. The K^- beam is identified by the beam line TOF and by the reconstructed mass using the spectrometer for rejecting the effect due to the in-flight decay of K^-. While the π^- beam is identified only by the beam line TOF. Events with hits on LT4 are selected in order to exclude particles scattered at large angles upstream FAC. If the threshold were set at 300 channel, a detection efficiency of FAC would be more than 95 % for the π^- beam. The effects of the scattering and interactions in LT4 and the multi-hits are considered to be relatively large because the efficiency measured before the experiment without the target was more than 99 %. The efficiency measured with FAC tilted by 15° for the π^- beam also maintained more than 99 %. It showed that the efficiency was independent of the scattering angles. The trigger rate was so high for the DAQ system that the threshold of CFD had to be set at higher (~650 channel) during the experiment. By virtue of the higher threshold, total trigger rate became about 200 events/spill that was acceptable for the DAQ system. A δ-ray produced by the K^- beam was one of the main reasons to increase trigger rate. The detection efficiencies of FAC are 91.3 % for the π^- beam and 99.1 % for the K^- beam, which is not satisfactory results for us. The average number of photo-electrons is estimated to be about 4.8 for the π^- beam.

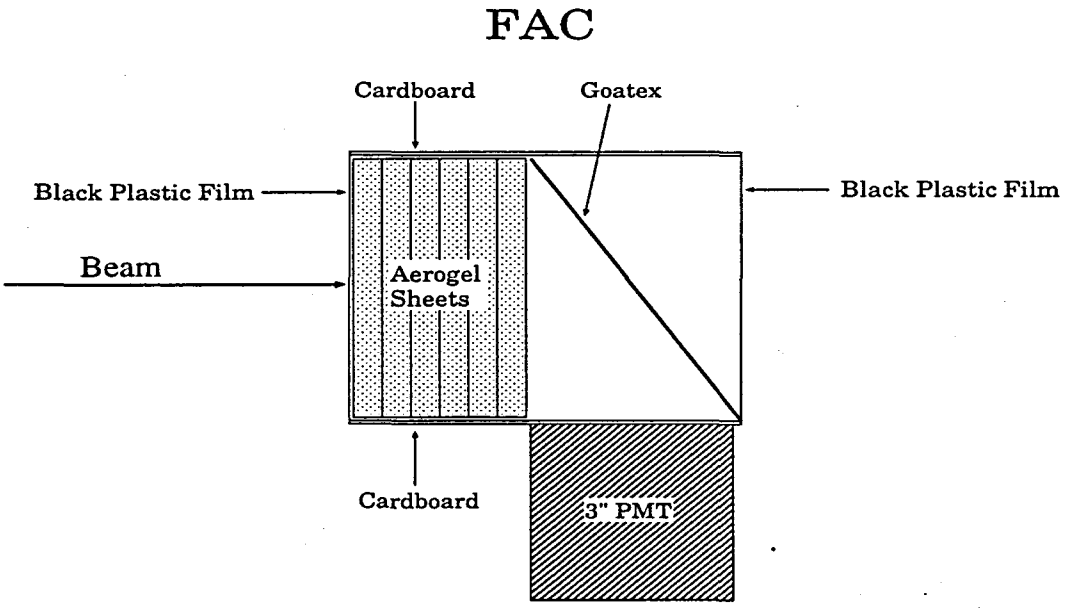

Figure 26: An aerogel Čerenkov counter (FAC) installed just behind the target. It consists of six sheets of aerogel whose refractive index is 1.45.

Aerogel Čerenkov Counter (BC)

In the previous (K^-, K^+) experiments, an aerogel counter BC had been installed in the spectrometer for the rejection of π^+ produced in the target [41][42][43]. Refractive index of the aerogel was 1.04. The aerogel blocks were manufactured by the Airglass Company in Sweden. The aerogel blocks were kept in dry nitrogen gas flow during the experiment. The radiator cells were coated with highly reflective white paper (millipore) to prevent absorption of Čerenkov radiation, and a mirror of aluminized mylar was arranged in parabolic shape as shown in Fig.27. For detecting the Čerenkov photons, 40 5" PMTs sensitive to a single photo-electron, Burle 8854 were used. The high voltages supplied to PMTs were adjusted to give an equal gain by flushing green LEDs installed in BC. Each PMT was placed inside a 1/4"-thick magnetic shield made of iron. A μ-metal pipe extended by about 3" from the cathode surface plays an important role in reducing the magnetic field effect on the performance of the PMT. A collar of aluminized mylar was installed in front of the PMT to increase the light yield. Since the performance of FAC installed just behind the target was fine enough for identifying (K^-, π^-) reactions, the signal from BC was not used to form the trigger. Althogh both informations on the timing and the pulse height were acquired in the data, they were not used in the off-line analysis consequently.

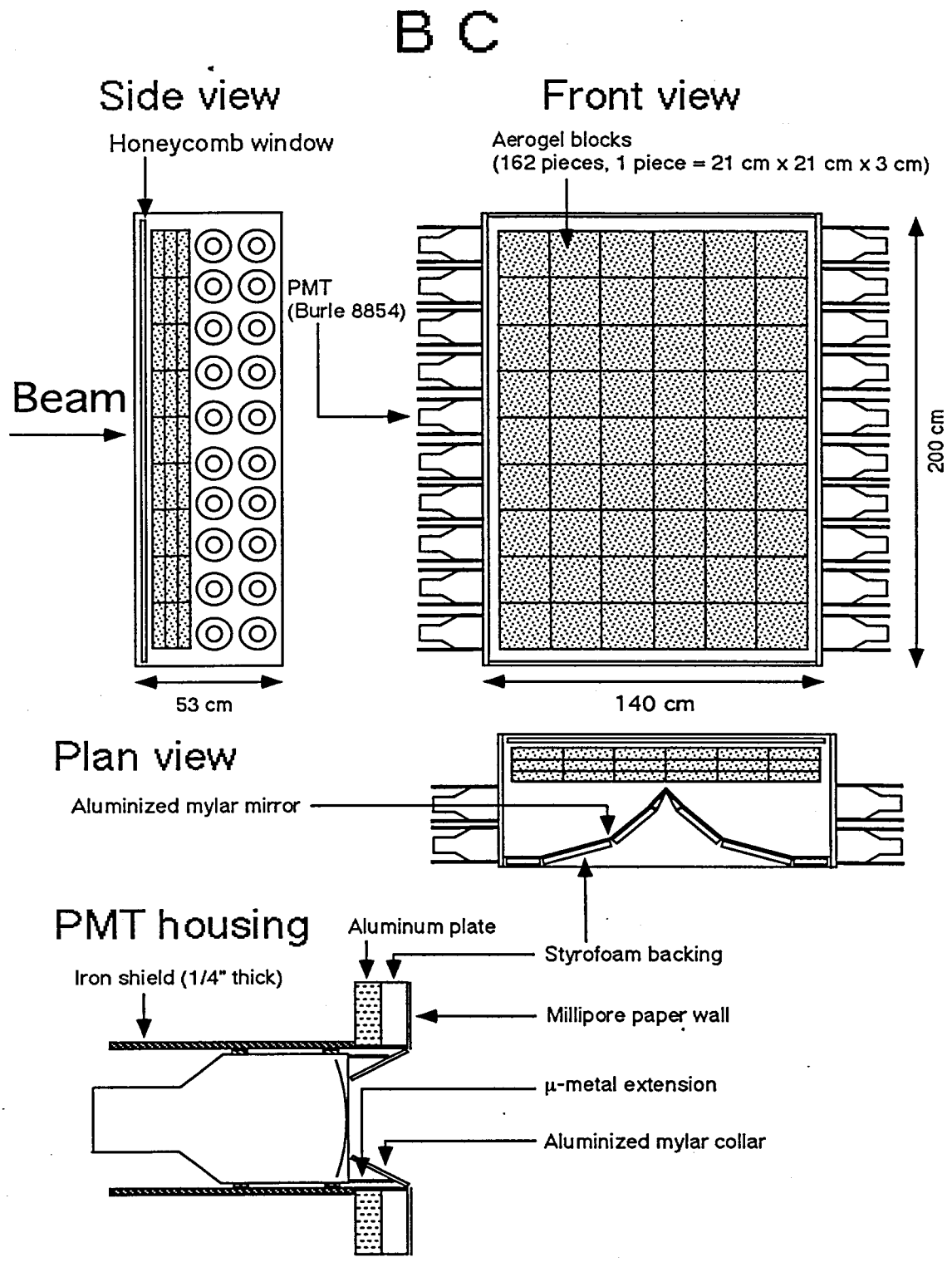

Figure 27: Drawing of aerogel Čerenkov counter BC. The housing structure of a PMT is also shown.

2.5.4 Drift Chambers

The spectrometer was equipped with two drift chambers (ID1,2) for the tracking of incident beam particles and with five drift chambers (FD1-3 and BD1,2) for reconstructing the track of outgoing particles through the magnet. Table.6 shows the specification of the drift chambers. An outgoing particle is bent vertically by 48D48 spectrometer, therefore the vertical (y) position is closely related to its momentum. For better resolution in the x position, FD1-3 and BD1-2 are designed with the plane configuration of y-u-v. In contrast, ID1-2 are designed with the plane configuration of x-u-v to give a better resolution in the x position. The gas mixture used to operate the drift chambers was 77 % argon, 20 % isobutane and 3 % methylal. The two drift chambers of ID1-2 are identical and so are FD1-2. The drift cell of these chambers are designed for the operation at high beam rate. Sense wires are positioned with a 5.1mm (0.2") spacing, thus the maximal drift distance is 2.5 mm giving the maximal drift time of 50 ns. FD3 chamber is installed inside the magnet for better determination of the momentum. BD1-2 chambers have the active area of 124 cm $\times$ 224 cm. They have a similar design of drift cells with sense wires placed with 2.0 cm spacing. The position resolution (σ) of the drift chambers are 0.2 mm for ID1-2 and FD1-2, 0.3 mm for FD3 and 0.4 mm for BD1-2.

	Plane	Orientation	Sense area		Active area	Location	Resolution
			spacing (mm)	# channel	(X × Y, cm^2)	(Z, cm)	(σ, mm)
	u-u'	120°	5.08	24 × 2		-140.0	
ID1	v-v'	60°	5.08	24 × 2	12.2 × 10.6	-139.1	0.2
	x-x'	0°	5.08	24 × 2		-138.2	
	u-u'	120°	5.08	24 × 2		-105.9	
ID2	v-v'	60°	5.08	24 × 2	12.2 × 10.6	-105.0	0.2
	x-x'	0°	5.08	24 × 2		-104.1	
	u-u'	210°	5.08	48 × 2		28.3	
FD1	v-v'	150°	5.08	48 × 2	21.2 × 24.4	29.2	0.2
	y-y'	90°	5.08	48 × 2		30.1	
	u-u'	210°	5.08	48 × 2		62.0	
FD2	v-v'	150°	5.08	48 × 2	21.2 × 24.4	62.9	0.2
	y-y'	90°	5.08	48 × 2		63.8	
	u	150°	12.7	64		139.4	
FD3	y	90°	12.7	64	45.7 × 81.3	141.3	0.3
	y'	90°	12.7	64		142.5	
	v	30°	12.7	64		144.4	
	y	90°	20.0	112		364.2	
BD1	u	120°	20.0	128	114.0 × 214.0	365.4	0.4
	v	60°	20.0	128		366.6	
	y'	90°	20.0	112		367.8	
	y	90°	20.0	112		446.3	
	u	120°	20.0	128		447.5	
BD2	v	60°	20.0	128	114.0 × 214.0	448.7	0.4
	y'	90°	20.0	112		449.9	
	v'	60°	20.0	128		451.1	

Table 6: Design parameters of the drift chambers.

2.5.5 TOF Wall (BT)

BT is the last detector to measure TOF between IT and itself. An active area of the BT is 2.0 × 3.2 m^2. BT is inclined at 15° which is different from the inclined angle of other detectors (30°). The inclined angle is chosen that outgoing particles with the same momentum scattered at different angles have as same path length as possible. It was designed to minimize the TOF spread of proton which was the main background of previously performed (K^-, K^+) experiments. A typical flight length is 7.9 m from the target. In case of our experiment, it gives TOF difference of 3.8 ns between K^- and π^- at the outgoing momentum of 0.84 GeV/c. The BT consists of 40 elements of plastic scintillators (BC408) arranged as illustrated in Fig.28. Each element is 200.0 cm long, 8.5 cm wide and 5.0 cm thick. Essentially, two 2"PMTs (Hamamatsu H1949) are coupled to both sides of the scintillator without light guides. A signal from each anode was divided by a handmade splitter. The divided signal was discriminated with a CFD. The discriminated timing signal was read by kinetic F432 FASTBUS TDC, which provides a fine timing resolution of 25 ps/channel. The divided analog signal is read by LeCroy 1885 FASTBUS ADC with the gate width of 150 ns. The whole elements were tested with the beam by changing the field of the magnet, and the TOF resolution averaged over 40 elements was found to be 130 ps (σ). By unfolding the resolution of the START signal (60 ps), the intrinsic timing resolution of 110 ps (σ) was obtained. The effective light velocity in the element was obtained as 15.0 ± 0.4 cm/ns. Details of the design and the device performance are described in Ref.[44]

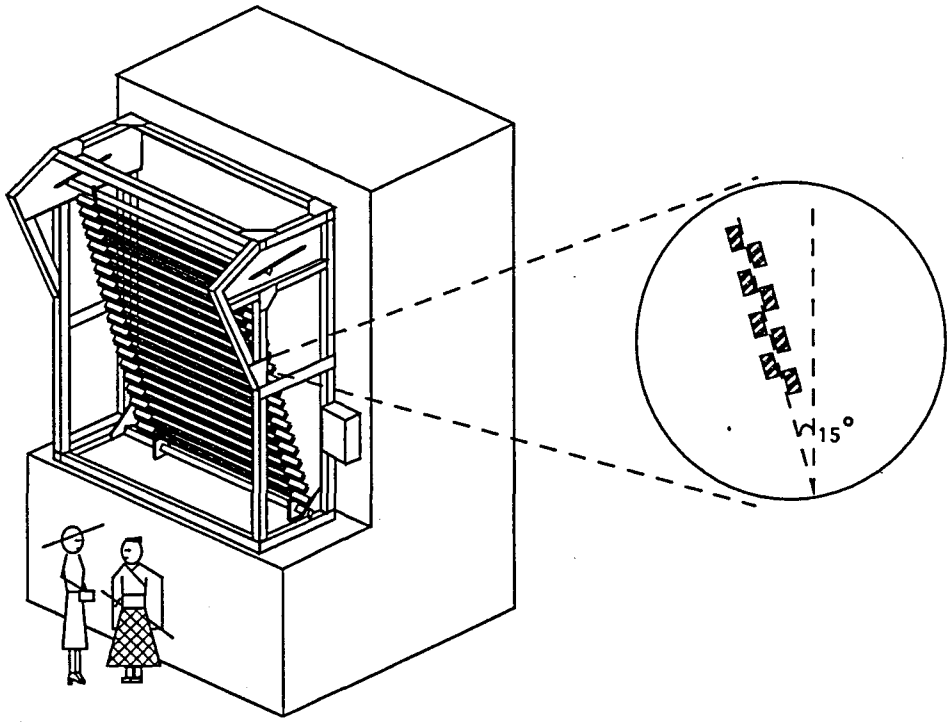

Figure 28: Layout of the time-of-flight wall BT.

2.6 Other Detectors around Target

There were other detectors which were of great importance around the target. An active target was used to form the trigger, and it played an important role in suppressing background. Four plastic scintillation counters (DEC) were used to detect decay particles. Eight plastic scintillation counters (VETO) were installed on the NaI detector to reject charged particles. 72 NaI detectors which were the main device in the experiment were installed at 10.5 cm from the target center for the detection of γ-rays as shown in Fig.14.

2.6.1 Active Target (LT)

An active target (LT) has four segments, and each segment is a liquid scintillator contained in a quartz cell. Inner size of the cell is 6.0 cm wide, 1.5 cm high and 3.0 cm thick. Thickness of the quartz is 1 mm. The width and height were determined from the beam profile obtained by the test experiment performed in 1997. Two 3/4" PMT (Hamamatsu H3167) are coupled to the sides of the quartz cell through light guides as shown in Fig.29.

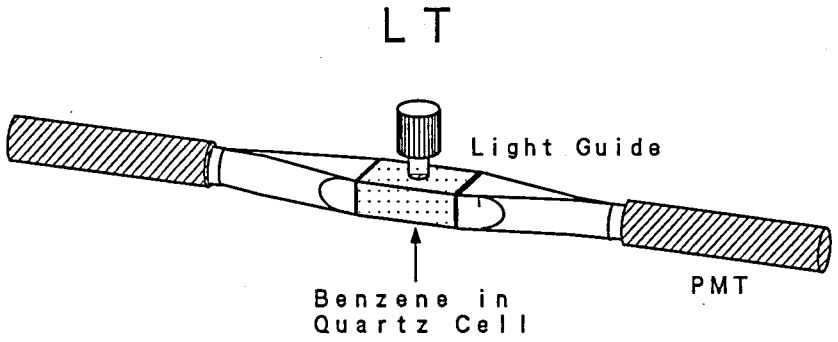

Figure 29: A segment of LT. The liquid scintillator is in the quartz cell. Two 3/4" PMTs are coupled to the quartz cell through the light guides.

In the experiment, IC, BQC and FAC were used to identify incoming and outgoing particles respectively. Even if the particle identification is effectively performed, there are still in-flight decays of K^- between BQC and FAC (about 15 cm in distance) remained as background. A K^- particle dominantly decays to $\mu^-+\bar{\nu}_\mu$ (63.5 %) and $\pi^-+\pi^0$ (21.2 %). The $K^- \rightarrow \pi^-+\pi^0$ decay is the direct background when we identify (K^-, π^-) reaction. In addition, the $K^- \rightarrow \mu^-+\bar{\nu}_\mu$ decay is also another background because 48D48 spectrometer can not separate the small mass difference between μ^- and π^-. The decay rate of K^- is huge compared with ^{13}C(K^-, π^-) event rate, therefore most of triggered events are coming from the background events.

One method to identify the formation of the hypernucleus is the detection of its weak decay. For hypernuclei heavier than A=5, the dominant modes of the weak decay are

non-mesonic decay processes such as $\Lambda p \rightarrow np$ and $\Lambda n \rightarrow nn$. About half of the non-mesonic decays produce an energetic proton with the energy distribution of a few tens MeV to 120 MeV. Since the lifetime of hypernuclei is similar to that of the free Λ and the lifetime is much shorter than the response times of scintillation counters, the energy deposit of the decay proton is added to that of the (K^-, π^-) reaction.

2.6.2 Decay Particle Counters (DEC)

DEC is the plastic scintillation counter installed just above and below the target as shown in Fig.14. DEC is consists of four segments, and the size of each segment is 24.0 $\times$ 15.0 $\times$ 1.5 cm^3. A 2" PMT (Hamamatsu H1161) is coupled to the plastic scintillator through a light guide as shown in Fig.30. The signal from an anode is divided by a handmade splitter, and discriminated with a discriminator. The discriminated signal was read by kinetic F432 FASTBUS TDC. The divided analog signal is read by LeCroy 1885 FASTBUS ADC with the gate width of 150 ns. DEC detects charged particles emitted by the weak decay of ${}^{13}_{\Lambda}$C, which increase the detection efficiency of the weak decay as shown in Fig.51.

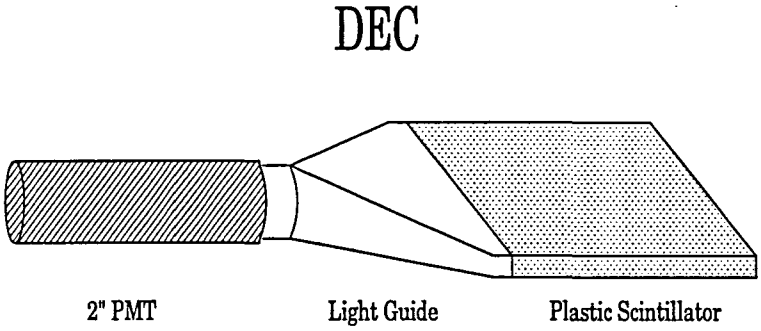

Figure 30: A segment of DEC.

2.6.3 Charged Particle Veto Counters (VETO)

VETO is eight plastic scintillation counters installed on NaI detectors as shown in Fig.31. Size of each segment is 42.0 cm long, 10.0 cm wide and 1.0 cm thick. Two 2" PMT (Hamamatsu H1161) are coupled to the sides of the plastic scintillator through light guides. The signal from each anode is divided by a handmade splitter, and discriminated with a discriminator. The discriminated signal was read by kinetic F432 FASTBUS TDC. The divided analog signal is read by LeCroy 1885 FASTBUS ADC with the gate width of 150 ns. VETO was used to reject charged particles emitted by the weak decay of ${}^{13}_{\Lambda}$C. When there is a signal from a VETO segment, informations of NaI detectors covered with the VETO segment are not used in the analysis. Concrete event selections with VETO is to be described below.

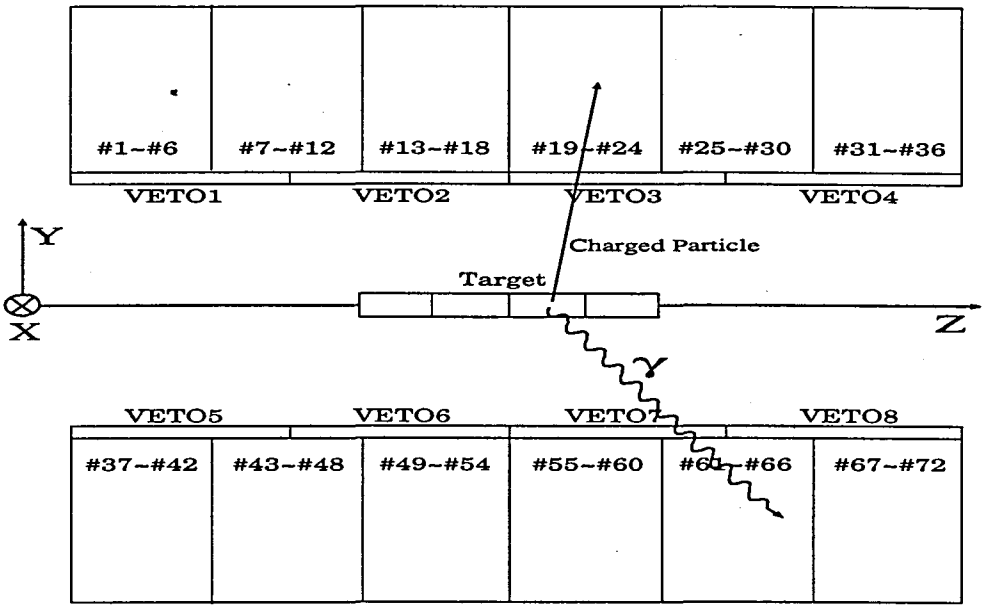

Figure 31: Side view of VETO and NaI detector.

2.6.4 NaI Detectors

The NaI detector is suitable device for the detection of γ-rays by virtue of its high Z. Density of the NaI crystal is 3.67 and radiation length is 2.59 cm. In case of the detection of a high energy γ-ray ($\sim$11 MeV), total absorption coefficients of the NaI crystal is μ=0.15 cm^{-1}. Most part of which is due to the pair creation $\sim$0.10 cm^{-1} and the compton scattering $\sim$0.05 cm^{-1} [45].

The NaI detector was installed at a distance of 10.5 cm from the target center. The NaI detector has 72 segments (6 $\times$ 6 up, 6 $\times$ 6 down) to endure high counting rate. It is quite convenient to correct a measured energy of γ-ray by calculating the Doppler shift effect. In case of using the NaI detector, it is particularly important to care for the counting rate and high voltage supplied to the PMT. It is so weak in the high counting rate because of its long decay constant 230 ns that it may cause a gain shift under beam-on conditions. A typical counting rate was $\sim 5 \times 10^3$ counts/s at the K^- beam intensity of 5×10^4/spill on the target. All NaI detectors covered the solid angle of $\sim$60 % of 4π. An active area of each NaI crystal is 2.5" $\times$ 2.5" $\times$ 12.0", which is thick enough to detect a high energy γ-ray ($\sim$11 MeV). The high energy γ-ray is energetic enough to produce a shower. Accordingly, in the off-line data analysis energies of a few NaI detectors are added to obtain full energy peak efficiently. A 2" PMT (Hamamatsu H1161) is connected to the NaI crystal through a silicon rubber and a light guide as shown in Fig.32. The PMT is covered with triple shield cases against the magnetic field for obtaining an enough gain near the magnetic spectrometer. LED light delivered by an optical fiber is used for the gain monitor. For operating the detectors stably we used handmade TFAs to maintain

high gains with lower HV for the PMTs. The signal from an anode was divided by the TFA, and discriminated with a CFD. The discriminated signal was used to form the self trigger for the energy calibration of the NaI detector. The analog signal was divided again by a handmade splitter by the ratio of 6:1. The divided larger signal was discriminated with a discriminater. The discriminated signal was read by kinetic F432 FASTBUS TDC. The divided analog signal was read by LeCroy 1885 FASTBUS ADC with the gate width of 1 μs.

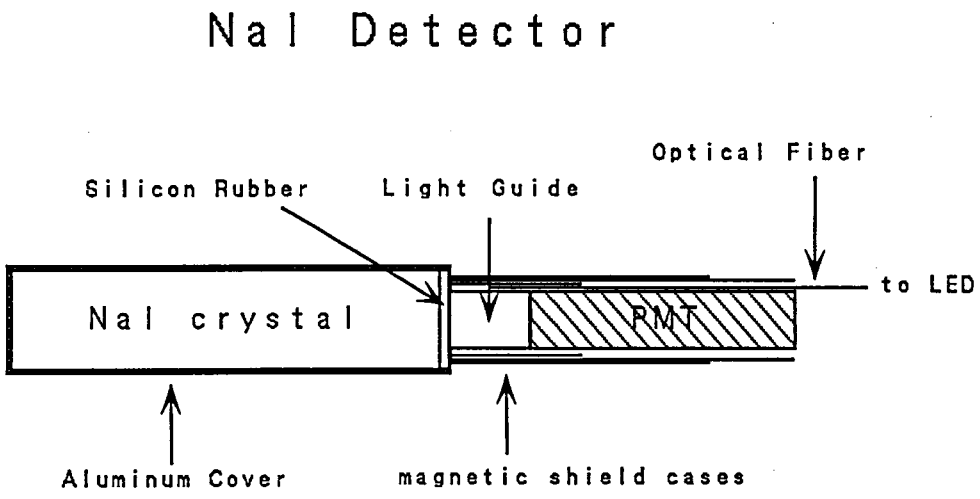

Figure 32: Drawing of a NaI detector. A NaI crystal is covered with aluminum. A PMT is covered with triple shield cases against the magnetic field.

2.7 Energy Calibration of NaI Detector

We measure high energy γ-rays ($\sim$11 MeV) accurately, therefore the energy calibration of the NaI detector is particularly important in the experiment. Before the experiment, we planned to use two γ-rays from the quasi-free scattering of $^{13}C(K^-, \pi^- \Lambda)^{12}C$ for the correction of the γ-ray energy. One is a γ-ray from the 2^+ state at 4.439 MeV, and the other is from the 1^+ state at 15.1 MeV (T=1) to the ground state in ^{12}C. However, in the off-line data analysis we gave up using the γ-rays because of insufficient statistics of their peaks. As a result, we used two methods for the energy calibration.

2.7.1 ^{22}Na source

^{22}Na decays to the first excited state (2^+, 99.96 %) in ^{22}Ne by emitting a positron [46]. The life time of this β^+ decay is 2.602 y. The first excited 2^+ state decays to the ground state (0^+, 100 %) in ^{22}Ne by emitting a γ-ray with the energy of 1.275 MeV. The life time of the state is 3.63 ps. The positron also emits two γ-rays with the energy of 0.511 MeV by annihilation. We used the ^{22}Na source for a low energy calibration of the NaI detector. It also played an important role in correcting a gain drift in the long term.

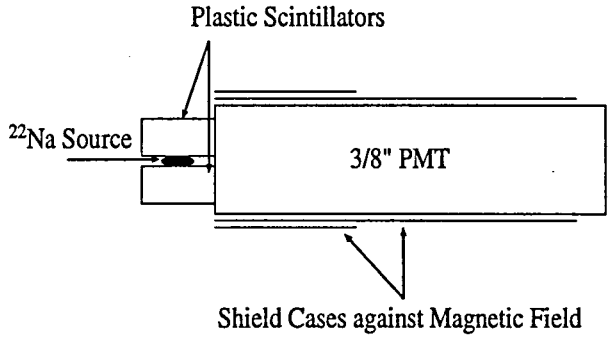

Figure 33: ^{22}Na source.

A ^{22}Na source is sandwiched between two plastic scintillators with a size of 8 mm $\times$ 8 mm $\times$ 4 mm as shown in Fig.33. A 3/8" PMT (H1635) is coupled to them by the optical grease. The PMT is covered with double shield cases against the magnetic field. The signal from anode is discriminated with a constant fraction discriminator, Phillips 715 (CFD) to form the trigger. Since the trigger timing of the source had better be same as the (K^-, π^-) trigger timing, the β-γ source was quite suitable in our experiment.

Fig.34 shows an energy spectrum of the γ-rays by using the ^{22}Na source in the energy calibration run under beam-off condition. The trigger was formed by the coincidence with the discriminated signal from the NaI detector. The energy threshold of the CFD was set at $\sim$1 MeV. Two peaks which correspond to the 1.275 MeV γ-ray and the 0.511 MeV γ-ray are clearly observed. A small structure at $\sim$1.8 MeV corresponds to events which both γ-rays simultaneously entered a NaI crystal.

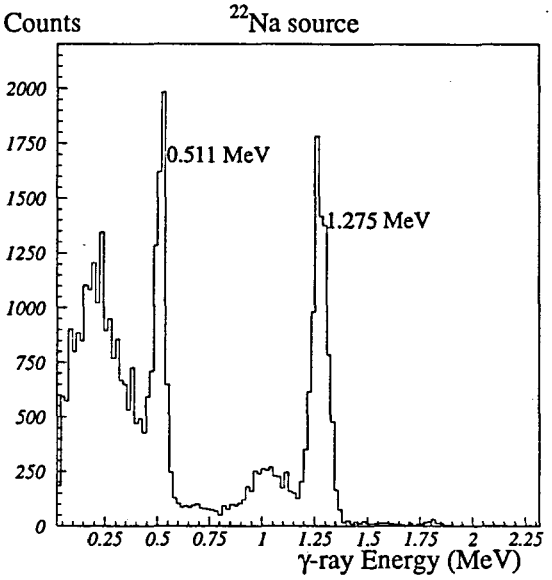

Figure 34: typical energy spectrum of γ-ray using the ^{22}Na source.

2.7.2 ^{58}Ni(n, γ) reaction

For the energy calibration at high energy region, we used ^{58}Ni(n, γ) reaction using a neutron source of ^{244}Cm^{13}C. Fig.35 shows an energy spectrum of γ-rays obtained in the energy calibration run under beam-off condition. In the off-line analysis only events with single hit in a cluster were selected. A clear peak corresponding to the 8.999 MeV γ-ray emitted by the ^{58}Ni(n, γ) reaction is clearly observed. The γ-ray is from the neutron emission threshold to the ground state in ^{59}Ni. Another γ-ray peak at $\sim$8.5 MeV is also observed. It can be considered that the peak is composed of two peaks. One is a single escape peak of the 8.999 MeV γ-ray expected to lie at 8.488 MeV. The other is the 8.534 MeV γ-ray from the neutron emission threshold to the $1/2^-$ second excited state in ^{59}Ni. This method of the energy calibration is quite useful because the emitted γ-ray energy is close to 11 MeV. A 6.826 MeV γ-ray is emitted by ^{127}I(n, γ) reaction in the NaI crystal. The γ-ray peak was not used for the energy calibration. Because the γ-ray was not from the target, but from the NaI crystal itself. It is not ideal to use γ-rays emitted from other than target position. The most dominant γ-ray at 6.129 is emitted by the ^{13}C(α, n γ)^{16}O reaction, where an α particle is emitted by a ^{244}Cm nucleus which is surrounded by ^{13}C nuclei. A single escape peak of the γ-ray is separately observed. A peak at 4.439 MeV is considered to be emitted by some reactions on ^{12}C.

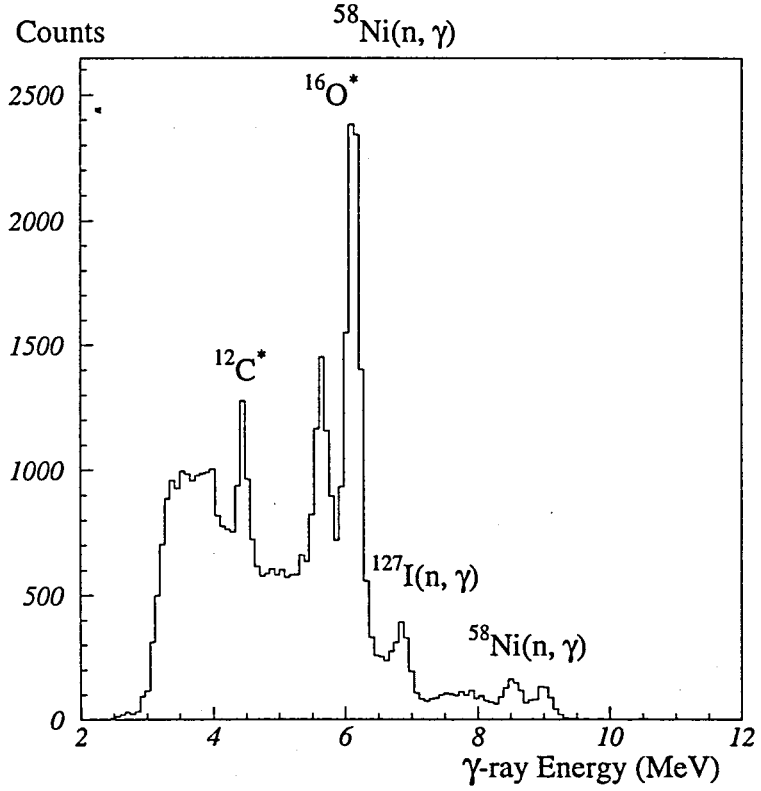

Figure 35: Typical energy spectrum of the ^{58}Ni(n, γ) reaction by using the ^{244}Cm^{13}C neutron source.

Three plates of ^{58}Ni were placed in the center of the NaI detectors as shown in Fig.36. This position was the same as the target. During the energy calibration, the iron box with BS, BQC and LT and DEC were removed. Size of a plate of ^{58}Ni is 5.0 cm $\times$ 5.0 cm $\times$ 0.5 cm. To modulate the neutron kinetic energy suitable for the neutron capture reaction, CH surrounds the neutron source and the plates of ^{58}Ni.

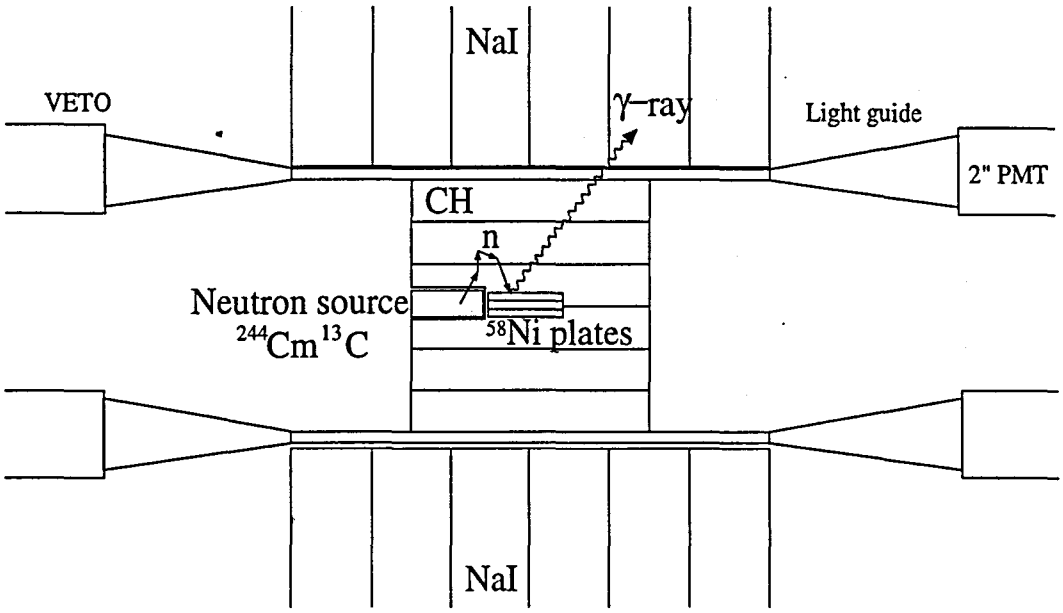

Figure 36: Setup for the high energy calibration of the NaI detector. During the calibration, the iron box in which BS, BQC and LT were installed and DEC were removed. Three plates of ^{58}Ni were placed at the same position as the target.

2.7.3 Linearlity of Energy Calibration

A linearlity of an energy calibration for a typical NaI detector is shown in Fig.37. Lower three data points which correspond to peaks of pedestal (0 MeV), annihilation (0.511 MeV) and ^{22}Ne (1.275 MeV) were collected in the energy calibration run using a ^{22}Na source. Higher two data points which correspond to ^{16}O (6.129 MeV) and ^{59}Ni (8.999 MeV) were collected in the ^{58}Ni(n, γ) energy calibration run using a ^{244}Cm^{13}C source. Both calibration runs were performed under beam-off conditions. Position of pedestal was not changed in the runs. In the figure, a linear relation between the γ-ray energy and the ADC channel is obviously confirmed, which is also confirmed for other NaI detectors.

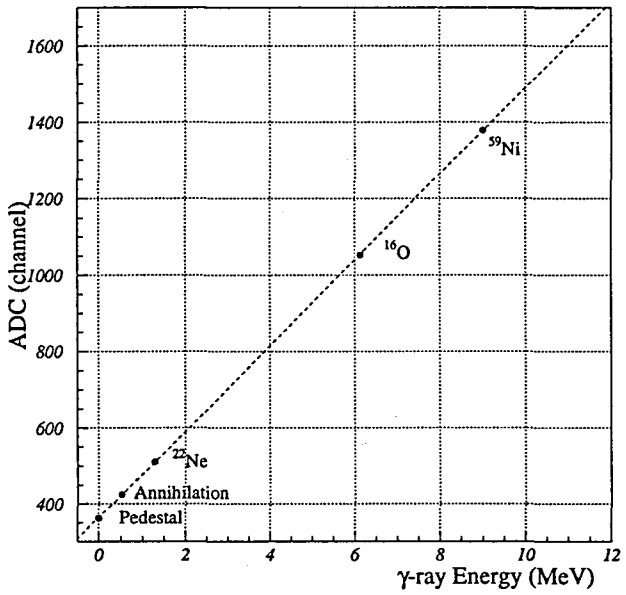

Figure 37: Linearlity of a typical energy calibration. Horizontal axis indicates the γ-ray energy. Vertical axis indicates the ADC channel. Closed circles are data points collected in the calibration run under beam-off conditions.

2.7.4 Energy Resolution of NaI detector

The energy resolution of the NaI detector has dependence on the γ-ray energy mainly due to statistics of the electron collection by PMT. Therefore, it almost follows a relation,

$$\Delta E \propto \frac{1}{\sqrt{E_\gamma}} + C, \tag{18}$$

as shown in Fig.38. The plotted data were typical energy resolutions of the central detector measured in the calibration run under beam-off condition. The 0.511 MeV (annihilation) and 1.275 MeV (^{22}Ne) γ-rays are emitted from the ^{22}Na source. The 4.439 (^{12}C) and 6.129 MeV (^{16}O) γ-rays are from the neutron source of ^{244}Cm^{13}C. The 8.999 MeV γ-ray is emitted by the ^{58}Ni(n, γ) reaction. Estimated energy resolution of the central detector is $\sim$280 keV (2.5 %) for the 11 MeV γ-ray under beam-off condition. The energy resolution is about an order-of-magnitude better than that of the magnetic spectrometer ($\sim$2 MeV). It is one of the most important advantages of our experiment, and it enables us to extract the spin-orbit splitting in $^{13}_{\Lambda}$C with an order-of-magnitude better precision.

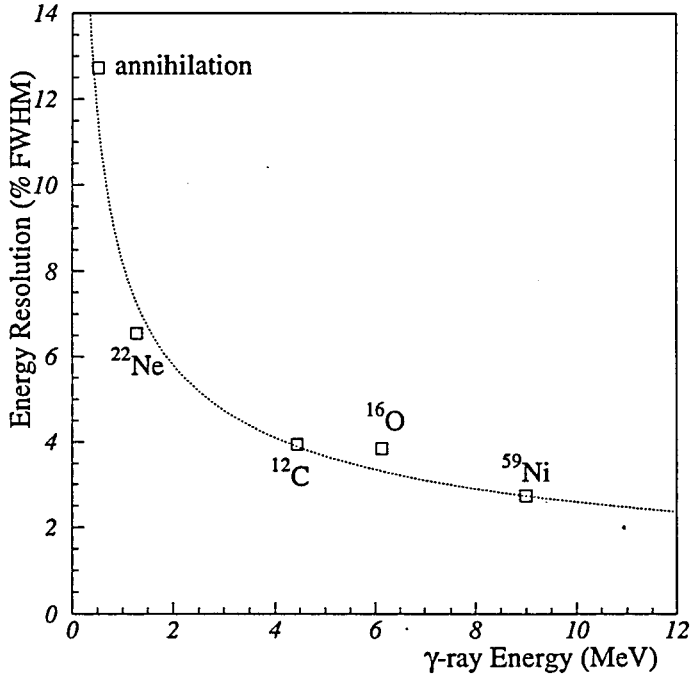

Figure 38: The energy dependence of the energy resolution of a typical NaI detector installed in the center. A fit to the data points are performed with the function of $8.2/\sqrt{E_\gamma}$.

The energy resolutions of all the NaI detectors used in the experiment are shown in Fig.39, where the module number and the energy resolution (% FWHM) measured using the ^{22}Na source (1.275 MeV) are written. NaI detectors with better energy resolution were installed in the center. Energy resolutions of the outer detectors are about 1.5 times worse than those of the center detectors.

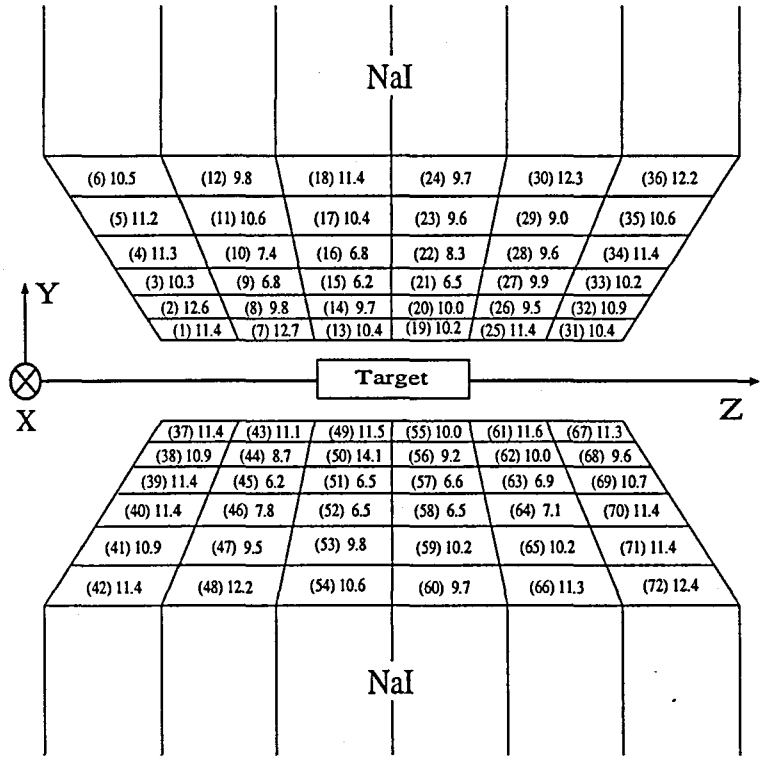

Figure 39: The energy resolutions of all the NaI detectors measured using the 1.275 MeV γ-ray under beam-off condition. The module number and the energy resolution are written.

2.8 Energy Correction of Doppler Shift

When we measure γ-rays emitted by hypernucleus, it is quite important to know if γ-rays are emitted during moving or after the stop. In case of $\sim$11 MeV γ-rays from the $1/2^-$ and the $3/2^-$ states to the ground state in ${}^{13}_{\Lambda}$C via the E1 transitions, the γ-rays are emitted much earlier than the stop. Thus energy corrections of the Doppler shift are necessary to sharpen peaks. How to perform the energy correction is summarized below.

1. Determine a position where a ${}^{13}_{\Lambda}$C emits a γ-ray from a reconstructed vertex of the (K^-, π^-) reaction for x, and y directions and from the segment number of LT for z direction.

2. Determine a position where the γ-ray interacts with a NaI crystal.

3. Calculate a direction the γ-ray is emitted from the positions.

4. Calculate a direction the ${}^{13}_{\Lambda}$C moving with β from a momentum transfer of the (K^-, π^-) reaction.

5. Correct a measured γ-ray energy by using the directions and β.

In the determination of the reaction position (1), a z vertex is difficult to precisely obtain at small scattering angles. Therefore, the z position is obtained from the segment number of LT with the maximal pulse height in which the ${}^{13}_{\Lambda}$C should decay. The center of the active target is obtained as the z position. It is to be verified below that this way is precise enough for the energy correction. In (2), the center of the NaI crystal is obtained as the x and z positions. The y position is a radiation length inner from the surface of the NaI crystal. The y position is not so serious for the energy correction. The direction of the emitted γ-ray can be calculated from these positions in (3). In (4), the momentum transfer is obtained from momentums and angles of a K^- beam and an outgoing π^-, and β is also obtained. The energy correction of the Doppler shift is performed (5) by using an opening angle (α) of the directions and β as

$$E'_\gamma = E_\gamma \times (1 - \beta cos\alpha). \tag{19}$$

Fig.40 shows distribution of (1-βcosα) used in the off-line analysis. Most of negative distribution is for NaI detectors installed above the target, while most of positive distribution is for NaI detectors installed below the target. RMS of distribution is 9.8 $\times$ 10^{-3} which corrects an energy of the 11 MeV γ-ray by about 110 keV. In our experiment, the energy correction of the Doppler shift is not serious because the NaI detectors were installed symmetrically in the vertical direction. Therefore, the effect of the Doppler shift is considered to contribute little to the splitting energy. It widens the peak width and decrease precision.

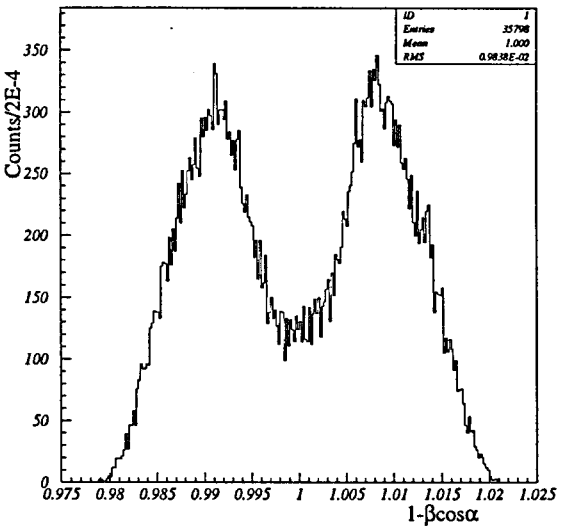

Figure 40: Distribution of (1-βcosα) used in the off-line analysis.

2.9 How to Add γ-ray Energies

When a high energy γ-ray enters a NaI crystal, it makes shower spreading in some crystals. To add γ-ray energies detected with some detectors is expected to make the full energy peak more dominant and to decrease the single escape peak in the γ-ray energy spectrum. In our experiment hypernucleus decays by emitting nucleons, thus on average there are a few clusters detected with detectors. It is necessary to add energies for all the clusters not to decrease the detection efficiency. How to add energies is summarized below.

1. Separate NaI detectors into clusters.
2. Find a detector with the maximal energy deposit in a cluster.
3. Count multiplicity in the cluster.
4. Add energies to the maximal energy in the cluster if the energies are 0.1$\sim$1.2 MeV.

If a detector has an energy deposit of more than 0.1 MeV, the detector is considered to be hit. Timing information from TDC is not used because energy thresholds of discriminators for TDC were set around 0.3 MeV. A timing information of the hit is not used because background is low enough, in addition the energy threshold of discriminators was set higher. A detector with an energy deposit of less than 0.1 MeV is not used in the analysis. In the clustering (1), there must be at least one detector without hit between

a cluster and another cluster. A cluster in the detectors installed above the target and a cluster in the detectors installed below the target are considered to be different. In (3), a cluster with multiplicity of more than 4 is not analyzed because a full energy peak is difficult to form by analyzing a cluster with many hits. It is shown in Fig.41 for the 8.999 MeV γ-rays, where an energy spectrum with multiplicity of 1 is compared with energy spectra obtained by adding energies. Data were collected in the ^{58}Ni(n, γ) calibration run under beam-off condition. Insufficient energy calibration performed by using only the ^{22}Na source is used, therefore energies are slightly shifted to the lower energy region. In adding energies (4), an upper energy threshold is also applied. Since detectors installed in the outer do not have good energy resolution, they are only used to add low energies to higher energy measured with detectors installed in the center. Therefore, if the outer detectors have an energy deposit of more than 1.2 MeV, the cluster is not used in the analysis. Fits to histograms are performed with the function of two gaussians added to the exponential. Measured mean energies of full energy peaks are 8.726 $\pm$ 0.007 MeV (a), 8.733 $\pm$ 0.006 MeV (b) and 8.744 $\pm$ 0.012 MeV (c). It is verified that the mean energy of the full energy peak is not shifted by adding γ-ray energies. It is found that the addition of γ-ray energies plays an important role in increasing yield of the full energy peak.

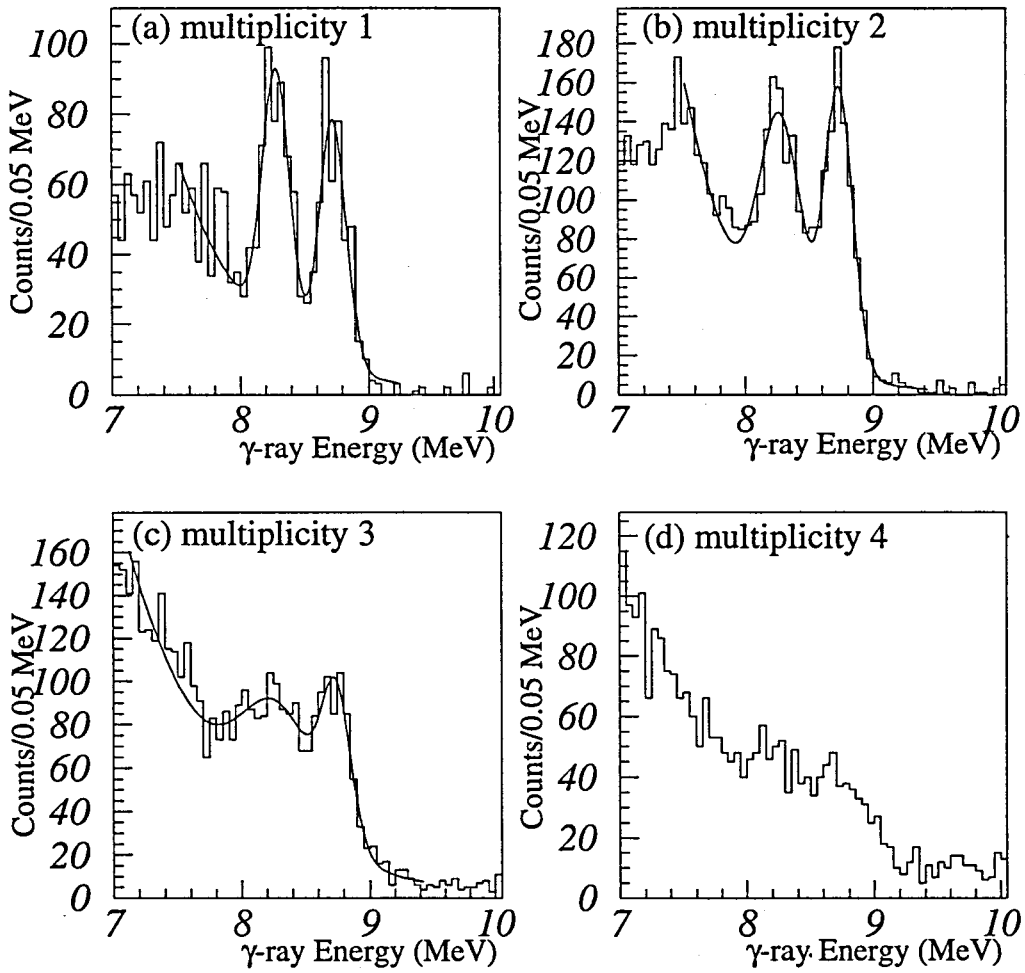

Figure 41: Typical energy spectra of the ^{58}Ni(n, γ) reaction with NaI multiplicities of 1 (a), 2 (b), 3 (c) and 4 (d) in a cluster.

2.10 Data Acquisition and Monitoring System

The data acquisition system had been developed based on the one used in the CERN NA36 experiment [47]. The experiment used four different modular electronics systems linked together to provide logic signal formation, digital logic circuitry and digital storage of analog and timing signals. The various electronic elements used are:

- NIM : Discrimination of analog signals to be used in the trigger logic and timing circuitry.
- FASTBUS : ADCs and TDCs.
- CAMAC : Fast readout TDCs and scalers. Input/Output registers. Computer control of electronics elements.
- VME : Main data acquisition processors that form raw event buffers, writes data to 8mm tape, passes data to other computers for on-line analysis and perform real time software calculations.

The kernel of the system was a pair of VME-based microprocessors (FIC1-2) from CES, one for the event readout and the other for the event building and output to an Exabyte 8mm tape drive. The latter also served for on-line monitoring. The device signals were processed mostly with FASTBUS ADCs and TDCs. Discriminated signals from the drift chambers, about 2200 channels in total, were digitized by LeCroy 1879 TDCs. Outouts from PMTs about 390 channels in total were divided into two; one fed into LeCroy 1885 ADCs for pulse height measurement and the other fed into Kinetic F432 high resolution TDCs (25 ps/channel) for timing measurement. For suppressing the data size, the pedestals of some ADC modules for NaI, VETO, DEC, LT and BT were subtracted, and the ADC data before subtraction were obtained in every 25th spills. The DAQ system also included several CAMAC modules to process scaler data and the trigger bits. Scaler information was read out spill-by-spill. The trigger status was stored in input resisters.

For on-line monitoring, a sample of data was transferred to the VMS computers (BNLH04 and BNLHY2) through a dual-ported Q-bus/VME.memory from BIT3. The data were also transferred from the host computer to other workstations linked through Ethernet. The on-line monitoring was made with a package called "IDA (interactive Data Analyzer)". The IDA had various processes running at a time. One of such processes was called "OPERATOR" to control the event analysis (start and stop the analysis, for example). A program called "HVIEW" displayed histograms defined by users. There were also programs such as "EVIEW" to display a view of each event and "NORMON" for monitoring of scaler information.

2.11 Off-line Data Analysis System

For off-line data analysis, the IDA programs were transplanted on the VMS system called RCNPAX at RCNP in Japan. The RCNPAX (OpenVMS V6.2-1H3) has four CPUs of 190 MHz clock (DEC chip 21064), and it also has five tape robots which enable users to save the experimental data with a size of more than 10 TBytes. Our data of $\sim$100 GBytes were small enogh to be saved in it. In the first stage complicated analyses of the tracking using chambers and the reconstruction of momentum and mass were performed on the RCNPAX. The data reduction by selecting events with measured γ-ray energy of more than 1 MeV was also performed on it.
In the second stage the data analyses of NaI detectors, active targets and other detectors around the target were performed on the UNIX system called MIHO, MIHO2 at RCNP. The MIHO (Digital UNIX) and MIHO2 have 24 CPUs of 440 MHz (DEC chip EV56), which provides users with a fine environment of the data analysis.

3 Data Analysis

In this section, the procedures of data analyses are described. The $^{13}C(K^-, \pi^-)$ data were collected for about 40 days in 1998. Typical intensity of the primary protons delivered to the production target of D-line was 5×10^{12}/spill. Typical K^- beam intensity was 5×10^4 on the target, and accumulated number of K^-s was 2.1×10^{10}.

For about 10 days in the beginning of the experiment, gains of NaI detectors had been unstable due to high counting rates. After decreasing voltages for PMTs, they became stable. Consequently, the data collected stably with 1.4×10^{10} K^-s were analyzed.

3.1 Data Reduction

Since total data size was ~100 Gbytes which was not small enough to handle easily, the data reduction was necessary for efficient analyses. Basically events without γ-ray hits on NaI detectors were not needed, therefore it was one of the best ways to select events with γ-ray hits. By selecting events with the energy deposit of more than 1 MeV on the 32 NaI detectors with high energy resolution installed in the center, the data size decreased to 7.1 Gbytes.

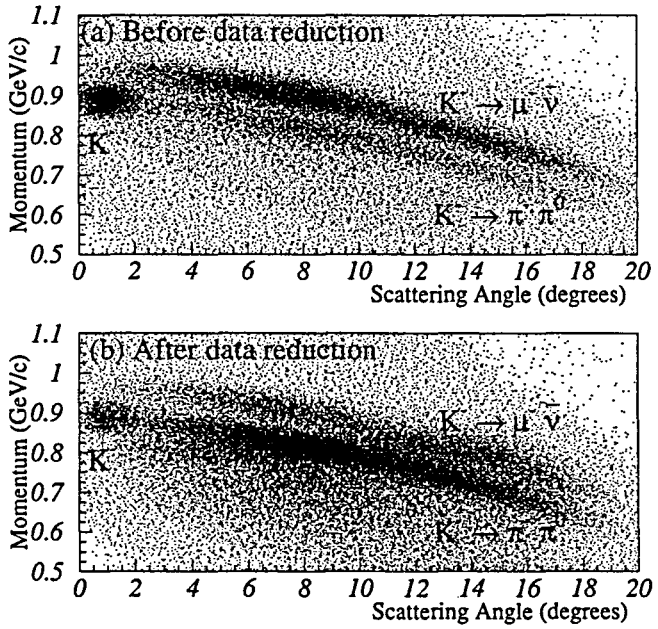

Figure 42: 2-dimensional plots of the scattering angle versus the momentum before the data reduction (a) and after the data reduction (b).

Fig.42 shows 2-dimensional plots of the scattering angle versus the momentum of the

outgoing particle, where in the upper spectrum about 10 % of the all data before the reduction are plotted, while in the lower spectrum data after the reduction are plotted. The data reduction decreases the $K^- \rightarrow \mu^- + \bar{\nu}_\mu$ decay which is the most dominant background. But the $K^- \rightarrow \pi^- + \pi^0$ decay is not so much decreased because π^0 decays to two γ-rays. The beam event is also decreased by the data reduction. Detection efficiency of the 32 NaI detectors for the 11 MeV γ-ray is estimated to be 22.3 % by the Monte Carlo simulation, GEANT.

3.2 Event Selection

The $^{13}C(K^-, \pi^-)$ reaction events should be purified by rejecting background events such as events originating from other materials than the target and events of particle misidentification. The quantities used for the event selection are beam line TOF, reconstructed mass of the outgoing particle, position of the reaction vertex, pulse heights of DEC and LT, timing signal of VETO and pulse height of NaI detector.

3.2.1 Beam line TOF

Distribution of ΔTOF between MT and IT is shown in Fig.43, where the TOF of K^- beam is adjusted to zero. The π^- beam is not observed because it was rejected by the hardware selection of the KPI trigger using the Čerenkov counters of IC and BQC. Most of the continuous background is coming from the multi-hits and the in-flight decay of K^- in the beam line. The criterion to select the (K^-, π^-) events is set to :

$$|\Delta TOF| \leq 2.0 \text{ nsec}, \tag{20}$$

as indicated by arrows in the figure.

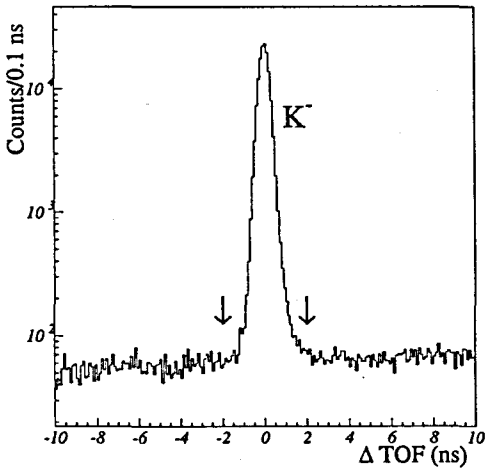

Figure 43: TOF difference between MT and IT. Arrows indicates the criteria for selecting the (K^-, π^-) events.

3.2.2 Mass of Outgoing Particles

Reconstructed mass distribution of outgoing particles is shown in Fig.44. The outgoing π^- is clearly separated from K^-. μ^- originating from the in-flight decay of K^- is not separated from the π^- because of the small mass difference between 0.106 and 0.140 GeV/c^2. Events collected with the KPI trigger include the contamination of K^- beam events, which is caused by δ-rays effecting the performance of FAC. Although the mass separation looks pretty good judging from the figure, the efficiency of the reconstruction is found to be poor (~70 %). The reason of the poor efficiency is low gains of PMTs of BT. When a particle hit on a BT element near a PMT, the gain of the PMT was high, but that of the other PMT was not high enough to be discriminated because of the attenuation. Consequently, for maintaining high analysis efficiency, we decide to apply a loose event selection which rejects only K^-. Not so large amount of background in the energy spectrum of γ-rays at around 11 MeV supports the selection. The criterion to select the (K^-, π^-) events is set to :

$$Mass \leq 0.45 \text{ GeV/c}^2,\ 0.54 \text{ GeV/c}^2 \leq Mass, \tag{21}$$

as indicated by arrows in the figure. Thresholds for the event selection are set at 3σ above and below the mean of the K^- peak. When the reconstruction of the mass is failed, the event has the negative mass.

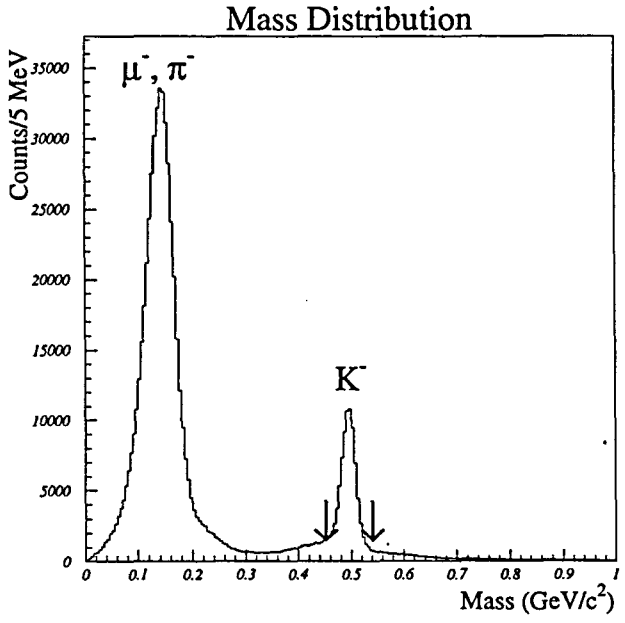

Figure 44: Reconstructed mass spectrum of outgoing particles. π^- and μ^- at around 0.15 GeV/c^2 are clearly separated from K^-.

3.2.3 Reaction Vertices

The event selection using the reaction vertices is not so essential for purifying the $^{13}C(K^-, \pi^-)$ reaction because the signal of the LT1 was used to form the hardware KPI trigger. However the reconstructed vertices play an important role in correcting γ-ray energies affected by the Doppler shift. Therefor, relatively loose event selections by using the reaction vertices are performed, which rejects events with strange reaction vertices.

Fig.45 shows distribution of the reaction vertex in the z direction reconstructed from hits on the drift chambers upstream and downstream the target (ID1-2 and FD1-2). The width of the distribution (13.5 cm FWHM) is almost consistent with the size of the target in the z direction. Since the spectrum has tails in the both sides, it is not easy to put thresholds. The tails originate from the difficulty in reconstructing the reaction vertex in the z direction for the events with π^-s scattered at small angles. On the other hand, the reaction vertex for the events with π^-w scattered at larger angles can be precisely reconstructed. It is afraid that the event selection by the reaction vertex in the z direction may lead to poor detection efficiency of the (K^-, π^-) reaction at the small scattering angles. Consequently, the event selection using the reaction vertex in the z direction is not performed. It is better to extract the reaction vertex in the z direction from the information on pulse heights of LT which can provide the resolution of better than 1.5 cm.

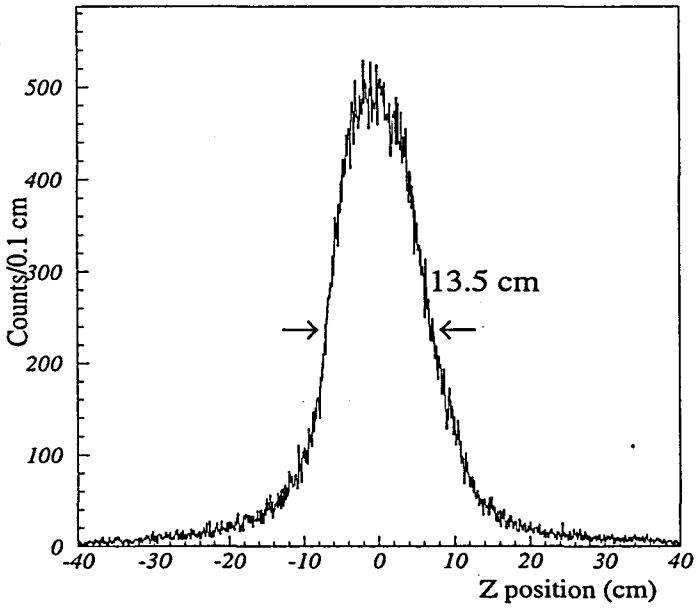

Figure 45: Distribution of the reaction vertex in the z direction at the scattering angles of 0 to 16 degrees. The width of 13.5 cm FWHM is almost consistent with the size of the target in the z direction.

Distributions of the reaction vertices in the x and y directions are shown in Fig.46. Widths (FWHM) of the distributions are 4.4 cm and 0.9 cm for the X and Y directions respectively. The widths are smaller than the target sizes of 6.0 cm (X) and 1.5 cm (Y). For rejecting events with strange reaction vertices, we loosely require :

$$-6.0 \text{ cm} \leq X_{vertex} \leq 6.0 \text{ cm}, -3.0 \text{ cm} \leq Y_{vertex} \leq 3.0 \text{ cm}, \tag{22}$$

which exclude about 0.7 % of the events.

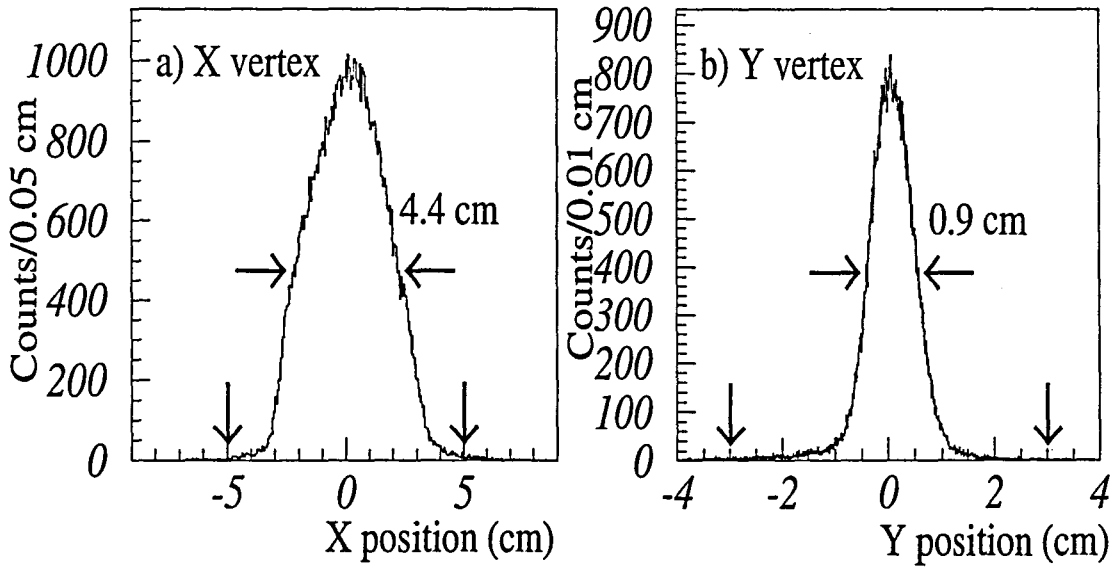

Figure 46: Distributions of the reaction vertices in the x (a) and y (b) directions at the scattering angles of 0 to 16 degrees. Down arrows indicate thresholds for rejecting events with strange reaction vertices.

3.2.4 DEC

DEC which has four segmentations was installed for the detection of the weak decay particles from the target. Fig.47 shows typical energy spectra of DEC collected with the KPI trigger (a) and with the ^{22}Na trigger for the energy calibration of NaI detectors (b), where pedestals are subtracted. Since there are not any structures with the exception of the continuum in (a), the energy calibration of DEC is performed using compton edges observed in (b). The compton edges observed at 200 and 600 channels correspond to γ-rays with the energies of 0.511 MeV emitted by annihilation and 1.275 MeV from ^{22}Ne respectively. When a charged particle emitted by $^{13}_{\Lambda}$C passes through DEC, relatively high energy is detected. Accordingly, the weak decay events can be discriminated by selecting events with high pulse heights. As an energy threshold for the selection increases, an amount of background mainly from the in-flight decay of K^- decreases. The amount of background suddenly decreases at the energy threshold of 2 times higher than the compton edge of the 1.275 MeV γ-ray. Consequently, the energy threshold which is indicated by arrows in the figures is set at 2.5 times higher than the compton edge.

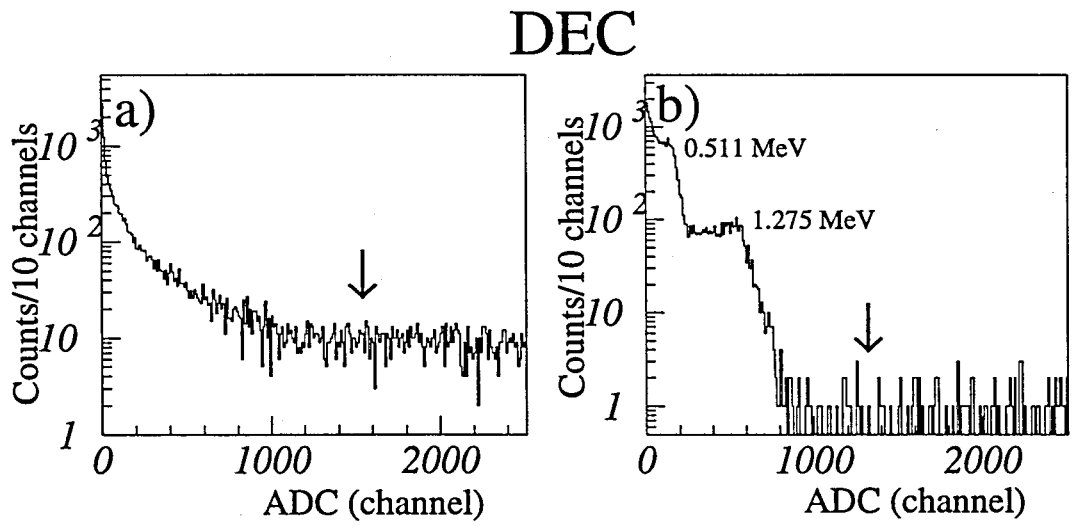

Figure 47: ADC spectra of DEC collected with KPI trigger (a) and with ^{22}Na trigger (b). Observed compton edges correspond to γ-rays with energy of 0.511 MeV and 1.275 MeV. Arrows indicate the threshold energy for selecting the weak decay of $^{13}_{\Lambda}$C.

Events selected with DEC are shown in Fig.48, where the horizontal axis represents the scattering angle and the vertical axis represents the momentum measured using the spectrometer. Most of the residual backgrounds in Fig.42(b) look disappeared, and a new locus corresponding to the formation of ${}^{13}_{\Lambda}\mathrm{C}$ hypernucleus is clearly observed. The locus is almost independent of the scattering angle due to the large mass of ${}^{13}\mathrm{C}$. It is shown that DEC has enough ability to detect the weak decay of ${}^{13}_{\Lambda}\mathrm{C}$ and to reject background mainly due to the in-flight decays. The detection efficiency and the inefficiency of DEC are to be described below.

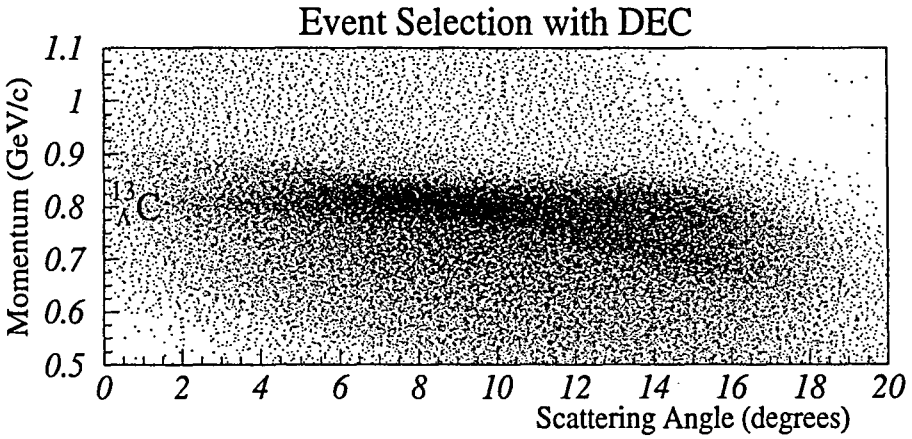

Figure 48: 2-dimensional plot of the scattering angle versus the momentum. Events are selected with DEC.

3.2.5 LT

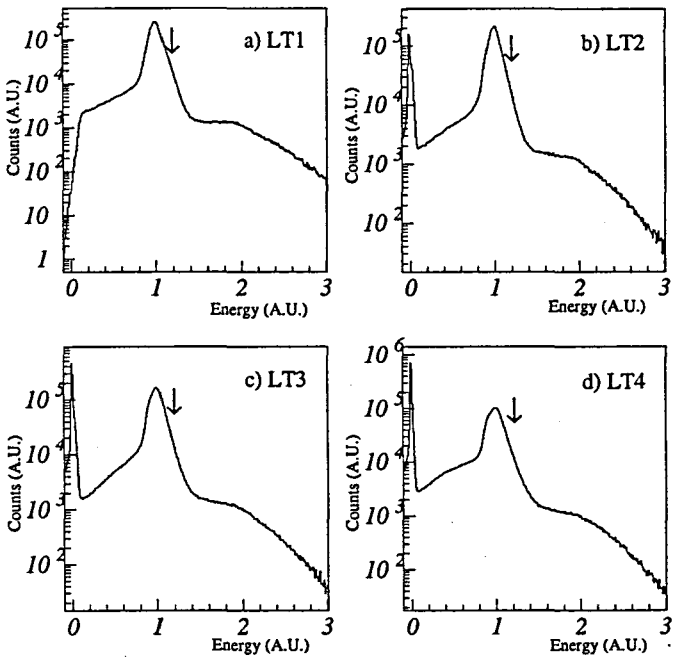

Figure 49: Energy spectra of LT at the scattering angles of 0 to 16 degrees, a) the first, b) the second, c) the third and d) the last segments. The mean of the minimum ionization peak is normalized to unity. Arrows indicate the energy threshold which is set at 3σ above the mean of the minimum ionization peak.

LT is a useful device to detect the weak decay of ${}^{13}_{\Lambda}\mathrm{C}$ and to reject the in-flight decay of K^-. Especially, the $K^- \rightarrow \pi^- + \pi^0$ decay that produces two γ-rays is one of the most dominant backgrounds in the experiment. Fig.49 shows energy spectra of four segments of LT for the (K^-, π^-) reaction at the scattering angles of 0 to 16 degrees. Horizontal axis represents an average pulse height of left and right PMTs', where the mean of the minimum ionization peak is normalized to unity. Since a signal of LT1 was used to form the trigger, the pedestal of LT1 is not observed. Typical energy resolutions (σ) of the minimum ionization peaks are 6.2 % (LT1), 6.5 % (LT2), 6.6 % (LT3) and 7.1 % (LT4). A resolution of the latter segment is worse than that of the former segment. The differences suggest that a particle scattered at large angle deposits more energy in the latter segments. It is also possible for the particle to easily escape LT without passing through the latter segment. These ambiguities are considered to widen peaks. Arrows indicate the energy threshold which is set at 3σ higher than the mean of the minimum ionization peak. Statistically, a probability that a pulse height of the in-flight decay exceeds the threshold is 0.13 % for a segment. The probability for all segments

is estimated to be 0.5 %. Therefore, it is expected that the 3σ threshold suppresses the in-flight decays less than 1 %.

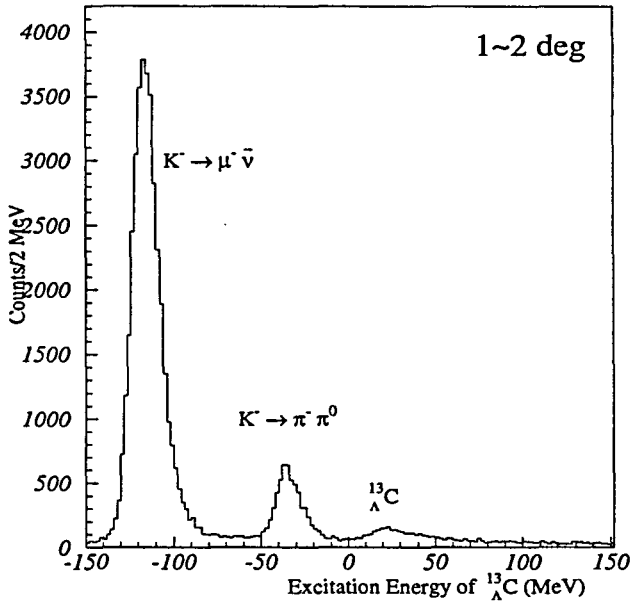

Figure 50: Energy spectrum of $^{13}_{\Lambda}C$ at the scattering angles of 1 to 2 degrees before the data reduction.

An energy spectrum of $^{13}_{\Lambda}C$ at the scattering angles of 1 to 2 degrees before the data reduction is shown in Fig.50. At these angles the $^{13}C(K^-, \pi^-)$ events are clearly separated from the in-flight decay events. Therefore, it enables to extract detection efficiencies for the weak decay of $^{13}_{\Lambda}C$ by counting the number of events at different conditions of the energy threshold of LT. Ratio of the numbers between the $\mu\nu$ and $\pi\pi$ decays is about 7:1, which differs from the expected ratio of 3:1. It is estimated that the angular distributions of the decays cause the difference. Estimated energy resolution is about 13 MeV which is worse than those obtained using other magnetic spectrometers, for example 2 MeV obtained using SKS at KEK, 2 MeV using SPES II at CERN and 3 MeV using Moby-Dick at BNL. However, it is not so serious in our experiment by virtue of much better energy resolution of the NaI detector.

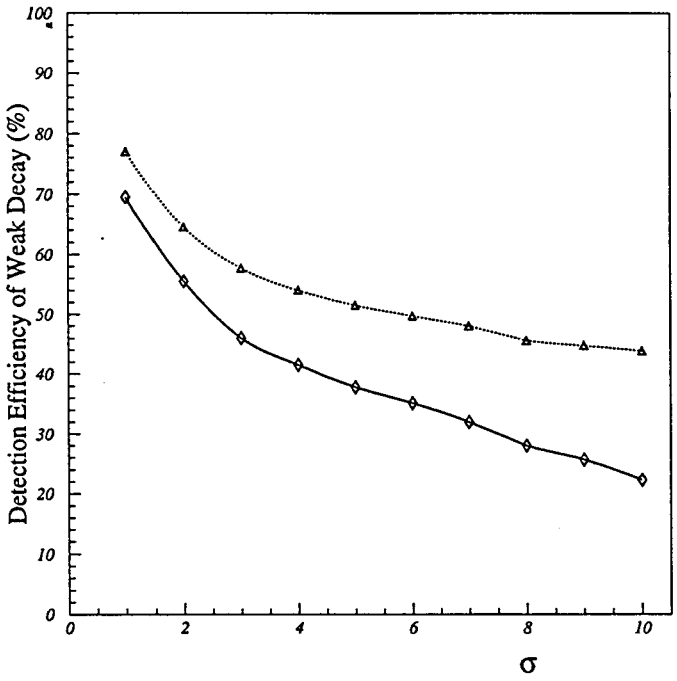

Figure 51: Detection efficiencies for the weak decay of ${}^{13}_{\Lambda}$C. Solid line represents the efficiency of LT, and dotted line represents that of both LT and DEC.

Detection efficiencies measured for the weak decay of ${}^{13}_{\Lambda}$C at the (K^-, π^-) scattering angles of 1 to 2 degrees are shown in Fig.51, where the efficiency of LT and that of both LT and DEC are plotted. The number of events in the excitation energy region of 0 to 20 MeV is counted to measure the efficiency at different conditions of active target's threshold. As the energy threshold changes from 1σ to 10σ above the mean of the minimum ionization peak, the efficiency of LT decreases from 70 % to 22 %. While the efficiency of both LT and DEC decreases from 77 % to 44 %. The efficiency using only LT is almost same as that measured by the test experiment using liquid scintillator of normal benzene in 1997. It is verified that DEC detects decay particles which are not detected by LT, and it provides additional efficiency.

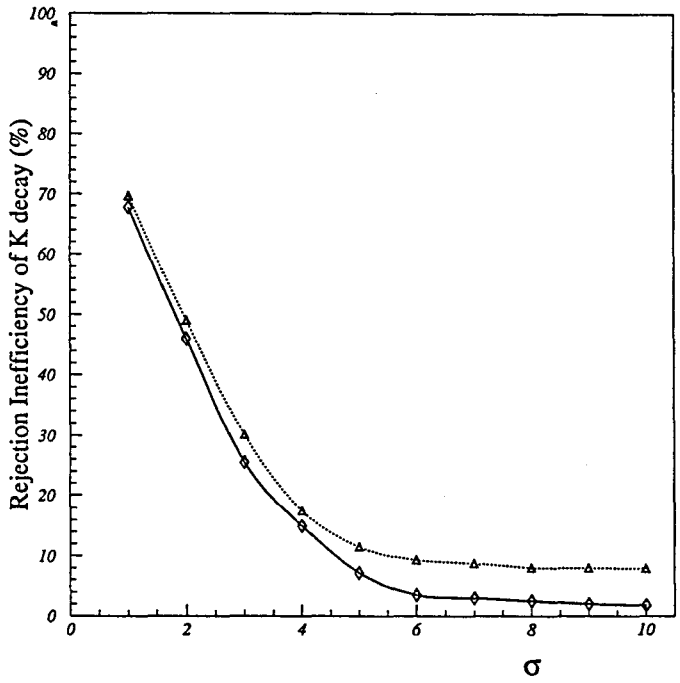

Figure 52: Inefficiency for the rejection of the in-flight decay of K^- at different conditions of the energy threshold of LT. Solid line represents the inefficiency of LT, and dotted line represents that of both LT and DEC.

Inefficiencies for the rejection of the in-flight decay of K^- at the (K^-, π^-) scattering angles of 1 to 2 degrees are also plotted in Fig.52, where the inefficiency of LT and that of both LT and DEC are plotted. The number of events in the excitation energy region of -130 to -90 MeV are counted to measure the inefficiencies. The measured inefficiency is larger than that expected statistically, which is due to the multi-hits on LT. A probability that two particles hit LT simultaneously is estimated to be $\sim$1 % by considering the beam intensity of 7 $\times$ 10^4 particles/spill and the ADC gate width of 150 ns. As the energy threshold changes from 1σ to 10σ above the mean of the minimum ionization peak, the inefficiency using LT decreases from 68 % to 1 %. While the inefficiency using LT and DEC decreases from 70 % to 8 %. The inefficiency of DEC is about 7 % that occupies most part of those at the thresholds of more than 6σ. However it is not so serious at the thresholds of less than 5σ. Consequently, the threshold of LT is set at 3σ above the mean of the minimum ionization peak. Although inefficiency for the rejection of the in-flight decay is not small enough, the increased detection efficiency of the weak decay of ${}^{13}_{\Lambda}$C provides the minimal statistical errors for the spin-orbit splitting of ${}^{13}_{\Lambda}$C.

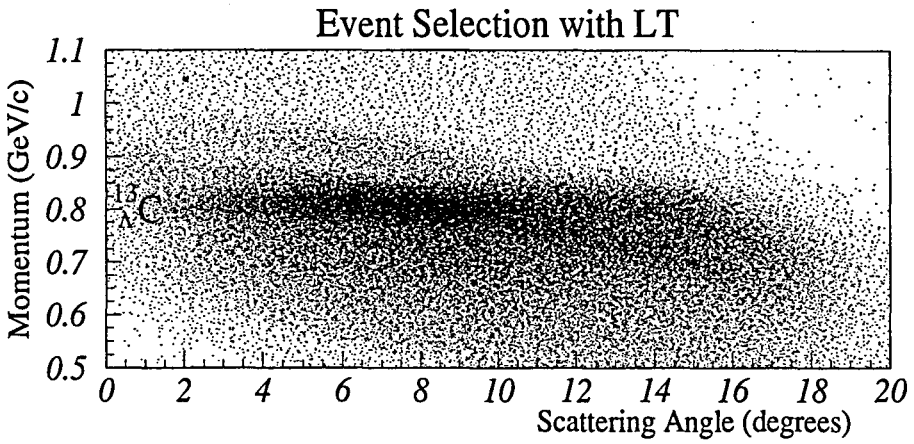

Figure 53: 2-dimensional plot of the scattering angle versus the momentum. Events are selected with LT. The threshold of LT is set at 3σ above the mean of the minimum ionization peak.

Events selected with LT at the threshold of 3σ above the mean of the minimum ionization peak are shown in Fig.53, where the horizontal axis represents the scattering angle and the vertical axis represents the momentum measured using the spectrometer. In spite of the loose event selection, most of the residual backgrounds in Fig.42(b) look disappeared, and a locus corresponding to the formation of $^{13}_{\Lambda}$C hypernucleus is clearly observed. An amount of background seems a little bit larger than that selected with DEC shown in Fig.48. LT has enough ability to detect the weak decay of $^{13}_{\Lambda}$C and to reject background mainly due to the in-flight decays.

3.2.6 VETO

VETO covering all NaI detectors is used to reject charged particles emitted from the target. Typical ADC and TDC spectra are shown in Fig.54, where the pedestal is subtracted in the ADC spectrum (a). Since there are not any peak structures such as a minimum ionization peak of charged particles in the ADC spectrum (a), only the TDC information is used to judge whether a charged particle hits VETO or not. The particle hit requires both TDC signals of the left and right PMTs in the range of 1000 channels (25 ns) in the TDC spectrum.

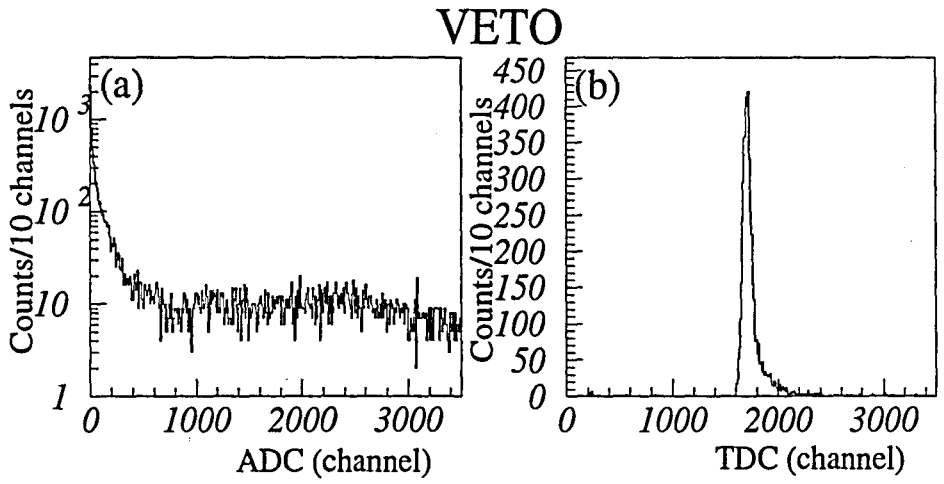

Figure 54: Typical ADC (a) and TDC (b) spectra.

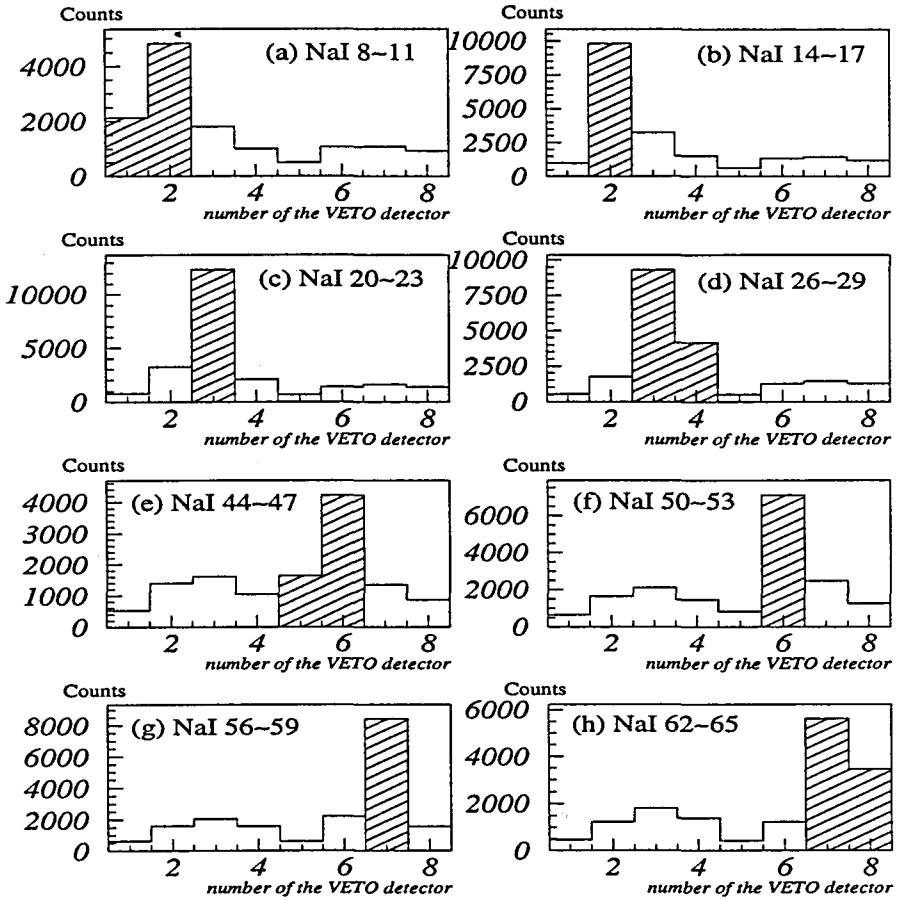

Figure 55: Hit patterns of VETO. (a), (b), (c), (d), (e), (f), (g) and (h) represent the hit pattern when the maximal energy deposit in all NaI detectors is on #8~ #11, #14~ #17, #20~ #23, #26~ #29, #44~ #47, #50~ #53, #56~ #59 and #62~ #65 respectively. Hatch indicates areas geometrically expected from the arrangement shown in Fig.31 when a charged particle goes through the detectors.

Fig.55 shows hit patterns of VETO. (a), (b), (c), (d), (e), (f), (g) and (h) represent the hit patterns when the maximal energy deposit in all NaI detectors is on #8~ #11, #14~ #17, #20~ #23, #26~ #29, #44~ #47, #50~ #53, #56~ #59 and #62~ #65 respectively. The events that the outer detectors have the maximal energy deposit were already removed by the data reduction described above. Hatch indicates areas geometrically expected from the arrangement shown in Fig.31 when a charged particle goes through the detectors. An event with energy deposits both on a NaI detector and on a VETO detector which covers the NaI detector should be rejected even if it is cause by a γ-ray. The selection applied for VETO is summarized in Table.7.

Probabilities of particles hitting each VETO are measured to be 2.6 % (VETO1), 9.3

% (VETO2), 12.6 % (VETO3), 6.4 % (VETO4), 2.5 % (VETO5), 7.4 % (VETO6), 9.1 % (VETO7) and 5.3 % (VETO8) for the data after the reduction. The counting rate of VETO installed near the target is higher and that installed downstream is also higher. If one of the VETO1, VETO4, VETO5 and VETO8 has a hit, the detection efficiency for γ-rays is estimated to decrease by factor of 0.893 from the simulation considering the solid angles, while in the case of VETO2, VETO3, VETO6 and VETO7, the efficiency decreases by factor of 0.750. As a result the detection efficiency of the γ-ray is estimated to decrease by factor of 0.90 when the event selection with VETO is applied.

♯ of the center NaI detector with the maximal energy deposit	Selection
8∼11	no hit on VETO1 and VETO2
14∼17	no hit on VETO2
20∼23	no hit on VETO3
26∼29	no hit on VETO3 and VETO4
44∼47	no hit on VETO5 and VETO6
50∼53	no hit on VETO6
56∼59	no hit on VETO7
62∼65	no hit on VETO7 and VETO8

Table 7: Applied selection for VETO.

3.2.7 NaI Detectors

We used 72 NaI detectors with various energy resolutions in the experiment as shown in Fig.39. Although detectors installed in the center have good energy resolution, detectors installed in the outer have about 1.5 times worse energy resolution. Precision of a peak center is roughly determined by $\Delta E/\sqrt{N}$, where ΔE indicates the energy resolution and N indicates the number of events in the peak. Thus, the worse energy resolution needs approximately 2.25 times higher statistics in compensating itself. Consequently, we decide to obtain energy spectra of γ-rays with mainly 12 NaI detectors with high energy resolution, and other detectors are used to add γ-ray energies. Because it must give obvious results even if precision is a little bit worse than that obtained with all the NaI detectors. The 12 NaI detectors were installed in the center above the target (♯9, ♯10, ♯15, ♯16, ♯21 and ♯22) and below the target (♯45, ♯51, ♯52, ♯57, ♯58 and ♯64).

A detection efficiency of the 12 NaI detectors for the 11 MeV γ-ray is estimated by using the Monte Carlo simulation, GEANT. NaI detectors are placed in the same positions as those in the experiment. γ-rays are emitted without the Doppler shift from the target with same size. Each γ-ray energy measured with a detector has width of $\Delta E = 220 \times \sqrt{E(keV)/4439}$ keV FWHM which is the same energy resolution as the experiment's. The γ-ray energies are added in the same way as that in the off-line data analysis. Obtained energy spectrum is shown in Fig.56. By virtue of the high energy resolution, a single escape peak looks separated from a full energy peak. Strength of the single escape peak is ~50 % of that of the full energy peak. The detection efficiency obtained by counting the number of events in the region of 10.3 to 11.5 MeV is 5.0 %. The energy spectrum is fitted using the function of

$$\begin{aligned} F(E_\gamma) &= p1 \cdot e^{-\left(\frac{E_\gamma - p2}{\sqrt{2}\cdot p3}\right)^2} + p4 \cdot e^{-\left(\frac{E_\gamma - p5}{\sqrt{2}\cdot p6}\right)^2} \\ &\quad + p7 \cdot e^{-(11.45 - E_\gamma)} \cdot \left(p8 \cdot (11.45 - E_\gamma) + (p9 \cdot (11.45 - E_\gamma))^2\right). \end{aligned} \tag{23}$$

Used parameters of p1 to p9 are written in Fig.56. This function is used to fit histograms of the γ-ray energy spectra.

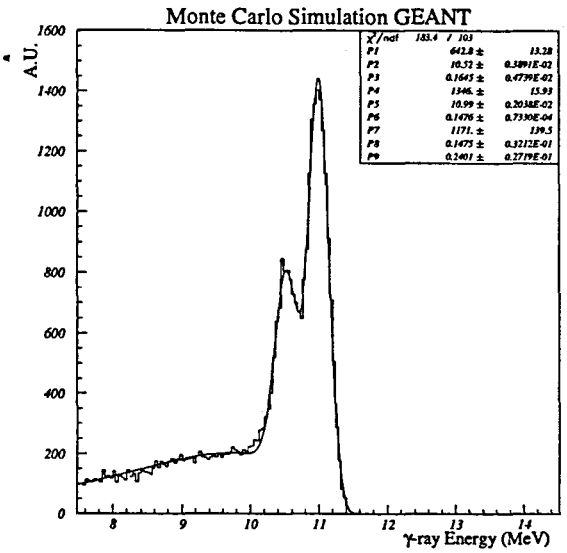

Figure 56: Energy spectrum of the 11 MeV γ-rays obtained by the Monte Carlo simulation, GEANT.

3.2.8 Energy Spectrum of $^{13}_{\Lambda}$C

An energy spectrum of $^{13}_{\Lambda}$C by the (K^-, π^-) reaction at 0 to 16 degrees is shown in Fig.57. The efficiency of the track reconstruction is 89 % that is much better than that expected before the experiment. The energy resolution of the spectrometer is estimated to be about 13 MeV FWHM from the momentum resolution of the in-flight decay of K^-. There are not any peak structures because of the poor energy resolution. In addition, the in-flight decay, which is not sufficiently rejected by the loose event selections using DEC and LT, spreading wide regions in the energy spectrum is also a dominant reason. The excitation energy is corrected by adjusting the measured momentum to the one expected from the kinematics of the in-flight decay of K^-. The correction of the momentum loss in the thick target needs much better reaction vertex resolution. Because of poor resolution, we could not perform the correction. For the event selection of the ~11 MeV states in $^{13}_{\Lambda}$C we require

$$-9 \text{ MeV} \leq \text{Ex} \leq 15 \text{ MeV}, \quad 0° \text{ to } 7°, \tag{24}$$

$$-9 \text{ MeV} \leq \text{Ex} \leq 18 \text{ MeV}, \quad 7° \text{ to } 10°, \tag{25}$$

$$-12 \text{ MeV} \leq \text{Ex} \leq 18 \text{ MeV}, \quad 10° \text{ to } 16°. \tag{26}$$

24~30 MeV windows are considered to be reasonable by considering the energy resolution of 13 MeV FWHM. Window sizes are adjusted for each scattering angles of the (K^-, π^-) reaction.

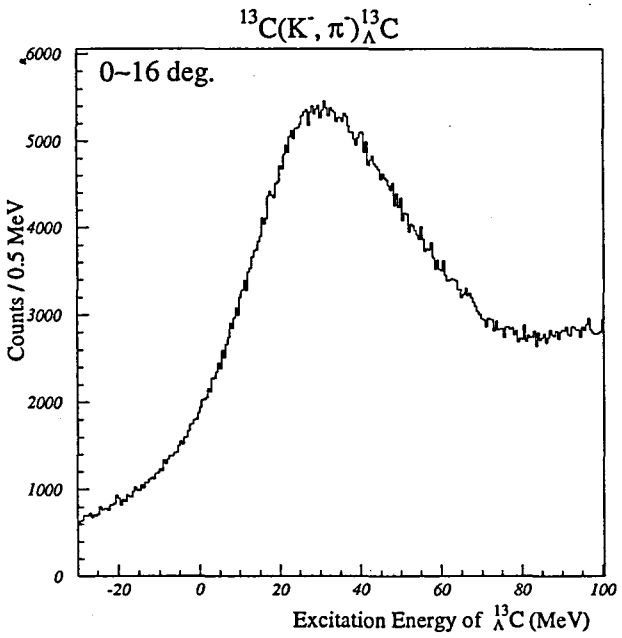

Figure 57: Energy spectrum of $^{13}_{\Lambda}$C at the scattering angles of 0 to 16 degrees.

The event selection criteria of the Λ bound region in $^{13}_{\Lambda}$C is defined as

$$-15 \text{ MeV} \leq \text{Ex} \leq 20 \text{ MeV}, \tag{27}$$

while that of the quasi-free region of ^{13}C(K^-, π^-) reaction is also defined as

$$30 \text{ MeV} \leq \text{Ex} \leq 100 \text{ MeV}. \tag{28}$$

3.2.9 Analysis Efficiency and Detection Efficiency for the 11 MeV γ-ray

Efficiency throughout the data taking to the off-line analyses are summarized in Table.8. The average live time of the DAQ system was 0.78, which is almost the same as expected one.

Data taking	DAQ live time	0.78
On-line trigger	K^- detection efficiency of IC and BQC	0.99
	π^- detection efficiency of FAC	0.91
	weak decay selection with DEC and LT	0.57
	track reconstruction	0.89
Total		**0.36**

Table 8: Efficiency throughout the data taking to the off-line analyses.

As for the detection efficiency for the 11 MeV γ-ray, it becomes 0.22 after the data reduction by selecting events with the maximal energy deposit on 32 NaI detectors installed in the center. Furthermore, we restrict the selection, therefore the detection efficiency becomes 0.050 by selecting events with the maximal energy deposit on 12 NaI detectors with better energy resolution. Consequently, the detection efficiency becomes 0.045 by applying VETO for rejecting events with charged particles.

4 Experimental Result and Discussion

4.1 Quasi-free Region of $^{13}C(K^-, \pi^-)$ Reaction

4.1.1 γ-ray Energy Spectrum Around 4.4 MeV

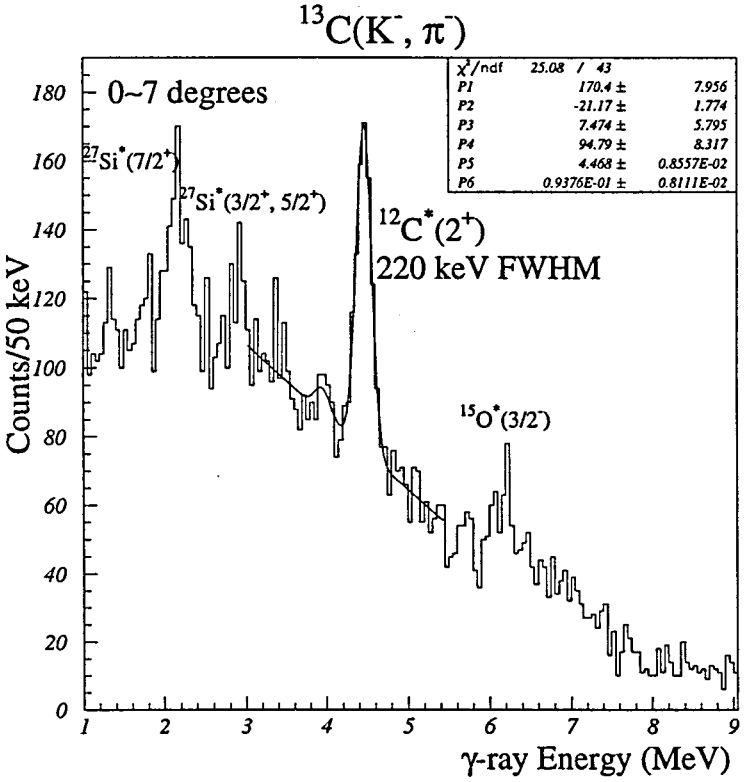

Figure 58: Energy spectrum of γ-rays detected mainly with the 11 NaI detectors installed in the center. The quasi-free region is selected in the energy spectrum of $^{13}_{\Lambda}C$ at the scattering angles of 0° to 7°.

One of the most suitable ways to confirm validity of our experiment and data analysis is to observe well known γ-rays emitted by nuclei such as ^{12}C, ^{27}Si or ^{15}O. Especially, ^{12}C is frequently produced by the quasi-free $^{13}C(K^-, \pi^- \Lambda)^{12}C$ process because of the large amount of ^{13}C used as the target. Two γ-rays are dominantly observed from excited states in ^{12}C, one is the 4.439 MeV γ-ray and the other is the 15.110 MeV γ-ray. Fig.58 shows an energy spectrum of γ-rays mainly detected with the 12 NaI detectors installed in the center. The quasi-free region defined above is selected in the energy spectrum of $^{13}_{\Lambda}C$ at the scattering angles of 0° to 7°. The most dominant γ-ray is from the first excited 2^+ state at 4.439 MeV to the ground state in ^{12}C via the E2 transition in the half-life of 42 fs. A fit to the histogram is performed with the function of two gaussians added to the linear function in the region of 3.0 to 5.4 MeV. A mean energy of the lower gaussian is fixed at 0.511 MeV lower than that of the higher one because the lower gaussian is for a single escape peak. As a result of the fit, the mean energy of the full energy peak is obtained as 4.468 $\pm$ 0.009 MeV, and the energy resolution is 220 $\pm$ 19 keV FWHM. The

measured mean energy of the full energy peak is a little bit higher than the correct energy of 4.439 MeV. The shape of background around 4.4 MeV and a recoil of the ^{12}C nucleus by the quasi-free scattering are considered to mainly cause the energy shift. If the enegy shift is caused by the energy calibration of NaI detectors, it would contribute little to the final result. The observed good energy resolution which is almost the same as that we planned to achieve before the experiment shows that our experiment was performed in good conditions and the data analysis was completed correctly. The energy resolution for the 11 MeV γ-ray is estimated to be 350 keV FWHM by assuming that the energy resolution gets wider according to $\sqrt{E_\gamma}$ as shown in Fig.38.

There are other peak structures in Fig.58. Peak structures at 6.2 MeV and at 5.7 MeV are considered to correspond to the full energy and single escape peaks of the γ-ray emitted by the $3/2^-$ state at 6.176 MeV in ^{15}O. A peak at 2.2 MeV looks much wider than the expected energy resolution of 160 keV FWHM. It is natural to think that the peak is composed of more than two peaks located closely. One of peaks is considered to be the γ-ray emitted by the $7/2^+$ state at 2.164 MeV in ^{27}Si. A peak structure observed at 2.9 MeV is identified to be the γ-ray from the $3/2^+$ or $5/2^+$ state at 2.866 MeV to the ground state in ^{27}Si. The ^{16}O and ^{28}Si nuclei are the most dominant compositions of the target cell made of quartz with total thickness of 8 mm.

4.1.2 γ-ray Energy Spectrum Around 15 MeV

The 15.110 MeV γ-ray is emitted by the 1^+ state (T=1) to the ground state in ^{12}C via the M1 transition in the half-life of 11 as. A γ-ray peak is clearly observed at 15 MeV as shown in Fig.59, where the quasi-free region in the energy spectrum of $^{13}_{\Lambda}$C at the scattering angles of 0° to 16° is selected. Although the expected energy resolution for the 15.110 MeV γ-ray is 410 keV FWHM, the observed peak looks wider. One of reasons is that the energy resolution of 410 keV FWHM does not easily separate a single escape peak from a full energy peak. In addition, height of the single escape peak is estimated to be ~60 % of that of the full energy peak by using the Monte Carlo simulation GEANT, which makes it more difficult. Therefore, it is reasonable that the observed width of the peak looks wider.

There is another structure at 11 MeV. The structure is estimated to correspond to the γ-ray emitted by the $^{13}_{\Lambda}$C hypernucleus. The insufficient energy resolution in the energy spectrum of $^{13}_{\Lambda}$C produces background in the quasi-free region. It is known that the 1^+ state at 15.110 MeV also decays to the first excited 2^+ state by emitting the 10.671 MeV γ-ray. The branching ratio of the decay is much smaller than that to the ground state, therefore the γ-ray contributes little to the spectrum. The background γ-ray is considered to originate from the decay of π^0. π^0 is dominantly produced by the in-flight decay of K^- and also produced by the mesonic decay of Λ. It is expected that the amount of background in the bound region is less than that in the quasi-free region.

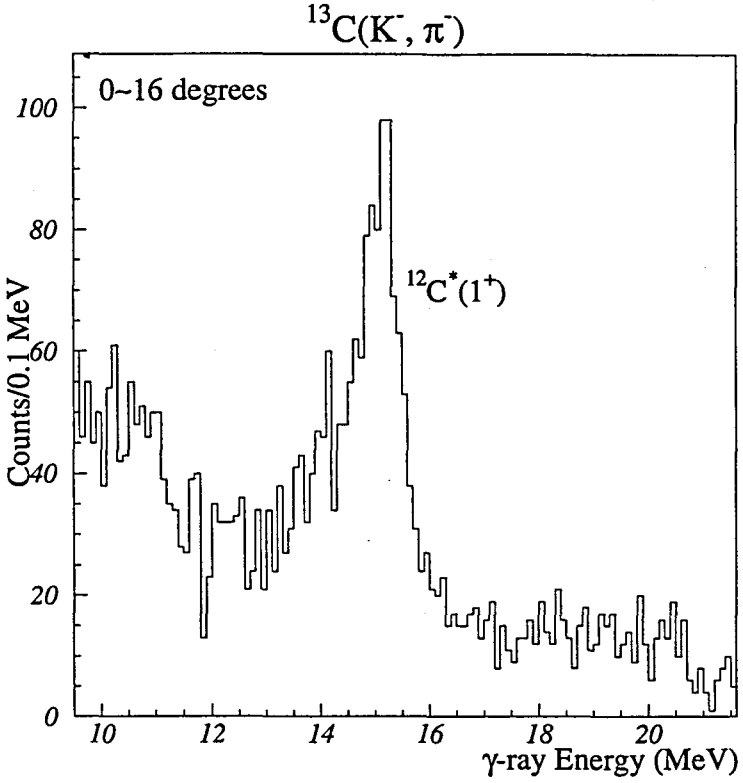

Figure 59: Energy spectrum of γ-rays detected mainly with the 12 NaI detectors installed in the center. The quasi-free region in the energy spectrum of $^{13}_{\Lambda}C$ at the scattering angles of 0° to 16° is selected.

4.2 Bound Region of $^{13}C(K^-, \pi^-)$ Reaction

4.2.1 γ-ray Energy Spectrum Around 4.9 MeV

In the bound region a peak at 4.9 MeV corresponding to the γ-ray from the $3/2^+$ second excited state to the ground state in $^{13}_{\Lambda}C$ via the E2 transition is observed as shown in Fig.60, where the energy correction of the Doppler shift is performed. A peak at 4.4 MeV which corresponds to the γ-ray emitted by ^{12}C observed in the quasi-free region is still observed as background because of insufficient energy resolution in the energy spectrum of $^{13}_{\Lambda}C$. The 4.439 MeV γ-ray is emitted after the Λ decay of $^{13}_{\Lambda}C$. For example the ~15 MeV state observed in Fig.2 is one of candidates because it is considered to have the configuration of $[^{12}C(2^+) \otimes (p)_\Lambda]$. Accordingly, the energy resolution of ~3 MeV is necessary to exclude the 4.439 MeV γ-ray. The scattering angles of ~9° should be selected for dominant observation of the $3/2^+$ state in $^{13}_{\Lambda}C$ because the state is excited via the $\Delta L=1$ transition. But the scattering angles of 0 to 16 degrees is selected in the figure for increasing the yield of the 4.9 MeV γ-ray. A fit to the histogram is performed with

the function of two gaussians added to the linear function in the region of 1.3 to 7.8 MeV. The measured mean energy of the higher peak in the figure is 4.914 ± 0.010 (stat.) MeV. The error is smaller than 4.89 ± 0.07 MeV (preliminary) obtained by the $^{13}C(\pi^+, K^-)^{13}_{\Lambda}$ experiment performed by O. Hashimoto *et al.* at KEK [36]. The measured width of 220 ± 25 keV FWHM is consistent with the width of 2^+ state in ^{12}C (220 ± 19 keV FWHM) observed in the quasi-free region. The measured mean energy and width of the 4.4 MeV γ-ray peak are 4.475 ± 0.011 MeV and 314 ± 28 keV FWHM. The width of 314 ± 28 keV FWHM becomes much wider than 220 ± 19 keV measured in the quasi-free region. The 4.4 MeV peak is considered to be widened by some reasons. The recoil of ^{12}C and the Doppler shift correction are considered as dominant reasons. For the 4.4 MeV γ-ray, the energy correction is not necessary. The single escape peak of the 4.914 MeV γ-ray which should lie at 4.403 MeV is also a reason.

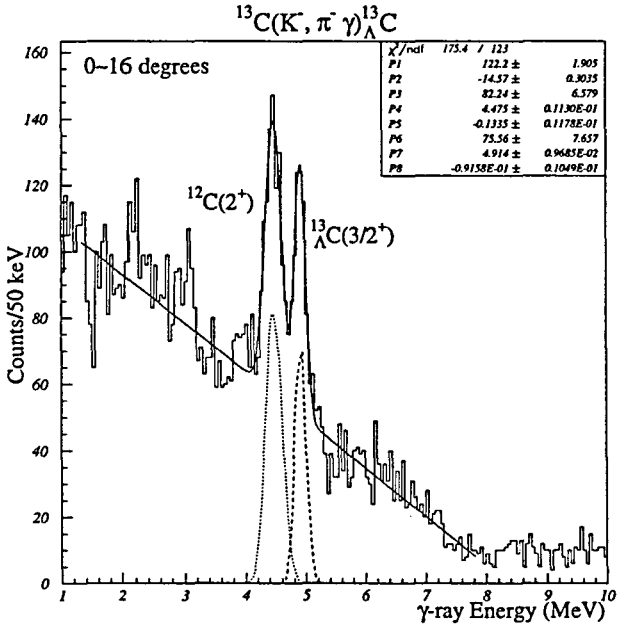

Figure 60: Energy spectrum of γ-rays detected mainly with the 12 NaI detectors installed in the center. Energy correction of the Doppler shift is performed. The bound region is selected in the energy spectrum of $^{13}_{\Lambda}C$ at the scattering angles of 0° to 16°.

The γ-ray from the $5/2^+$ state to the ground state is not observed in the figure. Theoretically, the state is expected to be in the lower energy region than that of the $3/2^+$ state due to the spin-orbit interaction between the ^{12}C core (2^+) and Λ. In our experiment the poor energy resolution of the spectrometer prevents us from observing the state without background γ-rays from the quasi-free region such as the 4.439 MeV γ-ray. In addition, the state is mainly excited via the ΔL=3 transition, therefore it is difficult to excite it by the (K^-, π^-) reaction because of its small momentum transfer. The (π^+,

K^+) reaction is suitable to excite the $5/2^+$ state in ${}^{13}_{\Lambda}$C.

There are other peaks at 2.2 MeV and 2.9 MeV. The peak at 2.2 MeV is the γ-ray from the $7/2^+$ state at 2.164 MeV to the ground state in ^{27}Si. The observed peak at 2.9 MeV is the γ-ray from the $3/2^+$ or $5/2^+$ state at 2.866 MeV to the ground state in ^{27}Si.

It is possible to verify if the Doppler shift is properly corrected. Fig.61 shows energy spectra of γ-rays detected mainly with 6 NaI detectors installed in the center above the target (a) and with 6 NaI detectors installed in the center below the target (b), where the bound region is selected in the energy spectrum of ${}^{13}_{\Lambda}$C at the scattering angles of 0° to 16°. Since the energy correction of the Doppler shift is not performed, the γ-ray energy measured with the NaI detectors installed above the target becomes higher if the γ-ray is emitted by ${}^{13}_{\Lambda}$C. While the γ-ray energy measured with the NaI detectors installed below the target becomes lower. Fits to the histograms in the region of 1.3 MeV to 7.8 MeV are performed with the function of two gaussians added to the linear function. Widths and positions are free parameters. As a result, measured energies of the 4.9 MeV γ-ray are 4.944 ± 0.017 MeV (a) and 4.871 ± 0.017 MeV (b). The energy (a) becomes higher than the energy (b), and the corrected energy of 4.914 MeV is between these energies. At the scattering angles of 0° to 16°, β of ${}^{13}_{\Lambda}$C is around 0.015 which shifts the γ-ray energy by $\sim$1 %. Although the 1 % shift is not clearly seen because the scattering angle is widely selected, shifted directions are reasonable.

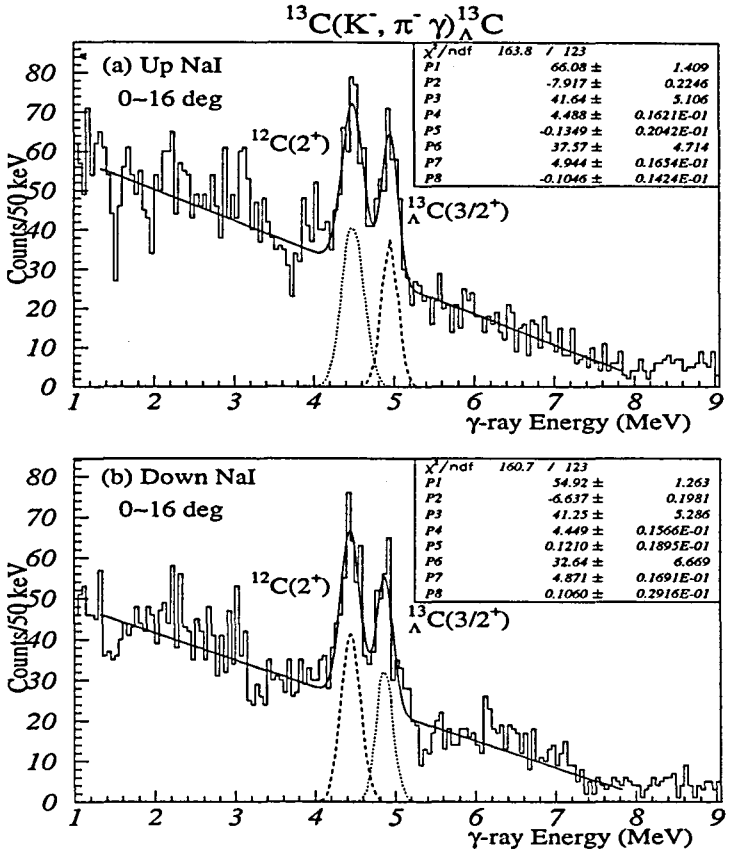

Figure 61: Energy spectra of γ-rays detected mainly with 6 NaI detectors above the target (a) and with 6 NaI detectors below the target (b). Energy correction of the Doppler shift is not performed. The bound region is selected in the energy spectrum of $^{13}_{\Lambda}C$ at the scattering angles of 0° to 16°.

4.2.2 γ-ray Energy Spectrum Around 11 MeV

The most fascinating energy spectrum of γ-rays at around 11 MeV measured mainly with the 12 NaI detectors installed in the center is shown in Fig.62. The scattering angles of 0° to 16° are selected and the energy correction of the Doppler shift is performed. A single peak is clearly observed at 11 MeV. The peak position is consistent with the energy of 10.95 $\pm$ 0.1 (stat.) $\pm$ 0.2 (syst.) MeV [33]. In the previous experiment, only γ-ray from the $1/2^-$ state to the ground state in $^{13}_{\Lambda}C$ was measured with NaI detectors at BNL. In Fig.62 the observed single peak must be composed of two γ-rays from the $1/2^-$ and $3/2^-$ doublet states to the ground state in $^{13}_{\Lambda}C$. Theoretically, expected yields for the peaks are in the same order. The single peak suggests that the $1/2^-$ and $3/2^-$ doublet states are located closely to each other. Total yield of the peak is much more than that obtained previously. By considering that the peak is composed of the full energy peak

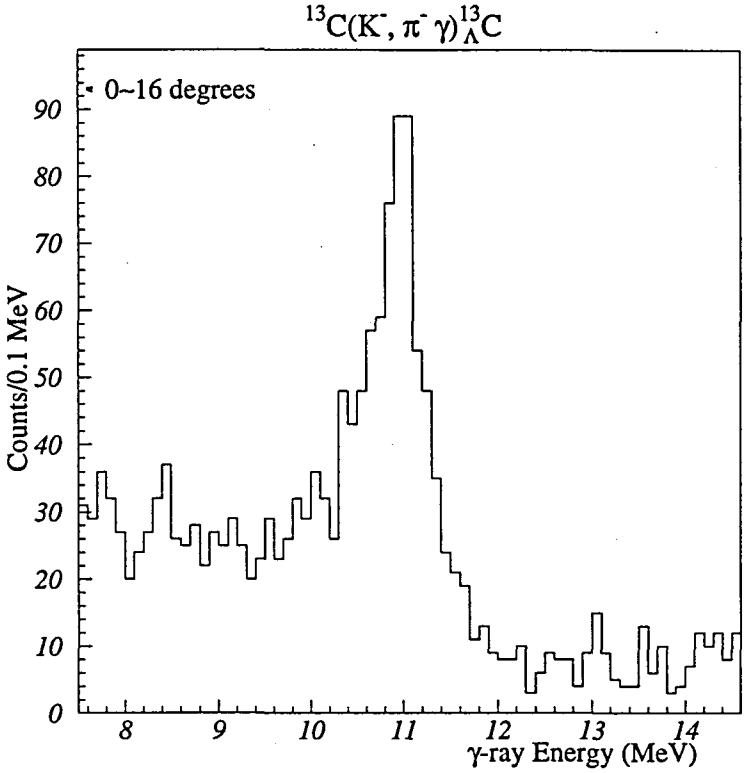

Figure 62: Energy spectrum of γ-rays detected mainly with the 12 NaI detectors installed in the center. Energy correction of the Doppler shift is performed. The bound region is selected in the energy spectrum of $^{13}_{\Lambda}C$ at the scattering angles of 0° to 16°.

and the single escape peak, a resolution of the observed peak is almost consistent with the expected energy resolution of 350 keV FWHM for the 11 MeV γ-ray.

The amount of background around 11 MeV is much less than that around 4.4 MeV. Especially, there are little background above 12 MeV. However, the amount of background in the previous experiment looks much less. There are some reasons considered to explain the difference. One of reasons is that the previous experiment measured the γ-ray in coincidence with the (K^-, π^-) reaction only at 0°. Thus the in-flight decay of K^- was easily rejected as shown in Fig.50. In addition, they used Moby-Dick spectrometer with much better energy resolution than that of 48D48 spectrometer. In the previous experiment, the event selection using the active target was strictly performed, which was utterly in contradiction to our analysis.

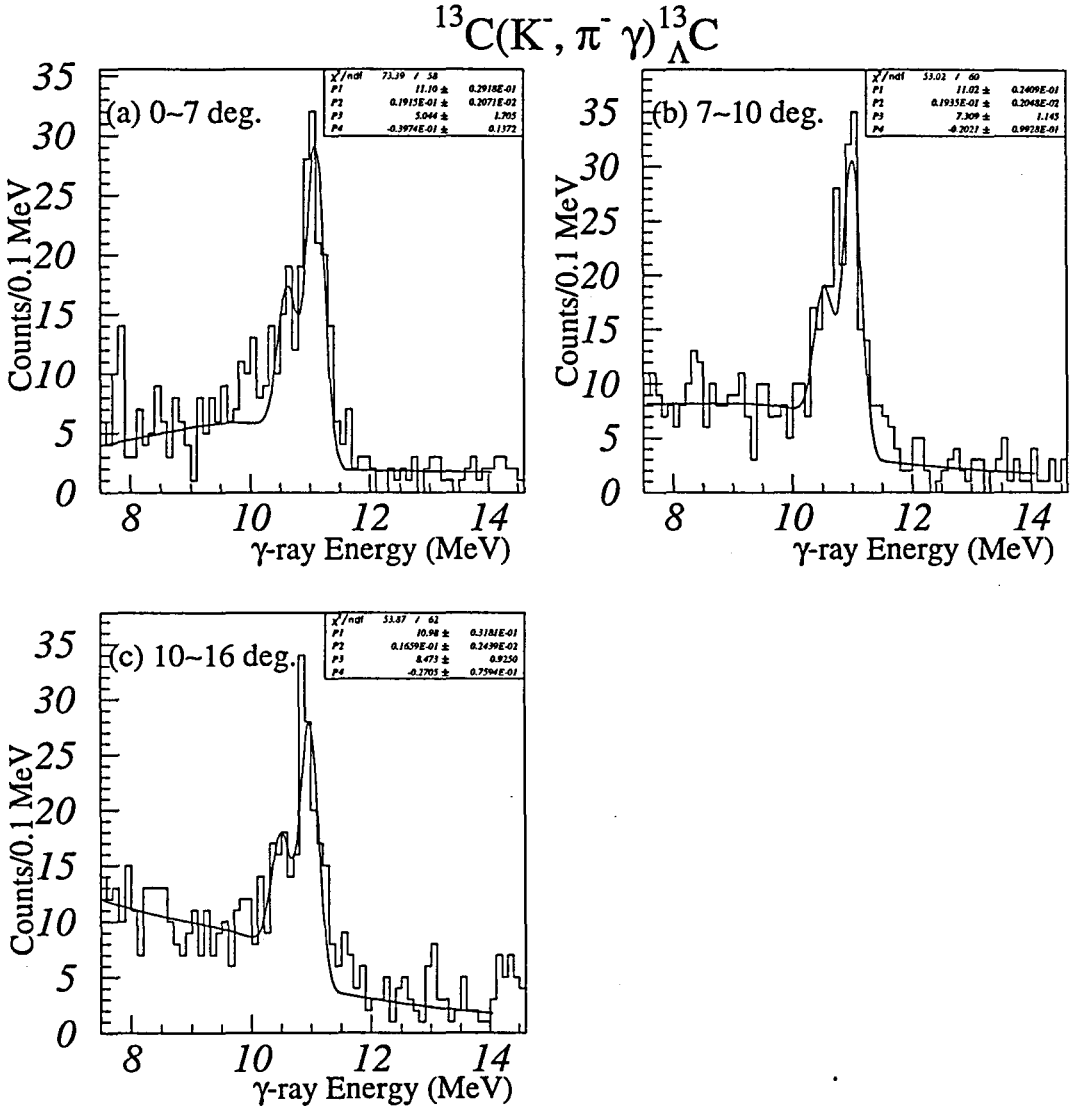

Figure 63: Energy spectra of γ-rays detected mainly with the 12 NaI detectors installed in the center. Energy correction of the Doppler shift is performed. The bound region is selected in the energy spectrum of $^{13}_{\Lambda}C$ at the scattering angles of 0° to 7° (a), 7° to 10° (b) and 10° to 16° (c).

The angular distribution of the $^{13}C(K^-, \pi^-)^{13}_{\Lambda}C$ reaction plays an important role in separating the $1/2^-$ state from the $3/2^-$ state even if the doublet states can not be separated in the γ-ray energy spectrum. It is one of the most important advantages of our experiment. The histogram at the scattering angles of 0° to 16° is divided into three histograms as shown in Fig.63, where the scattering angles of 0° to 7° (a), 7° to 10° (b) and 10° to 16° (c) are selected. Peaks at ~11 MeV are clearly observed in all the histograms. The strength ratios between the single escape peak and the full energy peak are about 1:2 in all histograms, which is consistent with the result of the Monte Carlo simulation, GEANT. Fits to the histograms are performed in the region of 7.5 to 14 MeV using the original function to produce the energy spectrum obtained by using the simulation. Measured γ-ray energies are 11.103 ± 0.029 MeV at the scattering angles of 0° to 7°, 11.016 ± 0.024 MeV at 7° to 10° and 10.980 ± 0.032 MeV at 10° to 16°. The measured γ-ray energies suggest that the excitation energy of the $1/2^-$ state is higher and that of the $3/2^-$ state is lower. It is consistent with theoretical predictions.

Errors in the fits to the histograms described above are statistical only. The statistical error at each angles is 24~32 keV. It is almost the same as that we planned to achieve before the experiment. The amount of background at the scattering angles of 0° to 7° is little. We expected that the amount of background at around 6° was the largest because the $K^- \rightarrow \pi^- + \pi^0$ decay produces γ-rays. However, the effect of the decay is found to be small. On the other hand, the amount of background is larger at the scattering angles of 10° to 16°. It is estimated that the momentum resolution of the spectrometer is worse at the large scattering angles, therefore it makes the signal to noise ratio worse.

4.3 Spin-orbit Splitting Energy

A splitting energy of the $1/2^-$ and the $3/2^-$ doublet states is extracted from Fig.64, where the horizontal axis indicates ratio of the expected yields, and the vertical axis indicates the measured γ-ray energy. The ratio of the expected yields $(N_{1/2^-}-N_{3/2^-})/(N_{1/2^-}+N_{3/2^-})$ is calculated using the acceptance of the spectrometer and the theoretical cross sections of the $1/2^-$ and $3/2^-$ doublet states shown in Fig.8. The right, the center and the left closed circles indicate the obtained γ-ray energies at the scattering angles of 0° to 7°, 7° to 10° and 10° to 16°, respectively. A fit to the three data points is performed with the linear function by considering the vertical errors. An obtained function is y=0.0760 (± 0.0271) x+11.028 (± 0.016), where x and y indicate the horizontal and vertical axes in Fig.64 respectively. The γ-ray energies (y) at x=1 and x=−1 correspond to the excitation energies of the $1/2^-$ and $3/2^-$ states in $^{13}_{\Lambda}$C. Consequently, the splitting energy of the $1/2^-$ and $3/2^-$ doublet states is obtained as 152 ± 54 keV, where the error is statistical only. Systematic errors are discussed below.

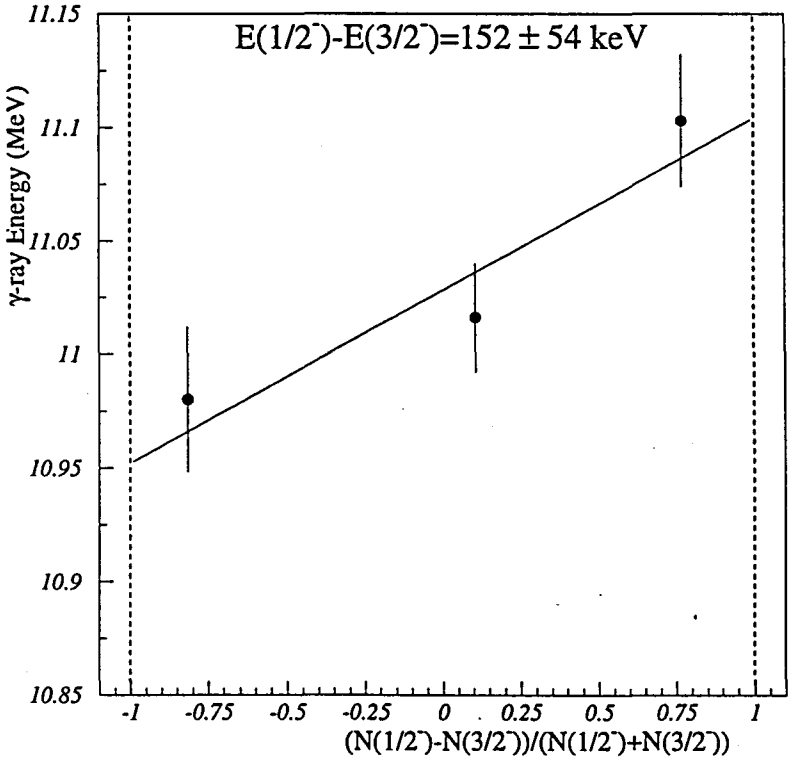

Figure 64: The horizontal axis indicates the ratio of the yields expected from the theoretically calculated cross sections and the acceptance of the spectrometer. The vertical axis indicates the γ-ray energy. The splitting energy of the doublet states is obtained as 152 ± 54 keV, where the error is statistical only.

4.4 Evaluation of Systematic Errors

The systematic error of the obtained splitting energy originating from the energy calibration of the NaI detector is extremely small because the same energy calibration is used for all the scattering angles of 0° to 7°, 7° to 10° and 10° to 16°. Therefore, systematic errors mainly originate from the predicted cross sections of the doublet states in $^{13}_{\Lambda}$C, from the fits to the histograms and from the energy corrections of the Dopller shift. The splitting energy is obtained by using the predicted cross sections. A systematic error which originates from the ambiguities of the cross sections should be estimated. In the fits to the histograms, the results may depend on what kinds of functions are used. In the energy correction of the Doppler shift, results may be changed by ambiguities of the reconstructed reaction vertex of the (K^-, π^-) reaction, the detected position of γ-ray, the measured momentum and scattering angle of π^-. Systematic errors originating from these effects are estimated below.

4.4.1 Systematic Error Originating from Cross Sections

For estimating a systematic error which originates from the predicted cross sections of the $1/2^-$ and $3/2^-$ doublet states, we evaluate yields of the γ-rays of the doublet states. Obtained yields of the γ-rays in the region of 10.3 MeV to 11.5 MeV are 164 at 0° to 7°, 166 at 7° to 10° and 142 at 10° to 16° after subtracting the exponential backgrounds. On the other hand, expected yields of the γ-rays in the region of 10.3 MeV to 11.5 MeV are calculated as

$$Y = \sigma N_B N_T \epsilon_{dt\cdot an} \epsilon_\gamma, \tag{29}$$

σ	added cross sections of the doublet states	3160 nb (0° to 7°) 1370 nb (7° to 10°) 1470 nb (10° to 16°)
N_B	No. of K^-	1.4×10^{10}
N_T	No. of target	$12 \times 0.95 / 84 \times 6 \times 6 \times 10^{23}$
$\epsilon_{dt\cdot an}$	efficiency throughout the data taking to the off-line analysis	0.36
ϵ_γ	detection efficiency for the 11 MeV γ-ray	0.045.

Expected yields are 360 at 0° to 7°, 156 at 7° to 10° and 168 at 10° to 16°. It is found that the obtained yield at the scattering angles of 0° to 7° is much less than the expected one. We regard differences between the obtained yields and the expected yields as systematic errors. The errors for the ratio of $(N_{1/2^-} - N_{3/2^-})/(N_{1/2^-} + N_{3/2^-})$ are ± 0.275 at 0° to 7°, ± 0.067 at 7° to 10° and ± 0.033 at 10° to 16°. The error at 0° to 7° is very large because of the large difference between the obtained yield and the expected yield. Several fits to the data points are performed with the linear function by considering both of the horizontal and vertical errors as shown in Fig.65. A fit with dotted line results in the largest splitting energy of 181 keV, while another fit with dashed line results in the

smallest splitting energy of 130 keV. As a result, the systematic error originating from the ambiguities of the cross sections is estimated to be ±29 keV.

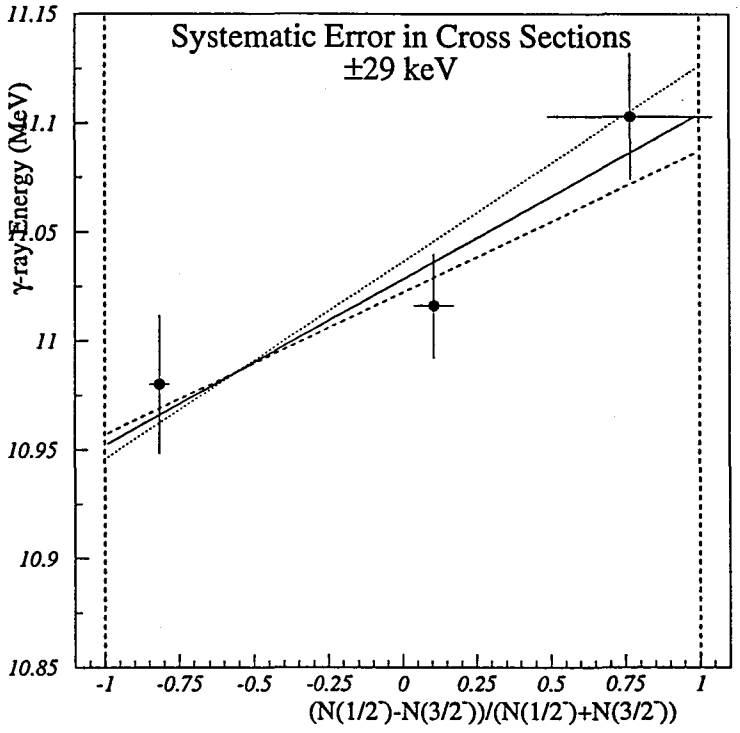

Figure 65: The horizontal axis indicates the ratio of the yields expected from the theoretically calculated cross sections and the acceptance of the spectrometer. The vertical axis indicates the γ-ray energy. The horizontal errors are systematic and the vertical errors are statistical. Solid line represents the fit to obtain the splitting energy of 152 ± 54 keV. Dotted line and dashed line represent fits resulting in the largest and the smallest splittings respectively.

4.4.2 Systematic Error Originating from Fits to Histograms

A systematic error of the obtained splitting energy in the fits to the histograms is estimated using functions of some kinds. Functions used in the fits are tabulated in Table.9, and results of the fits are summarized in Table.10.

In the fit A, as described above the original function is used in the region of 7.5 to 14 MeV. The function reproduces the energy spectrum of the 11 MeV γ-ray with the energy resolution of 350 keV FWHM obtained by using the simulation. For the fit to the continuous background, the exponential is used. In the fit B, how the binning of the histogram contributes to the result is studied. In Fig.63, histograms with the binning

Fit	Function for peaks	Resolution of function (keV FWHM)	Function for background	Histogram binning (keV/bin)
A	original	350	e	100
B	original	350	e	50
C	original	300	e	100
D	original	400	e	100
E	original	350	p1	100
F	2g	350	e	100

Table 9: Functions used in the fits to the histograms.

of 100 keV/bin are fitted. In the fit B, histograms with the binning of 50 keV/bin are studied. The binning of 200 keV/bin is not studied because it joins the single escape peak and the full energy peak together. In the fit C and D, the functions reproducing the energy spectra of the 11 MeV γ-ray with the energy resolutions of 300 keV (C) and 400 keV (D) FWHM obtained by using the simulation are used. In the fit E, the linear function is used instead of the exponential for the fit to the continuous background. In the fit F to the histograms, the function of two gaussians added to the exponential is used, where widths of the gaussians are fixed to 350 keV FWHM, and a mean of the lower gaussian is also fixed at 511 keV lower than that of the higher gaussian. It is found that the splitting energy changes from 135 keV in the fits of E and F to 171 keV in the fit B. As a result, the systematic error originating from fits is estimated to be $\pm$19 keV.

4.4.3 Systematic Error Originating from Doppler Shift Correction

A systematic error originating from the energy correction of the Doppler shift is estimated using the Monte Carlo simulation GEANT. The processes are

1. A scattered angle of a π^- with the momentum of 0.84 GeV/c is decided in the horizontal angles of -8° to 8° and in the vertical angles of -16° to 0°.

2. β of a recoil ${}^{13}_{\Lambda}$C is calculated by assuming that a K^- with the momentum of 0.93 GeV/c enters at 0 degrees.

3. A γ-ray with a Doppler shifted energy ($\sim$11 MeV) is emitted isotropically. For estimating the effect of the reaction vertex, the γ-ray is emitted from the region with the same size of a LT segment.

Fit	γ-ray energy (MeV) $0°\sim7°$	γ-ray energy (MeV) $7°\sim10°$	γ-ray energy (MeV) $10°\sim16°$	Splitting energy (keV)
A	11.103 $\pm$ 0.029	11.016 $\pm$ 0.024	10.980 $\pm$ 0.032	152
(χ^2)	(1.27)	(0.88)	(0.87)	(1.22)
B	11.096 $\pm$ 0.025	11.005 $\pm$ 0.025	10.967 $\pm$ 0.036	171
(χ^2)	(0.74)	(0.80)	(0.77)	(1.30)
C	11.087 $\pm$ 0.028	11.014 $\pm$ 0.021	10.961 $\pm$ 0.027	154
(χ^2)	(1.38)	(0.94)	(0.92)	(0.50)
D	11.110 $\pm$ 0.028	11.018 $\pm$ 0.027	10.999 $\pm$ 0.035	143
(χ^2)	(1.20)	(0.85)	(0.83)	(1.72)
E	11.095 $\pm$ 0.030	11.015 $\pm$ 0.025	10.978 $\pm$ 0.022	135
(χ^2)	(1.52)	(0.95)	(0.76)	(0.96)
F	11.061 $\pm$ 0.027	10.991 $\pm$ 0.023	10.950 $\pm$ 0.026	135
(χ^2)	(1.45)	(0.98)	(0.94)	(0.63)

Table 10: Results of the fits to the histograms using various functions. The fitting χ^2 is also written.

4. 72 NaI detectors are installed in the same positions. The γ-ray is detected with mainly one of the 12 NaI detectors installed in the center. All NaI detectors have zero energy resolution.

5. The γ-ray energy is corrected by using the position of the NaI detector with the maximal energy deposit and the scattered angle and the momentum of the π^-. The γ-ray is assumed to be emitted from the target center.

6. A difference between a measured γ-ray energy and 11 MeV is obtained as an energy resolution due to uncorrected effects.

Results of the simulation are summarized in Table.11. The effect to produce the largest systematic error in the energy correction of the Doppler shift is found to be the size of the NaI crystal. An obtained energy resolution is 11.03 keV σ. Since a NaI crystal located at 10.5 cm from the target center covers relatively large solid angle, the effect becomes the largest. Depth of the crystal where a γ-ray interacts does not so much contribute to the result. For estimating the effect of the momentum resolution, ΔP=10 MeV/c that is measured for the in-flight decay of K^- at the scattering angles of 1° to 2° is used. The effect of the momentum resolution is found to be small (1.97 keV σ). For estimating the effect of the scattered angle resolution, $\Delta\theta$=0.6° that is calculated by considering the multiple scattering in LT, FAC, FP and air is used. The effect is also found to be small (2.10 keV σ). It is most difficult to estimate the effect of the vertex resolution of the (K^-,

Effect	Energy Resolution of measured γ-ray (keV σ)
Size of NaI crystal (6.35 cm $\times$ 6.35 cm $\times$ 30.48 cm)	11.03
Momentum resolution (ΔP=10 MeV/c)	1.97
Scattered angle resolution ($\Delta\theta$=0.6°)	2.10
Vertex resolution (ΔX=3.00 cm)	3.75
(ΔY=0.75 cm)	
(ΔZ=1.50 cm)	
Total	12.0

Table 11: Systematic Errors in the correction of the Doppler shift.

π^-) reaction because the resolution changes together with the scattering angle. After all, the vertex resolutions of 3.00 cm for the x direction, 0.75 cm for the y direction and 1.50 cm for the z direction which are half sizes of a target cell are used. Since the z vertex for the energy correction of the Doppler shift is determined from the LT segment with the maximal energy deposit, the used vertex resolutions are the worst ones. The effect is also found to be small (3.75 keV σ). Total energy resolution due to uncorrected effects is found to be 12.0 keV σ that is more than an order-of-magnitude smaller than that of the NaI detector for the 11 MeV γ-ray (150 keV σ). There is one more simulation performed to study how the effects contribute to the result of the experimental splitting energy. After the simulation including all of the effects without the energy resolution of the NaI detector, γ-ray energies are corrected for both events of π^-s scattered at 0° to 7° and scattered at 10° to 16°. Obtained γ-ray energies of the full energy peaks are 11.000 MeV with the resolution of 10.4 keV σ at the scattering angle of 0° to 7°, while that is 10.999 MeV with the energy resolution of 11.0 keV σ at 10° to 16°. As a result, the systematic error originating from the energy correction of the Doppler shift is $\sim$1 keV which is much smaller than the statistical error. It is found that the energy correction of the Doppler shift does not so much contribute to the result of the spin-orbit splitting energy.

4.5 Discussion

As the results of estimating the systematic errors of the obtained spin-orbit splitting, ±29 keV is in the predicted cross sections, ±19 keV is in the fitting to the histograms and ±1 keV is in the energy correction of the Doppler shift. A final result of the spin-orbit splitting is 152 ± 54 (stat.) ± 35 (syst.) keV. It is almost 30~40 times smaller than that of single particle states in nuclei. However, the j_Λ=l_Λ−1/2 ($p_{1/2}(\Lambda)$) state still appears higher in energy as in nuclei.

Recently theoretical calculations were performed in the framework of microscopic 3α + Λ model for $^{13}_{\Lambda}$C [34]. OBE models of Nijmegen model D (ND), Nijmegen model F (NF) and the newest Nijmegen soft-core model (NSC97f) gave 0.75 (ND), 0.96 (NF) and 0.78 MeV (NSC97f) for the splitting of the $1/2^-$ and $3/2^-$ doublet states. Another calculations without using an antisymmetric spin-orbit interaction (ALS) were 1.09 (ND), 1.19 (NF) and 1.09 MeV (NSC97f). The OBE models still predict large splittings even in the calculation with the newest model, NSC97f. The ALS decreased the splitting energy by 20 to 30 %. The strength of the ALS predicted by the OBE models is much smaller than that predicted by quark models. According to a recent G-matrix calculation using quark-based ΛN interactions, the strength of ALS amounts to approximately 85 % of that of the spin-orbit interaction (LS) [48, 49].
E. Hiyama *et al.* also attempted calculations using strengthened OBE ALS interaction which reproduced the relative strength of the quark-based interactions. The obtained splitting energy was 150~200 keV in $^{13}_{\Lambda}$C, and they wrote that the difference originated mainly from the relative strength of ALS, not from LS itself. The quark-based interaction predicts smaller splitting. Judging from these calculations, it can be said that the quark-based interaction well describes our data.

D. J. Millener *et al.* points out that a tensor interaction makes a significant contribution to the splitting of $^{13}_{\Lambda}$C [50]. The nuclear spin-orbit force mixes a small S=1 component into the ^{12}C core wave functions, and a spin-spin interaction and the tensor interaction arise from the S=1 component. It is verified in their calculation with the spin-orbit interaction set to zero that the tensor force in the NSC97f puts the $1/2^-$ state 226 keV below the $3/2^-$ state. They made new interactions DNP99 by changing the sign of the odd-state central interaction and reducing the strength of the even state interaction to compensate, by about 2/3 for S=0 and 3/4 for S=1 to get the right strength for the spin-spin interaction. They also scaled the LS and ALS terms to get what the previous hypernuclear data demand, and reduced the strength for the tensor interaction by 3/4. Their prediction for the splitting in $^{13}_{\Lambda}$C is 107 keV, where the spin-spin interaction (+42 keV), the spin-orbit interaction (+280 keV) and the tensor interaction (-215 keV) are included. The prediction reproduces our data well.

In 1998, a new ^{89}Y(π^+, K^+)$^{89}_{\Lambda}$Y experiment was performed at KEK by Nagae *et al.*. Since they had observed large splitting in $^{89}_{\Lambda}$Y, the new experiment was to confirm the splitting. By virtue of the momentum calibration system using also the well known ^{12}C target and improved off-line analysis, the energy resolution of less than 2 MeV was achieved using SKS spectrometer. The splitting of the f-states with a few MeV was still

observed under the data analyses. However, relative strength of the $f_{5/2}$ and $f_{7/2}$ states are differently observed from the theoretical prediction. It is possible that one of the peaks is a hole state. A final result is to be published in the near future [11].

In 1998, H. Tamura *et al.* performed the ^{9}Be(K^{-}, π^{-} γ)$^{9}_{\Lambda}$Be experiment at BNL to observe γ-rays from the spin-orbit splitting doublet states to the ground state in $^{9}_{\Lambda}$Be by using Ge detectors [51, 52]. In the previous experiment, the $3/2^{+}$ and $5/2^{+}$ doublet states had not been resolved by using NaI detectors. An excellent energy resolution of the Ge detector may be capable of separating the doublet states. Although the off-line analyses were in progress, peak structures were observed at $\sim$3.05 MeV. In addition, the structures looked like two peaks with about 30 keV splitting. Our result will have to be a help to confirm the observed splitting. Since the amount of background at around 3 MeV is large, they tried to decrease background by the improvement of the field map of the spectrometer.

5 Summary

The Λ-nucleus spin-orbit interaction is of great interest for its fascinating smallness compared with that of the nucleon-nucleus which is more than an order-of-magnitude larger. There are discrepancies between experimental results of the Λ-nucleus spin-orbit splitting, and there are also discrepancies between theoretical predictions on the Λ-nucleus spin-orbit splitting. A new experiment to conclude the Λ-nucleus spin-orbit splitting has been needed for more than 20 years.

In 1998 we carried out the $^{13}C(K^-, \pi^- \gamma)^{13}_{\Lambda}C$ experiment at BNL. The γ-rays from the $1/2^-$ and $3/2^-$ doublet states at ~11 MeV to the ground state in $^{13}_{\Lambda}C$ were measured with 72 NaI detectors to obtain the spin-orbit splitting energy with high precision. The energy resolution of the NaI detector is 350 keV FWHM for the detection of the 11 MeV γ-ray. This energy resolution is almost an order-of-magnitude better than that of the magnetic spectrometer (~2 MeV). $^{13}_{\Lambda}C$ is an unique hypernucleus to measure the spin-orbit splitting energy clearly. $^{13}_{\Lambda}C$ has single Λ particle states with $p_{1/2}(\Lambda)(j_\Lambda=l_\Lambda-1/2)$ and $p_{3/2}(\Lambda)(j_\Lambda=l_\Lambda+1/2)$ which couple to the spin 0^+ ^{12}C core. The energy difference of the states thus simply corresponds to the spin-orbit splitting. Since these states lie under the particle emission threshold, the energy difference can be observed by their γ-decays. The experiment was performed at AGS-D6 line using the high intensity kaon beam line and 48D48 spectrometer with large acceptance. The K^- beam momentum was set at 0.93 GeV/c. Scattered π^-s at 0 to 16 degrees were detected by the spectrometer, which enabled us to excite the doublet states simultaneously. This beam momentum provides advantageous angular distributions of the $1/2^-$ and $3/2^-$ doublet states, at the forward angles of the $^{13}C(K^-, \pi^-)^{13}_{\Lambda}C$ reaction the $1/2^-$ state is excited dominantly, while at the larger angles of ~13 degrees the $3/2^-$ state is excited dominantly. Thus we can selectively observe the doublet states. We made an active target of ^{13}C with thickness of 12 cm, which enabled us to selectively observe the $^{13}C(K^-, \pi^-)^{13}_{\Lambda}C$ reaction at all the scattering angles by suppressing the background mainly due to the in-flight decay of K^-.

In the off-line analysis, the high quality data collected with 1.4×10^{10} K^-s are analyzed and 12 NaI detectors with fine energy resolution installed in the center are mainly used. To investigate whether the experiment and the analysis were correctly performed, γ-rays emitted from the quasi-free region of the $^{13}C(K^-, \pi^-)$ reaction are studied. Two dominant peaks are clearly observed at 4.4 MeV and 15.1 MeV. The former corresponds to the γ-ray from the 2^+ state to the ground state in ^{12}C, while the latter corresponds to the γ-ray from the 1^+ state to the ground state in ^{12}C. The measured energy of the 4.4 MeV peak is 4.468 ± 0.009 MeV which is a little bit higher than 4.439 MeV. The energy resolution is 220 ± 19 keV FWHM which is good enough. The width of the observed 15.1 MeV peak looks wider than the expected energy resolution of 410 keV FWHM because the resolution can not separate the single escape peak with height of ~60 % of the full energy peak.

In the bound region at the scattering angles of 7 to 14 degrees a peak at 4.9 MeV is

observed clearly separated from the 4.439 MeV peak corresponding to the γ-ray emitted by the ^{12}C. The peak corresponding to the γ-ray from the $3/2^+$ state to the ground state in the $^{13}_{\Lambda}$C was previously observed and measured as 4.89 $\pm$ 0.07 MeV (preliminary) by the ^{13}C(π^+, K^+)$^{13}_{\Lambda}$C experiment. A fit to the histogram is performed with the function of two gaussians added to the linear function, where one gaussian is for the 4.9 MeV peak and the other is for the 4.439 MeV peak. A measured energy of the higher peak is 4.914 $\pm$ 0.010 MeV, where the error is statistical only. We succeed in observing the most fascinating peak at 11 MeV corresponding to the $1/2^-$ and $3/2^-$ doublet states in $^{13}_{\Lambda}$C at the scattering angles of 0 to 16 degrees. The peak looks as if it were a single peak with almost the same width as the expected 350 keV FWHM, which suggests that the two peaks are located closely to each other. The histogram is divided into three histograms at the scattering angles of 0° to 7°, 7° to 10° and 10° to 16°. Fits to three histograms are performed with the original function which reproduces the energy spectrum of the 11 MeV γ-ray with the energy resolution of 350 keV FWHM obtained by using the simulation. Measured γ-ray energies are 11.103 $\pm$ 0.029 MeV at 0° to 7°, 11.016 $\pm$ 0.024 MeV at 7° to 10° and 10.980 $\pm$ 0.032 MeV at 10° to 16°. The statistical errors of 24$\sim$32 keV are almost the same as that we planned to achieve before the experiment. From the measured γ-ray energies, the splitting energy of the $1/2^-$ and $3/2^-$ doublet states is obtained as 152 $\pm$ 54 keV. In the summary of the estimations of the systematic errors, $\pm$29 keV is in the predicted cross sections, $\pm$19 keV is in the fitting to the histograms and $\pm$1 keV is in the energy correction of the Doppler shift. The systematic error originating from the energy calibration of the NaI detector is considered to be extremely small. The final result of the spin-orbit splitting is obtained as 152 $\pm$ 54 (stat.) $\pm$ 35 (syst.) keV. It is almost 30$\sim$40 times smaller than that of single particle states in nuclei. However, the j_Λ=$l_\Lambda$$-$1/2 ($p_{1/2}(\Lambda)$) state still appears higher in energy as in nuclei.

Recently, theoretical calculations were performed by E. Hiyama *et al.* in the framework of microscopic 3α + Λ model for $^{13}_{\Lambda}$C. OBE models of Nijmegen model D (ND), Nijmegen model F (NF) and the newest Nijmegen soft-core model (NSC97f) gave 0.75 (ND), 0.96 (NF) and 0.78 MeV (NSC97f) for the splitting of the $1/2^-$ and $3/2^-$ doublet states. The OBE models still predict large splittings even in the calculation with the newest model, NSC97f. E. Hiyama *et al.* also attempted calculations using strengthened OBE ALS interaction which reproduced the relative strength of the quark-based interactions. The obtained splitting energy was 0.15$\sim$0.20 MeV in $^{13}_{\Lambda}$C. The quark-based interaction seems well describing our data.

D. J. Millener *et al.* points out that a tensor interaction makes a significant contribution to the splitting of $^{13}_{\Lambda}$C. The nuclear spin-orbit force mixes a small S=1 component into the ^{12}C core wave functions, and the spin-spin interaction and the tensor interaction arise from the S=1 component. Their prediction for the splitting in $^{13}_{\Lambda}$C is 107 keV, where the spin-spin interaction (+42 keV), the spin-orbit interaction (+280 keV) and the tensor interaction (-215 keV) are included. The prediction reproduces our data well.

In 1998, H. Tamura *et al.* performed the ^{9}Be(K^-, π^- γ)$^9_{\Lambda}$Be experiment at BNL to observe γ-rays from the spin-orbit splitting doublet states to the ground state in $^9_{\Lambda}$Be by using Ge detectors. Although the off-line analyses were in progress, peak structures were

observed at ~3.05 MeV. In addition, the structures looked like two peaks with about 30 keV splitting. Our result will have to be a help to confirm the observed splitting.

BNL-AGS-E929 Collaboration

S. Ajimura, H. Hayakawa, T. Kishimoto, H. Kohri, K. Matsuoka,
S. Minami, Y. Miyake, T. Mori, K. Morikubo, E. Saji, A. Sakaguchi,
Y. Shimizu, M. Sumihama
Department of Physics, Osaka University, Toyonaka, Osaka 560-0043 Japan

R. E. Chrien, M. May, P. Pile, A. Rusek, R. Sutter
Brookhaven National Laboratory (BNL), Upton, New York 11973, USA

P. M. Eugenio, G. Franklin, P. Khaustov, K. Paschke, B. Quinn
Department of Physics, Carnegie Mellon University, Pittsburgh, PA 15213, USA

J. Franz
University of Freiburg, Hermann-Herder-Str.3, D79104 Freiburg, Germany

T. Fukuda, H. Noumi, H. Outa
High Energy Accelerator Research Organization (KEK), Tsukuba, Ibaragi, 305-0801,
Japan

L. Gan, L. Tang, L. Yuan
Department of Physics, Hampton University, Hampton, VA 23668, USA

H. Tamura
Department of Physics, Tohoku University, Sendai 980-8578, Japan

J. Nakano, T. Tamagawa, K. Tanida
Department of Physics, University of Tokyo, Tokyo 113-0033, Japan

R. Sawafta
Department of Physics, North Carolina A T State University, Greensboro, NC 27411,
USA

Acknowledgements

It is my great pleasure to acknowledge the collaboration, advice, support and encouragement many people gave to complete the present work.

First of all, I would like to express my sincere gratitude to my supervisor, Prof. Tadafumi Kishimoto. Under his guidance, I had the opportunity to work on the experiment, E929 carried out at BNL in 1998. I have been impressed by his leadership, spirits and efforts in a wide range of nuclear and astro physics. I am deeply grateful for beneficial discussions with Prof. Atsushi Sakaguchi, Dr. Shuhei Ajimura, Dr. Yukio Shimizu, Mr. Kenji Matsuoka, Ms. Hisako Hayakawa, Mr. Kazuya Morikubo, Mr. Eiji Saji, Ms. Mizuki Sumihama, Ms. Shizu Minami, Mr. Tomohito Mori, Mr. Kazuki Wakae, Mr. Tatsuto Kanie and Mr. Yoichiro Miyake. I have gained various knowledge from Prof. Atsushi Sakaguchi and learned sharp insight for physics from Dr. Shuhei Ajimura. I thank Ms. Mizuki Sumihama for extensive supports at BNL and analysis on LED. I want to ask Mr. Yoichiro Miyake for advanced analysis on LT. I would like to acknowledge Ms. Eriko Matsumoto for many works supporting us.

I appreciate Prof. R. E. Chrien for giving helpful suggestions. I am very glad to have performed the last experiment for him together. I would like to express thanks to Prof. M. May, Prof. P. Pile and Dr. A. Rusek for valuable discussions and advices. Especially, I never forget that Dr. A. Rusek came to Osaka University for giving helpful advices. During my stay at BNL, I was helped by technicians in the medium energy group, and many and various circuits were repaired by Dr. HEEP. I also thank other BNL stuff, especially the people of the Main Control, Target Desk, Health Physics.

I would like to acknowledge Prof. G. B. Franklin, Prof. B. Quinn, Dr. P. Eugenio, Mr. P. Khaustov and Mr. K. Paschke from Carnegie Mellon University, Prof. J. Franz from University of Freiburg and Prof. R. Sawafta from North Carolina A T State University for fruitful discussions. I still believe that the experiment was not successfully finished without their supports.

I have been very fortunate to have collaborations with Prof. T. Fukuda, Dr. H. Noumi and Mr. H. Outa, especially I appreciate Dr. H. Noumi for constructing the most suitable support frame of NaI detectors.

I would like to express sincere appreciation to Prof. L. Tang, Dr. L. Gan and Mr. L. Yuan from Hampton University and Prof. H. Tamura from Tohoku University for performing the experiment with many efforts.

I thank Mr. J. Nakano, Mr. T. Tamagawa and Dr. K. Tanida from University of Tokyo and Mr. H. Akikawa from Kyoto University for many advices and encouragement. When I was at BNL, I could work comfortably and live joyfully with them.

I am grateful to Prof. D. J. Millener from BNL for fascinating discussions about the spin-orbit splitting and to Prof. J. C Peng from Los Alamos National Laboratory for valuable suggestions.

I would like to acknowledge Prof. T. Motoba for calculating the cross sections of the doublet states in ${}^{13}_{\Lambda}\mathrm{C}$. The calculation is one of the most important works.

References

[1] A. Bohr and B. R. mottelson, Nuclear Structure Vol.1.

[2] P. H. Pile *et al.*, Phys. Rev. Lett. 66 (1991) 2585.

[3] T. Hasegawa *et al.*, Phys. Rev. Lett. 74 (1995) 224.

[4] T. Hasegawa *et al.*, Phys. Rev. C 53 (1996) 1210.

[5] D. J. Millener *et al.*, Phys. Rev. C38 (1988) 2700.

[6] W. Bruckner *et al.*, Phys. Lett. 79B (1978) 157.

[7] M. May *et al.*, Phys. Rev. Lett. 47 (1981) 1106.

[8] M. May *et al.*, Phys. Rev. Lett. 51 (1983) 2085.

[9] R. H. Dalitz *et al.*, Nucl. Phys. A 625 (1997) 71.

[10] T. Nagae *et al.*, Int. INS symp. on Nuclear and Particle Physics with meson beams in the 1 GeV/c region, eds. S. Sugimoto and O. Hashimoto (Universal Academic Press, Tokyo, 1995) 175.

[11] H. Hotchi, Doctor thesis of University of Tokyo (2000)

[12] T. Hamada *et al.*, Nucl. Phys. 34 (1962) 382.

[13] R. V. Reid *et al.*, Ann. of Phys. 50 (1968) 411.

[14] W. N. Cottingham *et al.*, Phys. Rev. D8 (1973) 800.

[15] M. N. Nagels *et al.*, Phys. Rev. D12 (1975) 744.

[16] Th. A. Rijken *et al.*, Phys. Rev. C 59 (1999) 21.

[17] Th. A. Rijken *et al.*, Nucl. Phys. A639 (1998) 29.

[18] M. N. Nagels *et al.*, Phys. Rev. D15 (1977) 2547.

[19] M. N. Nagels *et al.*, Phys. Rev. D20 (1979) 1633.

[20] C. B. Dover *et al.*, Nucl. Phys. 12 (1984) 171.

[21] Y. Yamamoto *et al.*, Prog. Theor. Phys. 73 (1985) 905.

[22] J. J. de Swart *et al.*, N. Cim. 102A (1989) 203.

[23] J. J. de Swart *et al.*, in Properties and Interactions of Hyperons, eds. B. F. Gibson, P. D. Barnes and K. Nakai (World Scientific, 1994) 37.

[24] R. Timmermans *et al.*, in Properties and Interactions of Hyperons, eds. B. F. Gibson, P. D. Barnes and K. Nakai (World Scientific, 1994) 179.

[25] K. Itonaga *et al.*, Prog. of Theore. Phys. 84 (1990) 291.

[26] D. A. Liberman *et al.*, Phys. Rev. D16 (1977) 1542.

[27] C. De Tar *et al.*, Phys. Rev. D17 (1978) 323.

[28] M. Oka *et al.*, Phys. Lett. 90B (1980) 41 ; Prog. Theor. Phys. 66 (1981) 556, 572.

[29] M. Harvey *et al.*, Nucl. Phys. A352 (1981) 301,326.

[30] A. Faessler *et al.*, Phys. Lett. 112B (1982) 201.

[31] O. Morimatsu *et al.*, Nucl. Phys. A420 (1984) 573.

[32] H. J. Pirner *et al.*, Phys. Lett. 114B (1982) 308.

[33] M. May *et al.*, Phys. Rev. Lett. 78 (1997) 4343.

[34] E. Hiyama *et al.*, to be published.

[35] E. H. Auerbach *et al.*, Phys. Rev. Lett. 47 (1981) 1110.

[36] O. Hashimoto *et al.*, Nucl. Phys. A639 (1998) 93.

[37] R. E. Chrien *et al.*, Nucl. Phys. A478 (1988) 705.

[38] Private communication with T. Motoba

[39] Kishimoto *et al.*, Proposal of BNL-AGS-E929.

[40] P. H. Pile *et al.*, Nucl. Inst. and Meth. A321 (1992) 48.

[41] T. Iijima, Doctor thesis of Kyoto University (1995).

[42] I. R. Sukaton, Doctor thesis of Carnegie Mellon University (1995).

[43] F. Merrill, Doctor thesis of Carnegie Mellon University (1995).

[44] V. Sum *et al.*, Nucl. Instr. Meth. A326 (1993) 489.

[45] W. R. Leo, Techniques for Nucl. and Part. Phys. Exp. 2nd Revised Edition Springer-Verlag.

[46] Table of Isotopes Eighth Edition Vol.1.

[47] E. Andersen *et al.*, Nucl. Instr. Meth. A320 (1992) 300.

[48] Y. Fujiwara *et al.*, Phys. Rev. Lett. 76 (1996) 2242.

[49] M. Kohno *et al.*, in Abstracts of the APCTP Workshop on Strangeness Nuclear Physics, Seoul, February 19 (1999) 77.

[50] Private communication with D. J. Millener.

[51] Private communication with H. Tamura and H. Akikawa

[52] H. Tamura *et al.*, Nucl. Phys. A639 (1998) 83.